

Neuroanatomical and morphological properties of neurons
that generate inspiratory related breathing rhythm
and influence respiratory motor pattern in mice

Victoria Tonita Akins

Virginia Beach, Virginia

Master of Science, College of William & Mary, 2012
Master of Science, James Madison University, 2010
Bachelor of Science, James Madison University, 2008

A Dissertation presented to the Graduate Faculty
of The College of William & Mary in Candidacy for the Degree of
Doctor of Philosophy

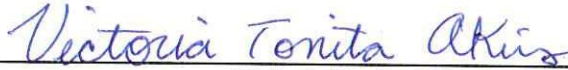
Department of Applied Science

College of William & Mary
May, 2018

APPROVAL PAGE

This Dissertation is submitted in partial fulfillment of
the requirements for the degree of

Doctor of Philosophy




Victoria Tonita Akins

Approved by the Committee, December, 2017



Committee Chair

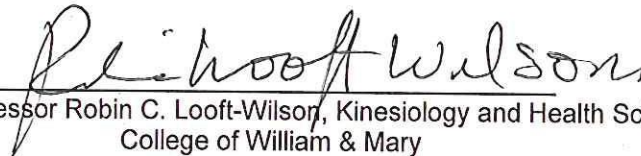
Professor Christopher A. Del Negro, Applied Science
College of William & Mary



Professor Gregory D. Smith, Applied Science
College of William & Mary



Professor Eric L. Bradley, Biology
College of William & Mary



Associate Professor Robin C. Looft-Wilson, Kinesiology and Health Sciences
College of William & Mary

COMPLIANCE PAGE

Research approved by

Institute of Animal Care and Use Committee

Protocol number(s): IACUC-2016-08-02-11305-cadeln

Date(s) of approval: 2017-05-10

ABSTRACT

The relationship between neuron morphology and function is a perennial issue in neuroscience. Information about synaptic integration, network connectivity, and the specific roles of neuronal subpopulations can be obtained through morphological analysis of key neurons within any given microcircuit. Breathing is essential behavior for humans and all mammals, yet the neural microcircuit that governs respiration is not completely understood. The respiratory neural microcircuit resides within the ventral respiratory column located in the medulla. Within the respiratory column, the site of respiratory rhythm generation is the bilaterally distributed preBötzinger complex (preBötC). Rhythm-generating neurons in the preBötC are derived from a single genetic line, i.e., precursor cells expressing the transcription factor Developing brain homeobox-1 (Dbx1). An analysis of over 40 dendritic morphological features of rhythmogenic Dbx1 preBötC neurons and putatively premotor Dbx1 neurons in the intermediate reticular formation, revealed these two populations are similar except reticular neurons have a larger dendritic diameter, which may contribute to a greater passive transmembrane conductance. Both populations showed commissural axon projections and reticular formation neurons show premotor-like projections to the XII motor nucleus. These morphological data provide additional evidence supporting bilateral synchronization the preBötC through Dbx1 neurons, and demonstrate that Dbx1 preBötC neuron connectivity includes recurrent interconnections. On the molecular level, the ion channels that mediate rhythm-generating whole-cell ion currents have not been not identified, and were investigated using principally an anatomical approach. The nonspecific cation current, I_{CAN} , underlies robust inspiratory drive potentials in the preBötC and the persistent sodium current, I_{NaP} may play a role in the production of robust bursts when respiration is challenged in such cases as anoxia or hypoxia. The leading candidate for ion channels that contribute to I_{CAN} belong to the transient membrane receptor (Trp) ion channel superfamily and the leading ion channel candidate for I_{NaP} is $Na_v1.6$. I determined the presence of Trpc3 ion channels and $Na_v1.6$ ion channels on Dbx1 preBötC neurons (as well as their expression in neighboring non-Dbx1 preBötC neurons). Finally, breathing behavior involves periodic sighs, which are slower than normal eupneic breathing but critical for lung function. I examined receptor expression for bombesin-like peptides neuromedin B (NMB) and gastrin releasing peptide (GRP), which are important for sigh behavior. I show that NMB and GRP receptors are expressed in Dbx1 preBötC neurons and are not expressed by glia in the preBötC, as posited by some because of the low frequency of sigh breaths. These advances in morphological and anatomical knowledge can be used to design targeted *in vitro* and *in vivo* experiments to further explore their role in respiratory rhythm and pattern generation.

TABLE OF CONTENTS

Acknowledgements	iii
Dedications	iv
List of Tables	v
List of Figures	vi
Literature Review	1
Chapter 1. Morphology of Dbx1 respiratory neurons in the preBötzinger complex and reticular formation of neonatal mice	37
1.1 Introduction	37
1.2 Methods	40
1.3 Data Records	46
1.4 Technical Validation	47
1.5 Data Citations	50
Chapter 2. Analysis of dendritic arbor and axon projections of Dbx1 preBötC and reticular formation neurons	53
2.1 Introduction	53
2.2 Methods	55
2.3 Results	58
2.4 Discussion	115
Chapter 3. Trpc3 and Nav1.6 ion channels on Dbx1 preBötC neurons	123
2.1 Introduction	123
2.2 Methods	127

	2.3 Results	133
	2.4 Discussion	138
Chapter 4.	Bombesin-like receptors involved in sighs on preBötC neurons and glia	144
	2.1 Introduction	144
	2.2 Methods	148
	2.3 Results	150
	2.4 Discussion	157
References		159

ACKNOWLEDGEMENTS

I would like to express my sincere appreciation to Dr. Christopher A. Del Negro, under whose guidance this investigation was conducted, for his patience and constructive criticism throughout the investigation. I am also indebted to Dr. Gregory D. Conradi Smith, Dr. Eric L. Bradley, and Dr. Robin C. Looft-Wilson for their careful reading and critique of the manuscript. I would like to thank Krishanthi Weragalaracchihi for paving the way for studying the morphology of our respiratory neurons. I would like to thank my colleagues in the Del Negro lab and our collaborators who were instrumental in the completion of this work. I am truly grateful for the William & Mary professors, alumni, and staff who instilled a sense of belonging and camaraderie within me during my journey.

I would also like to express my deepest heartfelt thanks to my mom, dad, family and friends for their love and support throughout my academic and scientific career.

I dedicate this dissertation to my mom, Marion Akins. She has always encouraged me and inspired me. My accomplishments in life would not be possible without her.

LIST OF TABLES

1. Sample SWC file data for digital neuron reconstruction	47
2. Definitions of morphometric properties analyzed	89
3. Morphometric properties of preBötC Dbx1 neurons	92
4. Morphometric properties of reticular formation Dbx1 neurons	99
5. Mann Whitney U test comparison of morphometric data obtained from L-measure for Dbx1 preBötC and reticular formation neurons	106
6. Sholl analysis branch point data and Mann Whitney U test	111
7. Sholl analysis dendritic length data and Mann Whitney U test	112
8. Sholl analysis dendritic volume data and Mann Whitney U test	113
9. Sholl analysis dendritic surface area data and Mann Whitney U test	114

LIST OF FIGURES

1. Anatomy of the respiratory system	7
2. Sagittal views of the brainstem demonstrating neural circuitry	9
3. Visualization of Dbx1 neurons in transverse brainstem sections from <i>Dbx1^{+/CreERT2}; Rosa^{26tdTomato}</i> reporter mice	15
4. Characteristic physiology of a respiratory preBötC Dbx1 neuron	17
5. Heat map of Trp mRNA expression from single neurons analyzed through RNA sequencing (RNASeq)	25
6. Firing patterns from neurons with identical ion channel distributions but various dendritic morphologies	28
7. Effect of electrical coupling on neuronal firing pattern in a two-compartment model	29
8. Respiratory Dbx1 preBötC neurons (A-C) tend to exhibit commissural axons, while respiratory non-Dbx1 preBötC neurons (D-F) have ipsilaterally projecting axons	31
9. Respiratory Dbx1 preBötC neurons (A-C) have a smaller projection in the rostrocaudal plane than respiratory non-Dbx1 preBötC neurons (D-F)	32
10. Workflow diagram for digital neuronal reconstructions	42
11. Dbx1 inspiratory cell 130624 in the reticular formation	67
12. Dbx1 inspiratory cell 140114 in the reticular formation	68
13. Dbx1 inspiratory cell 140120 in the reticular formation	69
14. Dbx1 inspiratory cell 140124 in the reticular formation	70
15. Dbx1 inspiratory cell 140207 in the reticular formation	71
16. Dbx1 inspiratory cell 140221 in the reticular formation	72

17. Dbx1 inspiratory cell 140306 in the reticular formation	73
18. Dbx1 inspiratory cell 140208 in the reticular formation	74
19. Dbx1 inspiratory cell 140220 in the reticular formation	75
20. Dbx1 inspiratory cell 140301 in the reticular formation	76
21. Dbx1 inspiratory cell 140127 in the preBötC	77
22. Dbx1 inspiratory cell 140109 in the preBötC	78
23. Dbx1 inspiratory cell 140117 in the preBötC	79
24. Dbx1 inspiratory cell 130910 in the preBötC	80
25. Dbx1 inspiratory cell 1 130212_1 in the preBötC	81
26. Dbx1 inspiratory cell 130625 in the preBötC	82
27. Dbx1 inspiratory cell 130819 in the preBötC	83
28. Dbx1 inspiratory cell 140110 in the preBötC	84
29. Dbx1 inspiratory cell 120417 in the preBötC	85
30. Dbx1 inspiratory cell 130212_2 in the preBötC	86
31. Dbx1 inspiratory cell 120621 in the preBötC	87
32. Dbx1 inspiratory cell 120623 in the preBötC	88
33. Trpc3 expression in Dbx1 and non-Dbx1 preBötC neurons of adult mice	134
34. Trpc3 expression in Dbx1 and non-Dbx1 preBötC neurons of neonatal mice	135
35. Nav1.6 monoclonal immunohistochemistry in neonatal mice	136
36. Nav1.6 polyclonal immunohistochemistry in neonatal mice	137

37. GRP receptors on Dbx1 and non-Dbx1 preBötC neurons in neonatal mice	151
38. GRP receptors not present on glia in preBötC of neonatal mice	152
39. GRP receptors on Dbx1 and non-Dbx1 neurons in adult mice	153
40. NMB receptors on Dbx1 and non-Dbx1 neurons in neonatal mice	155
41. NMB receptors on Dbx1 and non-Dbx1 neurons in adult mice	156

LITERATURE REVIEW

Neural origins of breathing behavior are experimentally accessible

Neuroscience aims to understand how the brain and nervous system produce behaviors through molecular, cellular, and network levels of analysis. A behavior with obvious physiological importance is breathing, which refers to periodic movements of the diaphragm, airways, and thorax, that tidally ventilate the lungs to support pulmonary gas exchange and ultimately aerobic respiration. Breathing is a constant, yet dynamic behavior that changes in response to different levels of physiological demand during exercise, sleep, and emotional states. Breathing must function harmoniously with actions such as swallowing, speaking, laughing, and crying in humans, and whisking and sniffing in rodents. Breathing begins at birth (although mock breathing movements occur episodically during embryonic development) and breathing continues uninterrupted to maintain life and homeostasis in all terrestrial mammals, including notably human beings. Therefore, the neural origin of breathing presents an important puzzle to solve. Nevertheless, the neural networks that generate and control breathing remain incompletely understood.

Understanding respiratory neural networks is a large problem; this dissertation will approach only limited aspects of it. By examining morphological properties of respiratory neurons including their dendritic structure and their axon projections, we gain insight into their synaptic integration and potential network

connectivity. Through further characterization of intrinsic membrane properties such as ion channel and peptide receptor expression, one can develop a better understanding of the physiological mechanisms underlying respiratory rhythmogenesis and other respiratory-related behaviors such as sighing or gasping. This dissertation aims to use those anatomical methods to develop insights into breathing's neural underpinnings.

The respiratory rhythm and the essential underlying motor pattern for breathing movements are generated by a network of neurons in the brainstem. Malfunctions in the respiratory neural circuit can lead to serious morbidity and mortality in humans. For example, premature infants can suffer apnea of prematurity due to an incomplete development of the respiratory network (Di Fiore et al., 2013; Martin and Wilson, 2012). Adults can also suffer from sleep-disordered breathing (Gaig and Iranzo, 2012) and obstructive sleep apnea (Tahmasian et al., 2016). Fatal respiratory failure is associated with neurodegenerative disorders such as Alzheimer's disease, Parkinson's disease, and multiple systems atrophy because such disorders appear to cause collateral damage to medullary respiratory circuits that putatively disrupt their respiratory functionality (Benarroch, 2003; Benarroch et al., 2003; Brunnström and Englund, 2009; Tuppy et al., 2015). Failure to adequately respond to rising carbon dioxide dissolved in the blood and cerebrospinal fluid (hypercapnia) is linked to breathing disturbances including sleep disordered breathing and may be involved in sudden infant death syndrome through an insufficient response to hypoxia or hypercapnia (Darnall, 2013; Garcia III et al., 2013; Guyenet and Bayliss, 2015).

Genetic mutations can also lead to respiratory problems. For example, Rett's syndrome is caused by a mutation in the *MECP2* gene (Amir et al., 1999) and leads to breathing abnormalities including hypoventilation and desynchronization of the cardiac and respiratory systems (Julu et al., 2001; Weese-Mayer et al., 2008). Also, people who suffer from a condition known as congenital central hypoventilation syndrome (CCHS, also known as "Ondine's curse") fail to respond normally to hypercapnia, and can cause respiratory arrest while sleeping; CCHS is the result of poly-alanine mutations of the *PHOX2B* gene which cause frameshifts that translate into mutant proteins and the disease phenotype, which is the destruction of chemosensitive neurons that provide the excitatory drive to breathe (Amiel et al., 2003; Dubreuil et al., 2008).

Understanding the neural origins of respiratory rhythm and pattern generation provides a baseline knowledge level that we can apply to understand respiratory pathology, which leads to enhanced therapies and prophylaxis of breathing disorders with etiologies related to brain and central nervous system (CNS) dysfunction.

Rhythmic behaviors, such as breathing, chewing, and walking, are driven by central pattern generators (CPGs) in the brainstem and spinal cord (Grillner, 2006; Kiehn, 2016; Westberg and Kolta, 2011). CPGs are networks of neurons that can generate periodic signals without any rhythmic external input (for example from other neural centers) or sensory feedback. CPGs produce rhythmic activity that drives premotor and motor neurons, which leads to motor output, i.e., movements (Frigon, 2012; Grillner, 2006; Guertin, 2013).

However, CPG rhythms are not rigid; sensory feedback and higher cortical commands must be accommodated and integrated so that behaviors in real environments respond to internal demands of the organism and demands imposed by the external world and environment. CPG operation and function is quite well understood in simpler invertebrate model systems (Marder et al., 2015; Nusbaum and Blitz, 2012), and in non-mammalian vertebrates considerable progress has been made in the past decade (Grillner and Manira, 2015; Kiehn, 2016; McLean and Dougherty, 2015). We aim to achieve the same level of understanding in a canonical rhythmic motor behavior in a mammalian species. This dissertation focuses on the CPG that drives breathing in mammals.

The breathing behaviors pertinent to this dissertation are eupneic breathing, or normal breathing, and sighs, which are necessary for proper lung function because they overinflate alveoli to reduce surface tension and prevent their collapse. The breathing movements involved with eupnea and sighs originate due to a neural rhythm, a periodic signal composed of burst discharges from interneurons, as well as a distinct motor pattern, which is mediated by premotor neurons and conveyed ultimately to motoneurons. The respiratory movements themselves involve airway resistance muscles and pump muscles responsible for tidal ventilation, consisting of inspiration (air in) and expiration (air out). A thorough understanding of respiratory rhythm and motor pattern generation mandates analyses ranging from a behavioral level, followed by more detailed neurophysiological examinations of the respiratory network (considered as a whole microcircuit), to an in-depth analysis of cellular and molecular

properties of individual neurons to determine their role in producing network activity.

This dissertation investigates three morphological and anatomical aspects of neurons that generate the respiratory rhythm and motor pattern. First, morphometric properties of respiratory rhythm-generating neurons are compared to neurons involved with respiratory motor pattern generation to ascertain potential distinctions and specializations pertaining to their synaptic integration properties. Next, the expression of ion channels that carry intrinsic membrane currents that may influence respiratory rhythm and pattern generation is examined on respiratory rhythm-generating neurons. Finally, the involvement of glia or neurons in sighing behavior will be investigated through the presence of peptide receptors shown to evoke sighs.

Respiratory system anatomy

The respiratory rhythm and motor pattern in mammals is governed by a neural network that resides in the medulla. The neurons that govern the respiratory rhythm and pattern generate the necessary periodic timing for breathing, integrate sensory information, such as CO₂ and O₂ levels, and send signals to motor neurons to generate respiratory motor output (Guyenet and Bayliss, 2015; Guyenet et al., 2009). Medullary neurons control muscles involved in respiratory motor output including the diaphragm which separates the thoracic cavity from the abdominal cavity and is the predominant pump for breathing, the tongue, and intercostal muscles which are in between the ribs. The thoracic

cavity consists of the ribs, vertebral column, and sternum encases the lungs, middle, and lower airways (Figure 1).

During the intake of breath, known as inspiration, air enters the upper airway through the mouth or nasal cavity. The tongue protrudes slightly to open the airway and maintain airway patency during the breath. The thoracic cavity expands as the diaphragm and external intercostal muscles contract, which drives air to enter the bronchi and the air-filled sacks of lungs (alveoli) due to the drop in the pressure gradient (Feldman and Del Negro, 2006). During expiration, breath is expelled from the chest cavity. At rest, the diaphragm relaxes and its passive recoil returns the lungs to their functional residual volume (i.e., normal resting volume). Expiration occurs in two sub-phases (Guyenet et al., 2005; Janczewski and Feldman, 2006). Post-inspiration is the first sub-phase, during which resistance muscles constrict the airways and can cause an eccentric contraction of the diaphragm if necessary, both of which increase time for gas exchange in the lungs. Second is the E2 phase (second stage expiration), which is not driven by any active muscle contraction at rest, but does involve active contraction of expiratory muscles such as abdominals and internal intercostal muscles during increased respiratory demand. This dissertation focuses on the neuroscience of the inspiratory rhythm and motor pattern, whereas the physical plant for breathing, involving muscles and organs, pertains more to pulmonary physiology.

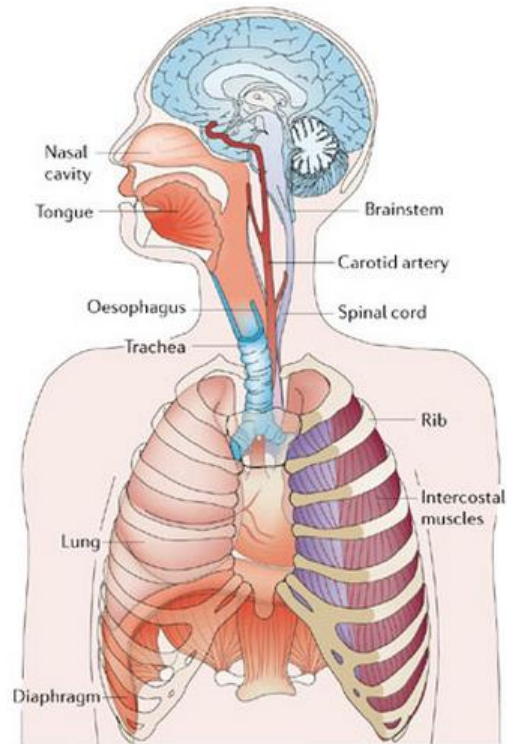


Figure 1. Anatomy of the respiratory system (from Box 1, Feldman and Del Negro, 2006). The neural circuit that governs the respiratory rhythm and motor pattern resides in the brainstem. Signals are sent from neurons in the brainstem to organs and muscles required for taking a breath including the genioglossus tongue muscle and diaphragm.

Respiratory and pattern rhythm generation

The brain and CNS are extensively interconnected. However, the concept of *microcircuits* enables neuroscientists to analyze the brain and CNS in smaller more manageable constituent parts. Having an identified function and taking up a limited amount of brain real estate, a neuronal microcircuit is characterized by having specific inputs, containing interneurons whose axon projections and synaptic contacts remain within the microcircuit, and ultimately featuring principal neurons whose axons make up the output of the system and thus project to other

parts of the brain and CNS (Shepherd, 2004). Interneurons can facilitate communication between groups of neurons (e.g., between sensory neurons and motor neurons) or within populations of neurons. In the respiratory rhythm-generating microcircuit, the rhythm is generated by interneurons, but can be modulated by sensory input sources such as lung mechanoreceptors (Dutschmann et al., 2014) and central/peripheral chemoreceptors (Guyenet and Bayliss, 2015; Guyenet et al., 2009), and its principal neurons consist of cranial and spinal motor nuclei, whose output results in breathing movements. Normal breathing, or eupnea, involves motor output, coordination of breathing with orofacial behaviors (Kleinfeld et al., 2014; Moore et al., 2013), and integration of chemosensory inputs, all of which function based on a rhythm.

The site for rhythm generation, specifically the inspiratory rhythm, is the preBötzinger Complex (Feldman and Del Negro, 2006; Feldman et al., 2013; Ramirez et al., 2016; Smith et al., 1991), which is located within the ventral medulla. During a breath, the cranial hypoglossal nerve (CN XII) facilitates tongue protrusion to maintain an open airway (Fregosi and Ludlow, 2014), thoracic nerves T1-T11 facilitate the movement of the external intercostal muscles and the phrenic nerve controls the diaphragm. The output from these nerves that facilitate respiratory motor output is in phase with the neurons governing the breathing rhythm.

The preBötzinger Complex (preBötC), a functionally and anatomically specialized region of the ventrolateral medullary brainstem is the CPG for the inspiratory rhythm (Feldman et al., 2013; Gray, 1999; Gray et al., 2001; Moore et

al., 2013; Smith et al., 1991; Tan et al., 2008). Rhythmogenic neurons in the preBötC send signals to various neuron populations, demonstrated in Figure 2, including other respiratory regions and premotor neuron populations.

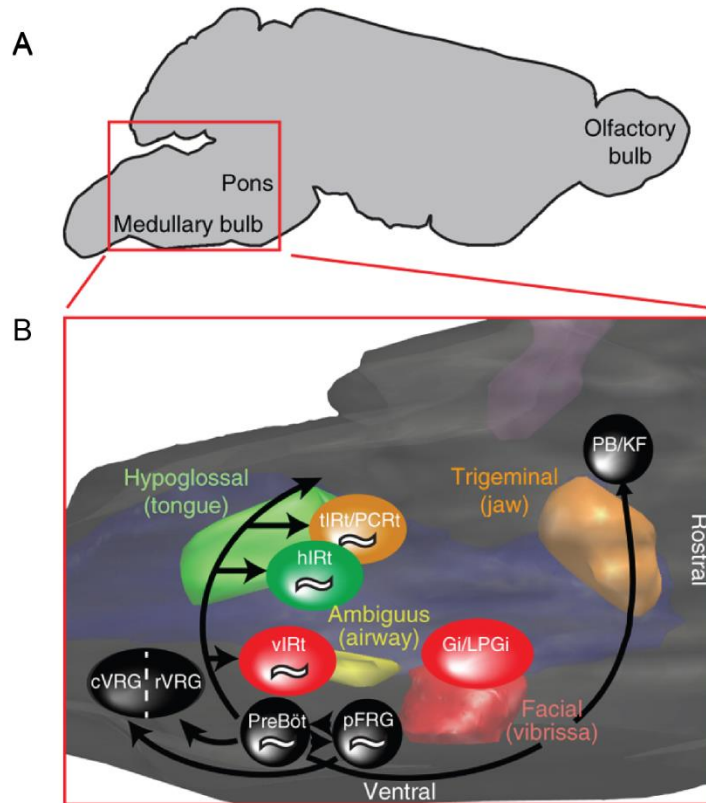


Figure 2. Sagittal views of the brainstem demonstrating neural circuitry (Kleinfeld et al., 2014). A, outline of brainstem, parasagittal view, with enlarged view of pons and medulla in B. B, black circles and arrows indicate respiratory regions, whisking regions are shown in red, chewing regions are shown in orange, and licking regions are shown in green. The yellow shaded region represents the population of cranial motor neurons that control the airway, the green region represents the population of motor neurons governing tongue movements. The preBötC, the site of inspiratory rhythm generation, sends information to various neuron populations including the vibrissa and hypoglossal intermediate reticular formations (vIRt and hIRt), caudal and rostral ventral respiratory groups (cVRG and rVRG). The rVRG is important for the inspiratory drive pattern and the cVRG is important for expiration.

To generate respiratory related motor output such as tongue protrusion and diaphragm contraction, a subset of premotor neurons transmit signals to genioglossus and phrenic motoneuron populations respectively (Chamberlin et

al., 2007; Koizumi et al., 2008; Peever et al., 2002; Smith et al., 1990; Volgin et al., 2008). The rostral ventral respiratory group (rVRG) contains glutamatergic premotor neurons that project to the phrenic nucleus and spinal cord, innervating the diaphragm and external intercostal motoneurons (Ellenberger and Feldman, 1990, 1994; Ellenberger et al., 1990).

To further classify respiratory neurons, we must be able to distinguish key neurons within the respiratory microcircuit from one another. Specific combinations of transcription factors, which control gene expression, are vital to neuronal development and can provide markers for neuron subpopulations (Alaynick et al., 2011; Garcia-Campmany et al., 2010; Gray, 2008, 2013). Using transcription factors as a marker allows us to classify populations of neurons within the respiratory neural network.

Genetic classification of respiratory rhythm-generating neurons

The temporal and spatial expression of transcription factors, genes that control other genes, give rise to the different types and classifications of neurons (and glia) in the brainstem and spinal cord (Garcia-Campmany et al., 2010; Grillner and Jessell, 2009). The formation of the respiratory central pattern generator may rely strongly on genetic components, evident through unstable respiratory rhythm and fatalities in mice with mutations in transcription factors involved in hindbrain interneuron specification (Blanchi et al., 2003; Gray et al., 2010; Jacquin et al., 1996; Pagliardini et al., 2008; Rose et al., 2009). Thirteen

different dorso-ventral domains of the brainstem can be distinguished by transcription factor expression (Alaynick et al., 2011). Dorsal domains pertain to sensory function and sensorimotor integration. The ventral domains are associated with CPGs and motor output functions. The ventral neural tube contains V0, V1, V2, VMN, and V3 domains. V0, V1, V2, and V3 make up interneurons, whereas VMN makes up motoneurons. In the hindbrain, the progenitor of the mature brainstem, the putative respiratory rhythm-generating interneurons reside within the V0 population (and the V3 population makes up visceral vagal motoneurons) (Briscoe and Ericson, 1999).

The V0 domain has two main subdivisions: dorsal and ventral. The dorsal V0 population are mainly GABAergic while the ventral V0 population are glutamatergic (Lanuza et al., 2004; Moran-Rivard et al., 2001; Pierani et al., 2001). Rhythmogenesis *in vitro* requires excitatory, glutamatergic transmission (Funk et al., 1993; Wallen-Mackenzie et al., 2006) and is modulated by peptidergic transmission (Rekling et al., 1996; Tupal et al., 2014; Li et al., 2016; Gray et al., 1999). Regular breathing depends upon rhythm-generating neurons that express receptors for neurokinin-1 (NK1R) demonstrated when *in vivo* saporin-mediated metabolic poisoning of NK1R-expressing neurons caused rats to develop ataxic breathing (Gray et al., 2001) as well as sleep-disordered breathing (McKay et al., 2005). Additionally, applying the NK1R agonist substance P, which depolarizes preBötC neurons and accelerates breathing rhythms, to the preBötC of adult rats *in vitro* increased the frequency of respiratory behavior (Gray et al., 1999), suggesting the depolarized preBötC

neurons are responsible for respiratory rhythm generation. However, NK1R-expressing preBötC neurons are not sufficient for respiratory rhythmogenesis. First of all, the NK1R-expressing cell-ablated rats (above) exhibited severe respiratory pathology, but did not die of respiratory failure. Moreover, silencing neurons that express the peptide somatostatin (SST) results in persistent apnea (Tan et al., 2008), which suggests that a class of SST-expressing neurons could define the core oscillator (although that depends to what extent NK1R and SST co-express in preBötC neurons, see below). In neonatal mice, NK1R expression extends (caudally) from the lateral reticular nucleus to the facial nucleus (rostrally) and includes the retrotrapezoid nucleus (RTN) and the parafacial respiratory group (pFRG). Also in the region of the preBötC and its rostrally sited neighbor the Böttinger complex, NK1R labeling extends to pharyngeal and oesophageal motoneurons of the compact and semicompact nucleus ambiguus (Bieger and Hopkins, 1987; Gray et al., 1999). so this marker alone cannot define the inspiratory rhythmogenic core (Gray et al., 1999; Stornetta et al., 2003; Thoby-Brisson et al., 2009). However, NK1R-expressing neurons can overlap with SST-expressing neurons. Glutamatergic, peptidergic, and peptide receptor-expressing interneurons in the preBötC develop from the V0 ventral post-mitotic domain, where the homeodomain transcription factor *Dbx1* is expressed pre-mitotically. During embryonic development, *Dbx1*-expressing precursors are the sole source of glutamatergic interneurons in the preBötC (Bouvier et al., 2010; Gray et al., 2010).

Dbx1 expression is necessary for respiration; without *Dbx1*, mice die at birth without ever taking a breath because the preBötC never forms (Bouvier et al., 2010; Gray et al., 2010). *Dbx1*-derived neurons (hereafter *Dbx1* neurons) are the putative rhythmogenic neurons in the preBötC. Laser ablation of *Dbx1* neurons in the preBötC slows and eventually abolishes the respiratory rhythm, indicating their requirement for respiratory rhythm generation (Wang et al., 2014). Also, transient optogenetic hyperpolarization of *Dbx1* preBötC neurons results in a disruption of the respiratory rhythm *in vitro* and in lightly sedated intact mice *in vivo*; when fully awake, optogenetic hyperpolarization of *Dbx1* preBötC neurons causes a reduction in breathing frequency (Vann et al., 2016). Optogenetic photostimulation *in vivo* of *Dbx1* preBötC neurons expressing channelrhodopsin (ChR2) resulted in inspiratory firing patterns and excitatory effects of burst timing and pattern (Cui et al., 2016). Also, selective photoinhibition of Archaeodopsin-3 (Arch) expressing preBötC neurons that were *Dbx1*-derived, SST-expressing, or glutamatergic neurons demonstrated that the three populations have similar respiratory rhythmogenic properties (Koizumi et al., 2016). These studies suggest the significant role of *Dbx1* neurons in respiratory rhythm generation, but there is more to learn of their connectivity within the microcircuit, synaptic integration, ion channels that could give rise to rhythmogenic currents, and peptide receptors. This dissertation will elucidate morphological and anatomical information about respiratory *Dbx1* neurons, giving insight into their potential network connectivity, synaptic integration properties, and properties contributing to respiratory rhythm and pattern generation.

Dbx1 neurons in respiratory rhythm and pattern generation

Dbx1 neurons are found throughout the brain. Their role(s) have been studied in the amygdala, the hypothalamus (Hirata et al., 2009; Lischinsky et al.; Sokolowski et al., 2015, 2016), the brainstem respiratory microcircuit, and in lumbar spinal cord locomotor microcircuits (Bouvier et al., 2010; Gray et al., 2010; Hirata et al., 2009; Pierani et al., 2001). Dbx1 neurons are involved in a variety of behaviors. For instance, Dbx1 neurons in the lumbar spinal cord drive motor neurons and are vital for controlling motor neurons responsible for left-right alternation in hindlimb muscles (Lanuza et al., 2004; Talpalar et al., 2013). Dbx1 neurons in the hypothalamus may also regulate stress responses (Sokolowski et al., 2015). We are most interested in Dbx1 expression in the brainstem and spinal cord because these neurons are involved in CPGs. Dbx1 is expressed in respiratory regions of the brain outside of the preBötC including the intermediate reticular formation. The intermediate reticular formation contains a mixture of premotor neurons, some of which govern oral-motor coordination (Gestreau et al., 2005; Kleinfeld et al., 2014; Moore et al., 2013). When precursor cells expressing Dbx1 are labeled with a fluorescent marker at embryonic day 10.5, transverse brain slices near the level of the preBötzinger complex and reticular formation exhibit an inverted U-shape pattern of fluorescent cells in neonatal mice from postnatal day 0 to 5 as demonstrated in Figure 3.

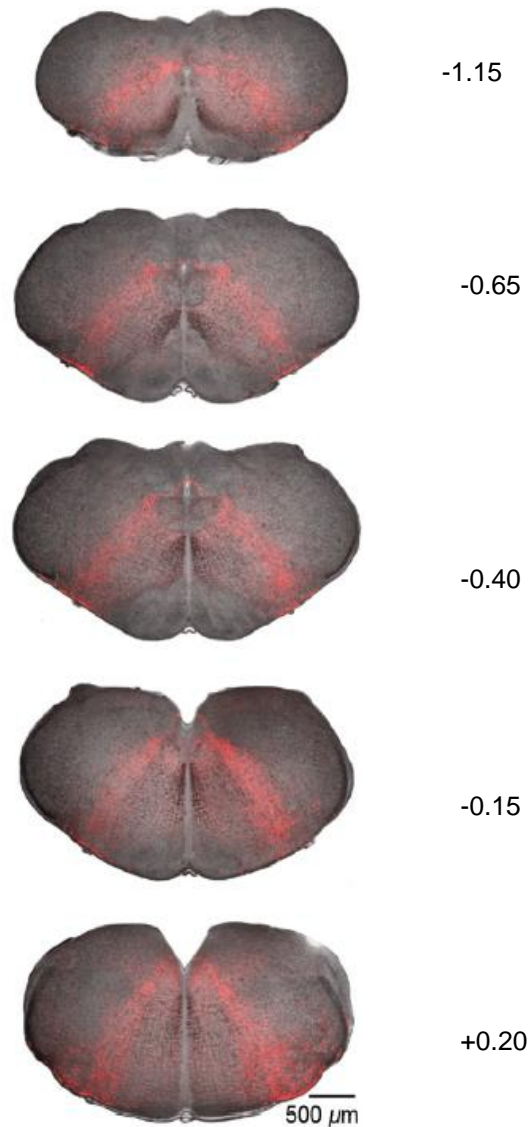


Figure 3. Visualization of *Dbx1* neurons in transverse brainstem sections from *Dbx1^{+/CreERT2}; Rosa26^{tdTomato}* reporter mice. *Dbx1* neurons have been labeled via induced expression of the red fluorescent protein tdTomato at embryonic day 10.5. Distances from the facial cranial nucleus (VII) are indicated to the right of each section. The preBötC is located at -0.40 μm from the facial nerve (Ruangkittisakul et al., 2014)

Respiratory modulated premotor neurons known to be located in the intermediate reticular formation include trigeminal premotor neurons, hypoglossal premotor neurons, and vibrissa premotor neurons (Kleinfeld et al., 2014; Revill et al., 2015; Stanek et al., 2014). The study by Revill et al. in particular showed that

hypoglossal respiratory premotor neurons are *Dbx1*-derived, although the genetic origins of the other respiratory and orofacial reticular neurons remain uncharacterized. *Dbx1*-derived hypoglossal premotor neurons exist in the preBötC as well as the reticular formation (Revill et al., 2015; Song et al., 2016; Wang et al., 2014). The role of respiratory *Dbx1* neurons in the reticular formation is beginning to be unraveled through morphological and physiological analyses, which will be further discussed in this dissertation.

Neurophysiology of respiratory rhythm generation

In the last few decades, neuroscientists have exploited the experimental advantages offered by respiratory rhythms that can be studied in reduced breathing model systems *in vitro*. In 1984, Suzue determined that rhythmic neural activity can be recorded from cranial and spinal respiratory nerves of a brainstem-spinal cord preparation from newborn rats and that neural activity matched the movements of the ribcage when left semi-intact, indicating rhythmic neural activity was respiratory (Suzue, 1984). In a more thorough analysis of respiratory nerve activities *in vitro* and their cellular bases, Smith et al. confirmed Suzue's initial conclusion that rhythmic activity in the isolated brainstem and spinal cord was breathing-related and amenable to investigate the cellular and synaptic mechanisms underlying respiratory rhythm and motor pattern (Smith et al., 1990).

Further reduction of the brainstem-spinal cord preparation led to the development of a medullary slice preparation that retains fictive rhythmic respiratory activity when the preBötC is included in the slice (Funk et al., 1993; Smith et al., 1991). From these transverse slices that are 350-550 μm thick, rhythmic fictive respiratory activity, depicted in Figure 4, can be recorded from nerves and individual cells (Smith et al., 1991; Funk et al., 1993; Ruangkittisakul et al., 2006; Funk and Greer, 2013).

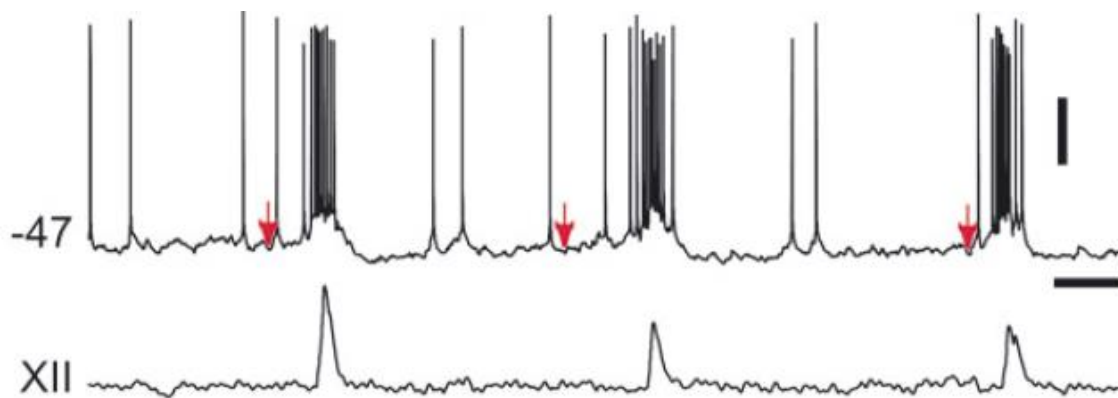


Figure 4. Characteristic physiology of a Dbx1 neuron in the preBötC (Picardo et al., 2013). The top physiological trace shows a whole-cell recording of a respiratory Dbx1 neuron with a baseline activity level of -47 mV. The bottom physiological trace is the integrated output of the hypoglossal cranial nerve (XII). The respiratory Dbx1 neuron is active during the inter-inspiratory burst interval, which is the interval between peak XII activity. The respiratory Dbx1 neuron also displays voltage dependent spike inactivation known as depolarization block. Red arrows signify where the inspiratory drive begins. The horizontal scale bar is 1s and the vertical scale bar is 20 mV.

During the inspiratory phase of respiration, Dbx1 preBötC neurons exhibit synchronous bursts of 300-500 ms *in vitro* (Funk and Greer, 2013). Individually, Dbx1 preBötC neurons produce bursts of 10 to 30 mV amplitudes; the underlying envelope of depolarization has been characterized as the *inspiratory drive potential*. This dissertation will analyze the morphological and anatomical properties of neurons governing this inspiratory drive.

Understanding rhythm generation in central pattern-generating networks presents a formidable challenge. Three prominent theories, explained in the following sections, emerged that describe rhythmogenesis in central pattern generating networks. The first theory involves inhibition, the second involves autorhythmic pacemaker neurons, and the third is based on emergent network properties.

Respiratory rhythm through phasic inhibition

The hypothesis of respiratory rhythm generation through cyclic inhibition consists of three neuron populations: early-inspiratory neurons in the preBötC, postinspiratory BötC neurons and augmenting-expiratory BötC neurons (Janczewski et al., 2013). Inhibition was thought to terminate inspiratory bursts and facilitate expiration. Inspiratory and expiratory patterns were thought to be kept as separate processes through reciprocal inhibition (Euler, 1983; Feldman, 2011).

Several studies have investigated the role of inhibitory neurons in respiratory rhythm generation, since inhibition has been hypothesized to guide rhythmic behaviors such as locomotion and chewing since the early 1900s (Brown, 1914). In 2013, the effect of postsynaptic inhibitory transmission in respiratory rhythm generation was analyzed by blocking GABA_A and glycine receptors in preBötC and BötC neurons; but the breathing rhythm persisted indicating postsynaptic inhibition is not required for respiratory rhythm generation

(Janczewski et al., 2013). Another study of inhibitory preBötC neurons in 2015 involved expressing either channelrhodopsin-2 or archaerodopsin in glycinergic (inhibitory) preBötC neurons in mice (Sherman et al., 2015). Photostimulation of glycinergic preBötC neurons in channelrhodopsin-2 transfected mice ends inspiration prematurely while photostimulation during the expiratory phase delays the start of the next inspiratory cycle (Sherman et al., 2015). In archaerodopsin-transfected mice, photoinhibition of glycinergic neurons causes an increase in tidal volume but does not change inspiratory duration (Sherman et al., 2015). These results indicate that inhibitory glycinergic preBötC neurons can modify inspiration, but are not required for rhythm generation since the rhythm persists after optogenetic dampening.

In 2016, to disrupt inhibition within the preBötC or BötC, GABA_A and glycine receptors in the preBötC or BötC in *in situ* (reduced) and anesthetized *in vivo* rat preparations were blocked with antagonists gabazine and strychnine while suppressing preBötC or BötC neuronal activity with a muscimol microinjection. This disruption of inhibition perturbed the respiratory rhythm frequency and motor pattern; in some cases the motor output was terminated (Marchenko et al., 2016). In this case, changes in rhythmic frequency might be attributable to elevated excitability caused by disinhibition of the respiratory network creating an induced state of hyperexcitability such that motor activity is tonic rather than rhythmic. However, modulation of the rhythm, even inducing a tonic state, shows that chloride-mediated synaptic inhibition is not necessary for

rhythm generation. Phasic inhibition does not adequately explain respiratory rhythm generation, so other theories emerged.

Pacemaker hypothesis

Another theory of respiratory rhythm generation, which became widely accepted because of its precedents in invertebrate and cardiac systems, involves pacemaker neurons that are autorhythmic. Autorhythmicity refers to neurons that are intrinsically rhythmically active, generating brief bursts of spiking activity (~250 ms duration) separated by periods of quiescence (2-5 sec duration) when synaptically isolated. This theory evolved because the respiratory rhythm persists in *en bloc* and slice and preparations containing the preBötC after postsynaptic inhibition has been blocked (Ballanyi et al., 1999; Feldman and Smith, 1989). A subset of preBötC neurons that exhibit voltage-dependent bursting properties and depend on the persistent sodium current (I_{NaP}) were discovered in the preBötC and it was quickly suspected that these intrinsic bursting neurons might be rhythmogenic pacemakers for the network (Del Negro et al., 2002a; Smith et al., 1991). However, pacemaker activity is not required for respiratory rhythm generation because when voltage-dependent bursting behavior is terminated in preBötC neurons, rhythmogenesis still occurs (Del Negro et al., 2002b) and bath application of riluzole does not affect respiratory motor output (Del Negro et al., 2005). Experiments blocking I_{NaP} with riluzole and tetrodotoxin (TTX) in thin neonatal rat slices (250 – 350 μm) and preBötC islands do stop the rhythm

(Koizumi and Smith, 2008), but only produce small disturbances in more intact preparations (Paton et al., 2006; Smith et al., 2007). Additionally, when similar experimental methods were applied to thicker slices (500-550 μm) in neonatal mice that contain the preBötC and surrounding network components, the respiratory rhythm was not disrupted (Pace et al., 2007a). In the embryonic preBötC, attenuation of I_{NaP} at embryonic day 16.5 (E16.5) decreased respiratory rhythm frequency and blockade of I_{NaP} and the nonspecific cation current I_{CAN} blocked network activity, but at E18.5, after the embryo switched from a purely I_{NaP}/I_{CAN} driven network to a combined network and pacemaker network the same blockade did not completely silence network activity (Chevalier et al.). Thus far, pharmacological experiments testing the pacemaker hypothesis either do not stop the respiratory rhythm, use drugs that could affect synaptic transmission or ion channels, or do not produce comparable results between experimental preparations, species, or developmental stages; therefore, autorhythmic neurons alone cannot explain respiratory rhythm generation (Del Negro et al., 2005; Pace et al., 2007a).

Neither the pacemaker hypothesis nor phasic inhibition can explain respiratory rhythmogenesis; each theory has been falsified by experimental data. Another hypothesis, the group-pacemaker, is based on emergent network properties, and provides an alternative to explain respiratory rhythmogenesis that is (at least at present) consistent with the existing data.

Group-pacemaker hypothesis

A group-pacemaker hypothesis is a proposed, alternative theory to intrinsic pacemakers and phasic inhibition that describes respiratory rhythm generation. Group-pacemaker behavior is an emergent network property; no individual neuron recaps network activity via its intrinsic bursting-pacemaker properties in the absence of synaptic transmission. According to the group pacemaker, the collective activity of the network's constituent neurons produces the respiratory rhythm in the preBötC (Del Negro et al., 2002b, 2010). In a group-pacemaker system, a set of intrinsic currents is normally inactive or latent within the constituent neurons. These latent intrinsic currents are evoked through synaptic activity in the context of network activity. The evoked currents result in periodic inspiratory bursts (Del Negro et al., 2010; Rekling and Feldman, 1998; Rubin et al., 2009).

In the group-pacemaker hypothesis, recurrent synaptic excitation facilitates and propagates activity similar to the way a traditional network oscillator would behave (Grillner, 2006); yet there is an additional intrinsic property of the respiratory rhythm generating neurons that make them different from traditional central pattern generating neurons.

Current data suggest glutamatergic transmission induces post synaptic calcium transients that recruit a calcium-activated nonspecific cation current, I_{CAN}

which then amplifies the synaptic currents resulting in robust inspiratory drive potentials (Crowder et al., 2007; Pace and Del Negro, 2008; Pace et al., 2007b).

There are preBötC neurons whose burst activity is reduced by Cd^{2+} , flufenamic acid, or intracellular dialysis by the Ca^{2+} chelator BAPTA, indicating that rhythmic bursting relies on Ca^{2+} and the Ca^{2+} -activated nonspecific cation current I_{CAN} (Crowder et al., 2007; Del Negro et al., 2005; Pace et al., 2007b; Peña et al., 2004). When AMPA receptors, i.e., non-NMDA ionotropic glutamate receptors, and metabotropic glutamate receptors, i.e., mGluRs, are activated, then transient postsynaptic Ca^{2+} currents or intracellular Ca^{2+} release occurs, which in turn evoke I_{CAN} . The combination of these biophysical events evokes inward currents that facilitate robust inspiratory burst generation; the resulting inspiratory bursts can be of such high amplitude that depolarization block of spiking occurs during the inspiratory burst phase. Dendritic synaptic drive resulting in Ca^{2+} influx or propagating Ca^{2+} waves evoke I_{CAN} (Del Negro et al., 2011; Mironov, 2008), while somatic Ca^{2+} transients do not contribute (Morgado-Valle et al., 2008). The role of ion channels that can generate I_{CAN} in rhythmogenic Dbx1 preBötC neurons will be further investigated in this dissertation.

Molecular and ion channel contributions to respiratory rhythmogenesis

Ion channels belonging to the transient receptor potential (Trp) super family are likely candidates leading to the generation of I_{CAN} . The Trp family of ion

channels consists of several subtypes. The most promising candidates of the Trp family of ion channels for generating I_{CAN} are Trpm4, Trpm5 (Crowder et al., 2007; Mironov, 2008; Mironov and Skorova, 2011), Trpc3, and Trpc7 (Ben-Mabrouk and Tryba, 2010). Trpm4 and Trpm5 channels exhibit biophysical properties associated with I_{CAN} such as being Ca^{2+} impermeable cation channels that are gated by intracellular Ca^{2+} and sensitive to blockade by flufenamic acid (Hofmann et al., 2003; Launay et al., 2002; Ullrich et al., 2005). Trpc3 and Trpc7 ion channels are expressed in rhythmically active ventral respiratory group neurons and may play a role in respiratory rhythm regularity (Ben-Mabrouk and Tryba, 2010), although it is not quite clear whether the authors (Ben-Mabrouk and Tryba) advocate that Trpc3 and Trpc7 comprise a tonic inward current that maintains baseline excitability in preBötC neurons or if they putatively give rise to I_{CAN} . Regardless of the authors' intent, none of their data indicate that Trpc3 or Trpc7 act phasically during burst generation, but those channels could underlie baseline excitability and could be the targets of neuromodulation.

Here, we are particularly concerned with the molecular origins of I_{CAN} , which acts phasically in the service of inspiratory burst generation. While the expression of these Trp ion channels on Dbx1 neurons has yet to be determined, mRNA of several Trp channels have been detected via PCR experiments in preBötC neurons in previous studies (Crowder et al., 2007) and through RNA sequencing shown in Figure 5. In this dissertation, I examine the morphology of Dbx1 neurons to determine if ion channels are present on Dbx1 neurons that could putatively give rise to inspiratory burst-generating currents and if Dbx1

rhythm-generating neurons are structurally different from other respiratory-modulated Dbx1 neurons.

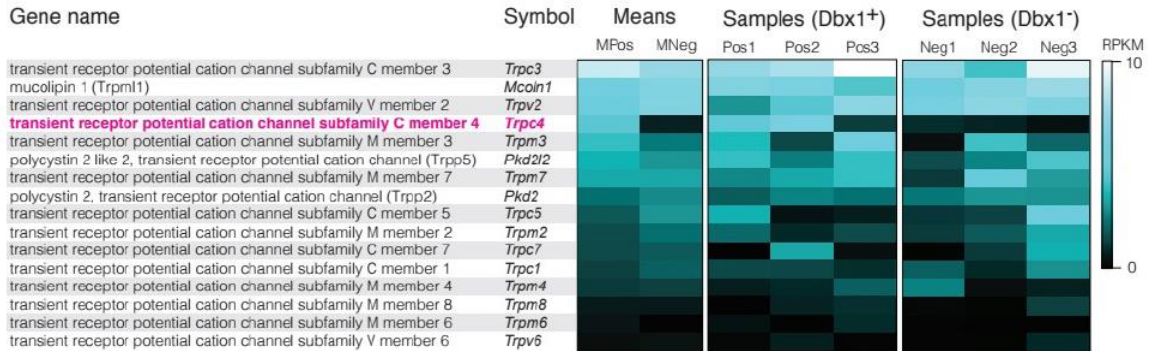


Figure 5. Heat map of Trp mRNA expression from single neurons analyzed through RNA sequencing (RNASeq). Expression levels are determined by the number of RNA copies present in terms of reads per kilobase of transcript per million mapped reads (RPKM), so high expression means a high number of RNA copies. In this heat map, low expression is designated as black and as expression levels increase the color transitions from black through teal and finally to white. In Dbx1 preBötC neurons, *Trpc3* had the highest mRNA expression. *Trpc3*, *Trpm4*, and *Trpc7* are likely candidates for the generation of the calcium activated non-specific cation current I_{CAN} . Supplementary figure from (Hayes et al., 2017).

Relationship between neuronal structure and physiology

Neural network information can be derived from anatomical studies; for example, axon projections indicate who is connected to whom in the network. Knowledge of potential neuron populations that are communicating with one another facilitates understanding network connectivity. For example, the connectivity of a neural network can influence its synchronization and robustness (Belykh et al., 2005). More specifically, we have shown the influence of network connectivity on synchronization and robustness in respiratory rhythm generation (Song et al., 2015, 2016; Wang et al., 2014). In this dissertation, we will analyze

the axon projections of respiratory-modulated neurons to determine likely recipients of their information. We will also analyze their dendritic structure to scrutinize relationships between structure and function.

The relationship between neuron morphology and function was proposed by Santiago Ramon y Cajal in the late 1800s concerning the functional organization of the nervous system. He proposed that the shape and synaptic connectivity of neurons would influence their function within a neural network (Linás, 2003). Cajal proposed the *neuron doctrine*, which stipulates that neurons comprise the information-carrying units of the nervous system, which laid the foundation for neuroscience today (Guillery, 2007).

Wilfred Rall, a founder of computational neuroscience helped establish the integrative function of dendrites showing how dendritic properties can contribute to synaptic integration in different ways including the spatiotemporal summation of excitatory post synaptic potentials (EPSPs) (Rall, 1969; Segev and Rall, 1998). Dendritic trees influence neuronal firing patterns because dendritic size and topology govern the electrotonic properties, which in turn affect how signals propagate within single cells, particularly synaptic signals that predominantly arrive at remote sites in the dendrite (rather than near the soma or axon hillock). The impact of dendritic morphology on the behavior of neurons, especially the input vs output relationship, has been studied in the classic principal neurons of the neocortex and hippocampus, i.e., layer 3 or layer 5 cortical pyramidal neurons as well as CA1 and CA3 hippocampal pyramidal neurons (Ferrante et al., 2013). Multiple studies demonstrate the impact of dendritic morphology on

the physiology of a single neuron; one study found that the dendrites of bursting neurons have a larger diameter compared with spiking neurons (Halavi et al., 2012; Komendantov and Ascoli, 2009). Dendritic structure can be examined through a Sholl analysis, which examines the branch points, dendritic volume, length and area of a neuron's dendritic arbor for specified distances from the soma to quantify dendritic geometry (Langhammer et al., 2010; Sholl, 1953). Therefore, Sholl analysis provides a way to quantify dendritic structure, which can then be applied to understand, from anatomical information alone, how a neuron might characteristically respond to its inputs to generate its output pattern. In terms of our neural microcircuit of interest, this type of Sholl analysis and dendritic electrotonic analysis could help understand how rhythmogenic (or premotor) interneurons would respond to synaptic drive in the context of rhythm- and motor-pattern generation.

A study analyzing how dendritic structure governs the firing pattern of neurons used computational neuron models to compare the ratio of the axon and somatic area to the dendritic membrane area (Mainen and Sejnowski, 1996). Neurons with the same ion channel types and ion channel densities demonstrated a range of firing patterns when only the dendritic morphology was varied. Neurons with the smallest dendritic arborizations, such as smooth stellates (Figure 6a), exhibited spike trains with monophasic afterhyperpolarization potentials and weak spike frequency adaptation. Slightly larger dendritic arbors, such as those in layer 4 spiny stellates (Figure 6b) produced adaptable spike trains. The second most extensive dendritic arbors

studied, layer 2 and 3 pyramidal neurons (Figure 6c) exhibited doublets or bursting and depolarization after spiking. The largest dendritic arbors studied, layer 5 pyramidal neurons (Figure 6d) exhibited burst spike trains (Mainen and Sejnowski, 1996).

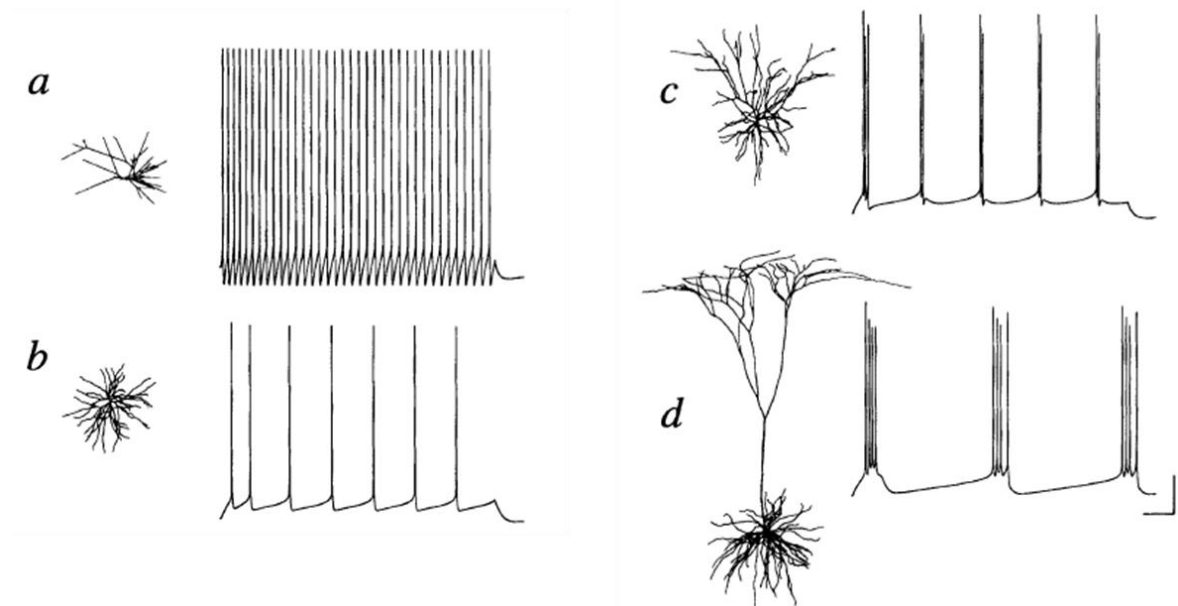


Figure 6. Firing patterns from neurons with identical ion channel distributions but various dendritic morphologies. (A) Layer 3 aspiny stellate and response to somatic current injection of 50 pA; (B) Layer 4 spiny stellate and response to 70 pA somatic current injection; (C) Layer 3 pyramidal morphology and response to 100 pA somatic current injection; (D) Layer 5 pyramid morphology and response to 200 pA somatic current injection. Scale bars: 100 ms (horizontal) and 25 mV (vertical) Adapted from (Mainen and Sejnowski, 1996).

The study also varied the coupling resistance (i.e., conductance) between the axon and somatic area to its dendritic arbor. Ion channel densities were held constant while the two ratios (area of the compartments, and the conductance coupling them) were varied systematically. Various firing patterns (Figure 7d & e) including bursting behavior were possible when weak to moderate coupling strength was used whereas the uncoupled and fully coupled models produced

spiking without after spike depolarization (Mainen and Sejnowski, 1996). This study is one of many that emphasize the significance of dendritic structure on its physiology; this concept is the focus of the first chapter of this dissertation.

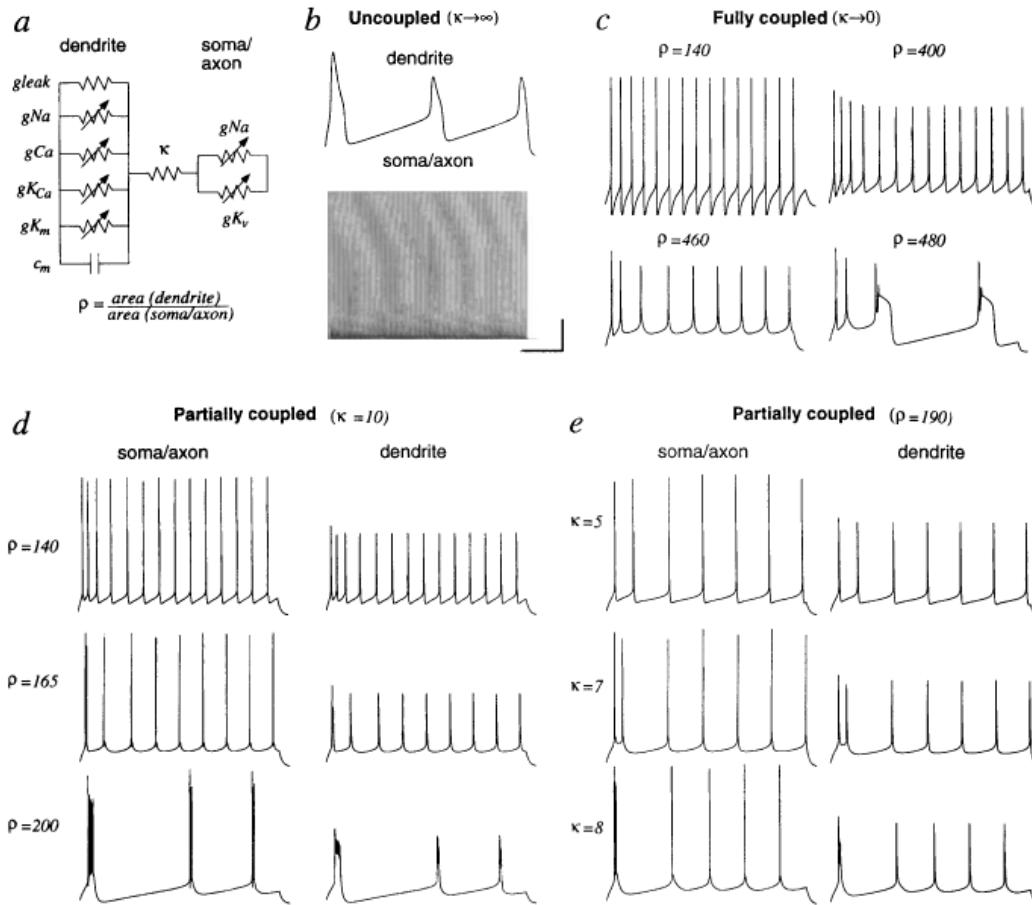


Figure 7. Effect of electrical coupling on neuronal firing pattern in a two-compartment model. A, two compartment model where κ is the electrical resistance (coupling) between the axon and soma and ρ is the ratio of dendritic to axo-somatic area; B, uncoupled dendritic (top) and axo-somatic compartments (bottom) are each capable of firing repetitively with current injected with the axo-somatic compartment firing at a much higher frequency; C, in fully coupled compartments, the spike frequency adaptation is modified by the size of the dendritic compartment indicated by ρ , but there is no bursting; D, partial coupling creates voltage gradients between axo-somatic and dendritic compartments and firing patterns change with regard to dendritic area or coupling strength (E). Adapted from (Mainen and Sejnowski, 1996).

Morphological characteristics of Dbx1 preBötC neurons

Structure-function relationships regarding the dendritic trees of neurons in the respiratory neural circuit are not yet fully understood. While important biophysical properties of Dbx1 preBötC rhythm generating neurons have been elucidated and continue to be examined, morphological and anatomical information about these neurons is necessary in order to obtain a more complete understanding of the role of these neurons in respiratory rhythmogenesis. The Del Negro lab began analyzing the morphology of Dbx1 preBötC neurons in 2011, through digital reconstructions which were presented in a master's thesis by Krishanthi Weragalaracchihi and then published in the *Journal of Physiology* (Picardo et al., 2013). Our findings, which include my reconstructions and morphometric data, were published within the *Journal of Physiology* (2013) paper are outlined below. My reconstructions of Dbx1 reticular formation neurons, which will be discussed in chapters 1 and 2, were published in eLife (Revill et al., 2015) and the Dbx1 preBötC neurons not discussed in the 2013 paper were included in the Scientific Data publication (Akins et al., 2017), which is the foundation for chapter 1.

We have learned that Dbx1 neurons in the preBötC have larger dendritic projection ranges than non-Dbx1 neighbors in the preBötC and neurons in the preBötC with commissural axon projections are mainly glutamatergic (Picardo et al., 2013). Commissural excitatory Dbx1 interneurons are of particular importance as the preBötC is a bilaterally synchronous population (Bouvier et al.,

2010; Gray et al., 2010). When compared to respiratory neurons that are not *Dbx1* derived (non-*Dbx1* neurons or *Dbx1*^{-/-}), *Dbx1* neurons had commissural axons while non-*Dbx1* neurons had more localized axon projections (Figure 8).

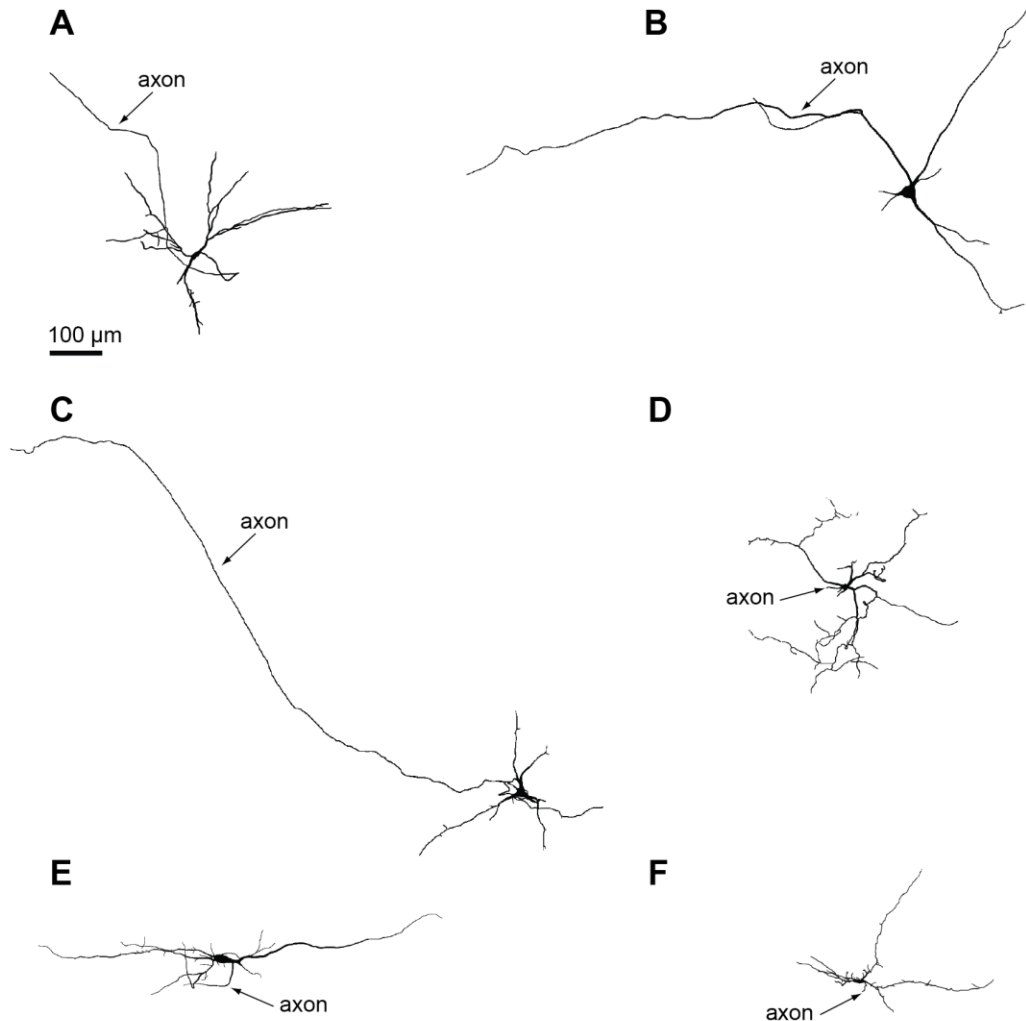


Figure 8. Respiratory *Dbx1* preBötC neurons (A-C) tend to exhibit commissural axons, while respiratory non-*Dbx1* preBötC neurons (D-F) have ipsilaterally projecting axons (Picardo et al., 2013).

Also, *Dbx1* preBötC neurons are more confined to a transverse plane (Figure 9), meaning they have less of a span in the rostral to caudal direction (Picardo et al., 2013).

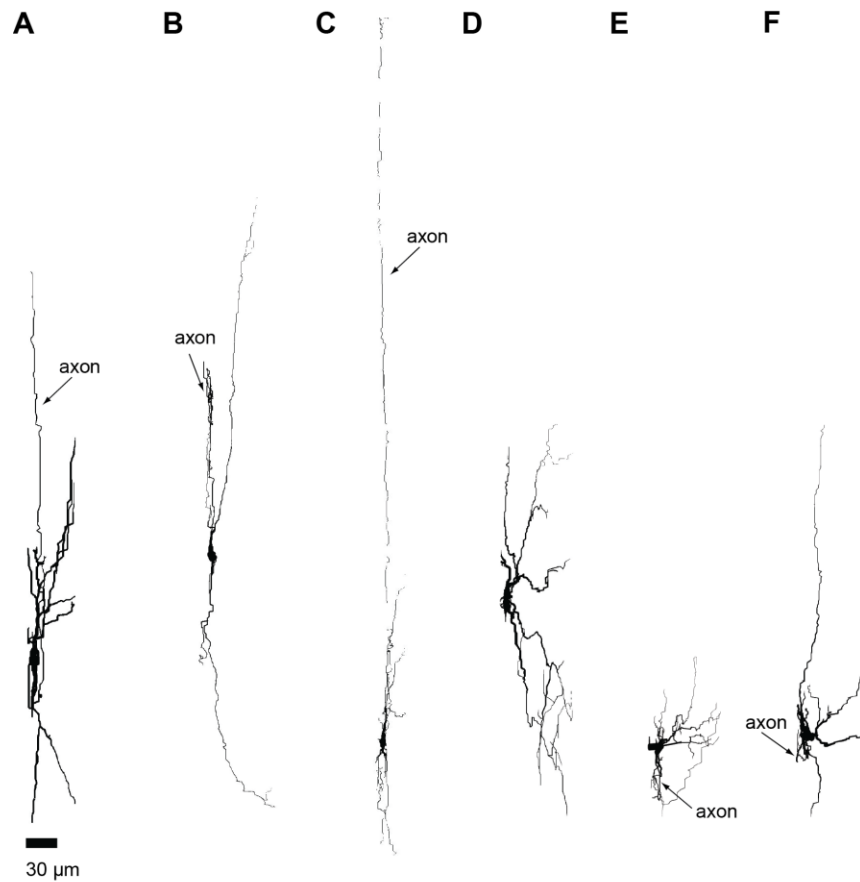


Figure 9. Respiratory Dbx1 preBötC neurons (A-C) have a smaller projection in the rostrocaudal plane than respiratory non-Dbx1 preBötC neurons (D-F) (Picardo et al., 2013).

While some of the morphometric properties of respiratory preBötC Dbx1 neurons have been elucidated, we have yet to determine the morphometric properties of respiratory modulated Dbx1 neurons in other parts of the respiratory microcircuit such as Dbx1 premotor neurons. In this dissertation, I will examine the morphometric properties of respiratory Dbx1 neurons in the reticular formation, a heterogeneous population dorsal to the preBötC that includes

respiratory modulated Dbx1 premotor neurons. Since reticular Dbx1 neurons are largely premotor rather than rhythmogenic, we expect Dbx1 reticular neurons and Dbx1 preBötC neurons will differ in some dendritic morphological features such as diameter. Also, given their premotor propensity, we suspect Dbx1 reticular neurons will project to the hypoglossal motor nucleus to facilitate respiratory related motor output.

Sighs

Sighs are long, deep breaths that most people would automatically associate with emotional states such as sadness, relief, frustration, or exhaustion. However, physiological sighs occur regularly during normal breathing (eupnea) to prevent collapsed alveoli in the lungs and to help preserve normal lung function (Ramirez, 2014; Reynolds, 1962). The increased inspiratory volume associated with sighs is reflected by a double-burst from the preBötC, the second part of the burst comes immediately at the peak (or slightly after) the eupneic preBötC burst (Lieske, 2000; Ruangkittisakul et al., 2008). Those data (and references) suggest that sighs and eupnea originate from the same neural population in the preBötC. Sighs are distinct from eupnea and gasping as demonstrated in an *in vitro* slice model of breathing when cadmium (Cd^{2+}) eliminated sighs without affecting eupneic bursts (Lieske, 2000; Toporikova et al., 2015). While the neural network that controls sighs has not been fully elucidated,

it is known that bombesin-like neuropeptides can evoke sighing behavior in rodents (Li et al., 2016; Ramirez, 2014).

Neuromedin B (*Nmb*), a gene that encodes a bombesin-like neuropeptide in mammals similar to the bombesin peptide found in frogs that influences sighing (Niewoehner et al., 1983), is expressed in the neurons of the rostral medulla around the RTN and pFRG in mice (Li et al., 2016). Neurons expressing *Nmb* project to the preBötC with some evidence that there may be contacts with somatostatin-positive neurons in the preBötC, but the data are ambiguous because the resolution of the neuroanatomy is insufficient to be sure the visualized cells are neurons or some other cell type (Li et al., 2016). Some preBötC neurons express mRNA for the receptor for the peptide NMB (Li et al., 2016), though the role of sigh receptor peptides in the preBötC needs to be further investigated. In anaesthetized rats that exhibited normal breathing patterns with regularly occurring sighs, bilateral injection of the peptide NMB into the preBötC increased the sigh frequency 6-17 times the normal frequency for several minutes (Li et al., 2016). In neonatal mouse slices containing the preBötC that exhibited rhythmic bursts and occasional doublet sigh bursts, NMB increased the frequency of doublets by changing inspiratory bursts to sighs, which indicates NMB influences the preBötC to increase sighing (Li et al., 2016). Bilateral injection of an NMB receptor antagonist reduced sighing but did not noticeably change eupneic respiration in wild type mice. In *Nmbr*^{-/-} knockout mice, sighing frequency was reduced overall compared to wild type mice (Li et al., 2016) suggesting NMBR signaling in the preBötC is important for basal sighing.

Pharmacological inhibition of *Nmbr* and knocking it out of the genome attenuates sighing behavior, but does not eliminate sighing, which indicates that NMB and NMB receptors do not comprise the sole pathway for generating and controlling sighs. Mammals also express the gastrin-releasing peptide (*Grp*) gene, another bombesin-like peptide gene (Jensen et al., 2008). In mice and rats, *Grp* was expressed in some cells in the dorsal part of the RTN and pFRG region as well as the nucleus tractus solitarius and the parabrachial nucleus, which are other regions involved in respiration (Guyenet et al., 2010; Li et al., 2016). Neurons expressing *Grp* project to the preBötC, some of which project onto somatostatin-positive neurons (Li et al., 2016). Bilateral injection of GRP into the preBötC of anaesthetized rats increased sighing 8-16 times the baseline sighing frequency and nearly doubled the amount of doublets in slices containing the preBötC (Li et al., 2016) indicating GRP also influences sighs through the preBötC. In *Grp*^{-/-} mice, sighs were reduced by half though eupnea was unaffected. Bilateral injection of a GRPR antagonist into the preBötC of anaesthetized rats decreased sighing without changing normal respiration (Li et al., 2016). Basal sighing may be maintained by GRPR-expressing neurons in the preBötC, although the presence of GRP receptors on Dbx1 preBötC neurons has not yet been studied. Potentially, NMB or GRP receptors on glia play a role in sigh regulation because glial toxins inhibited sighs while eupneic breathing persisted (Dashevskiy et al., 2016). The current data suggest, but do not demonstrate, that NMR- and GRP-expressing neurons of the rostral medulla

directly innervate preBötC neurons. More investigation is needed to determine whether NMBRs and GRPRs are expressed in preBötC neurons or glia.

This dissertation will investigate morphological and anatomical properties of neurons that generate inspiratory behavior and influence respiratory motor pattern in mice. Morphological differences between Dbx1 preBötC rhythm generating neurons and Dbx1 premotor reticular formation neurons will also be addressed. The presence of Trpc3 ion channels, a candidate for facilitating I_{CAN} , and $NA_v1.6$ ion channels, a candidate for I_{NaP} , will be assessed for Dbx1 preBötC neurons. Finally, this dissertation will address whether bombesin-like receptors, which are involved in sigh behavior, are present on preBötC neurons and glia.

CHAPTER 1: Morphology of Dbx1 Respiratory Neurons in the preBötzing Complex and Reticular Formation of Neonatal Mice

INTRODUCTION

Neuronal morphology, particularly the structure of the dendritic tree, influences how a neuron integrates synaptic inputs and generates physiological output patterns. Axon projections provide information about connectivity patterns in microcircuits. This study documents the morphology of brainstem interneurons that generate and control breathing.

Breathing is a rhythmic motor behavior that ventilates the lungs to support respiration and homeostasis in air-breathing vertebrates. For humans and all mammals, rodents serve as an advantageous model system to study the breathing's neural origins. Key interneuron populations that generate inspiratory, expiratory, and (very recently) post-inspiratory related rhythms have been characterized in terms of physiology, genetic background, and transmitter phenotype (Feldman and Del Negro, 2006; Feldman et al., 2013; Ramirez et al., 2016; Richter and Smith, 2014). Premotor neurons that influence airway resistance have been similarly characterized (Chamberlin et al., 2007; Gestreau et al., 2005; Koizumi et al., 2008; Ono et al., 1998; Revill et al., 2015; Travers et al., 2005; Volgin et al., 2008). However, only a limited number of morphologies of constituent neurons in these populations have been documented and analyzed (Picardo et al., 2013; Revill et al., 2015; Wang et al., 2014). This chapter, which

corresponds to a published data descriptor: doi:10.1038/sdata.2017.97, aims to ameliorate that problem by providing annotated, high-quality digital reconstructions of the morphologies of rhythm-generating interneurons and motor pattern-related premotor neurons from neonatal mice.

The respiratory cycle is dominated by the rhythm underlying inspiration, which is generated within the preBötzinger complex (preBötC) of the ventral medulla (Feldman and Del Negro, 2006; Feldman et al., 2013; Moore et al., 2013; Ramirez et al., 2016; Richter and Smith, 2014; Smith et al., 1991). Rhythmogenic preBötC neurons are derived from precursor cells that express the homeobox transcription factor *Dbx1* (Bouvier et al., 2010; Gray et al., 2010; Vann et al., 2016; Wang et al., 2014), hereafter referred to as *Dbx1* neurons. The intermediate reticular formation, immediately adjacent (dorsal) to the preBötC, is a diverse region containing respiratory *Dbx1* premotor interneurons that control inspiratory related muscles of the tongue and pharynx (Chamberlin et al., 2007; Peever et al., 2002; Stanek et al., 2014; Welzl and Bureš, 1977).

In this study we used intersectional mouse genetics to induce fluorescent protein expression in *Dbx1* neurons of neonatal mice. Neuronal morphologies were acquired following patch-clamp recordings in transverse brainstem slices that retain the preBötC, the intermediate reticular formation, as well as the hypoglossal (XII) motor nucleus. These slices expose the preBötC and reticular formation at the rostral surface and spontaneously generate inspiratory rhythm and XII motor output, thus providing an experimentally advantageous breathing model *in vitro* (Funk and Greer, 2013; Ruangkittisakul et al., 2014).

We obtained three-dimensional morphologies of respiratory Dbx1 preBötC and Dbx1 intermediate reticular formation neurons by filling neurons with biocytin during whole-cell patch-clamp recordings (Halavi et al., 2012; Jacobs et al., 2010; Parekh and Ascoli, 2013, 2015). Compared to other reconstruction methods such as fluorescence microscopy of dye-filled neurons, biocytin reconstructions can be more time consuming but provide better visualization of thinner neuronal processes and axons (Blackman et al., 2014). Once labeled, we visualized the recorded neurons via confocal imaging and manually reconstructed their morphologies in a convenient digital format suitable for storage, display, and analysis.

Over the past four years, the Del Negro laboratory contributed 47 digital neuronal morphologies to the public open access database NeuroMorpho.org (this author, V.T. Akins, was either the lead morphologist or played a major role in managing the reconstructions for publication. Of those 47 digital reconstructions, 23 correspond to Dbx1 preBötC neurons (Picardo et al., 2013; Wang et al., 2014). Six have not been previously published; this report and the corresponding data descriptor publication (Akins et al., 2017) describes them for the first time. Twelve of the 47 correspond to preBötC neurons not derived from *Dbx1*-expressing precursors (Picardo et al., 2013) (i.e., non-*Dbx1* preBötC neurons), and 12 correspond to Dbx1 reticular formation neurons (Revill et al., 2015).

Digital morphologies can be analyzed by software packages such as L-measure (Scorcioni et al., 2008), which computes more than 40 different

morphometric properties of dendritic trees and axons. Sholl analysis, which provides branching and dendritic density information in regular distance intervals from the soma (Langhammer et al., 2010; Sholl, 1953), can be performed with software such as NeuronStudio (Wearne et al., 2005). Digital morphologies can also be readily ported to simulation packages such as NEURON (Hines and Carnevale, 1997) and GENESIS (Bower et al., 2003) to form compartmental mathematical models that are high-fidelity representations of real neurons. We intend that these morphological data be meta-analyzed and incorporated into models of inspiratory rhythm- and pattern-generating circuits of the lower brainstem to better understand the neural mechanisms of breathing. That is why we published the data descriptor in addition to this dissertation chapter, and have released the data in the public domain on Neuromorpho.org.

METHODS

Mice

All of the animal protocols were approved by the Institutional Animal Care and Use Committee at The College of William and Mary, which follows the guidelines provided by the US National Institutes of Health Office of Laboratory Animal Welfare (NIH Office of Laboratory Animal Welfare, 2015).

Figure 10 recaps the workflow, which is detailed below. We crossed female mice that express Cre recombinase fused to a tamoxifen-sensitive

estrogen receptor (*CreERT²*) under the control of the *Dbx1* promoter, i.e., *Dbx1^{CreERT2}* (stock no. 028131, Jackson labs, Bar Harbor, ME) (Hirata et al., 2009) with floxed male reporter mice that express red fluorescent protein variant tdTomato in a Cre-dependent manner (*Rosa26^{tdTomato}*, stock no. 007905, Jackson labs)(Madisen et al., 2010). Offspring with both alleles (*Dbx1^{CreERT2}*; *Rosa26^{tdTomato}* mice), whose pregnant dams received tamoxifen during embryonic development, express the fluorescent reporter in *Dbx1*-derived cells (Hirata et al., 2009; Picardo et al., 2013; Ruangkittisakul et al., 2014) (Fig. 10, step 1). *Dbx1^{CreERT2}* mice were maintained on a CD-1 background strain. *Rosa26^{tdTomato}* reporter mice were maintained using a C57BL/6J background strain.

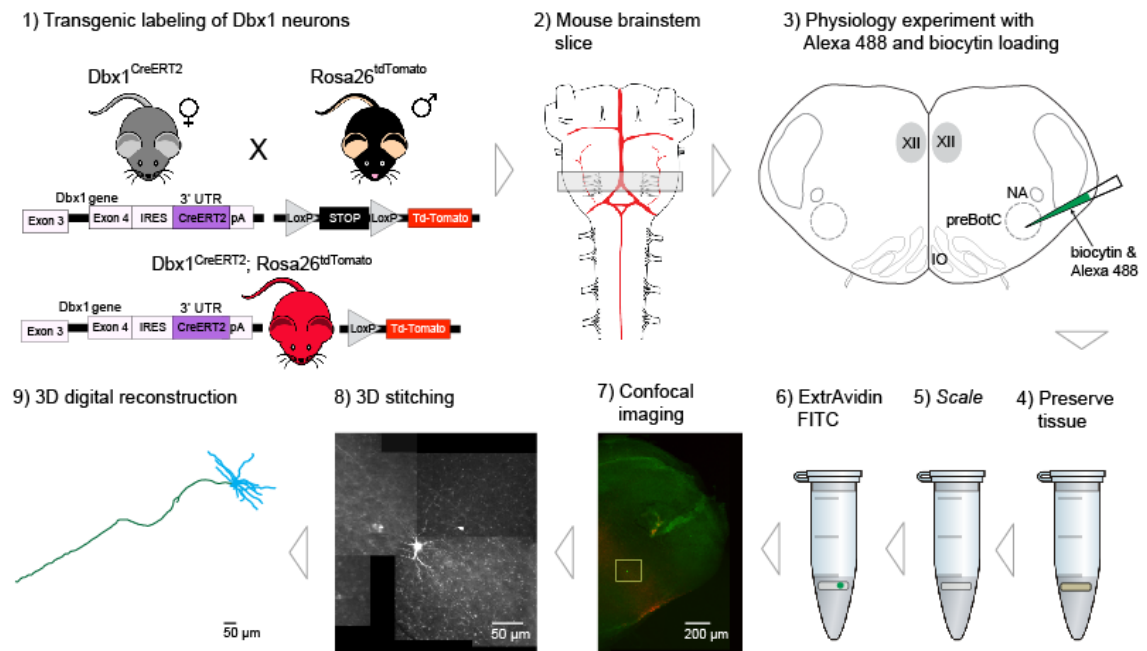


Figure 10. Workflow diagram for digital neuronal reconstructions. Expression of the red fluorescent protein tdTomato is induced in *Dbx1* neurons in mice (1). A transverse slice of the brainstem (indicated by the gray box) containing the preBötzing complex is taken from a neonatal transgenic mouse (2). The slice is used for physiology recordings, during which respiratory modulated neurons are filled with biocytin (3). The slice is then preserved in 4% paraformaldehyde (4) and made transparent via incubation in *Scale* solution (5). The slice is treated with ExtrAvidin FITC (6) which binds to the biocytin allowing for visualization of the neuron through confocal microscopy (7). Confocal images in the x-, y-, and z- dimensions are taken of the entire neuron morphology and stitched together using FIJI (8). Using the 3D confocal images, neurons are digitally reconstructed using Neuromantic (9). XII, hypoglossal nucleus; NA, nucleus ambiguus, preBötC, preBötzing complex; IO, inferior olive. (Akins et al., 2017)

Dbx1^{CreERT2} mice were also mated with floxed reporter mice that express a channelrhodopsin-2/tdTomato fusion protein (*Rosa26*^{ChR2-tdTomato}, stock no. 12567, Jackson labs) (Madisen et al., 2012). The *Dbx1*^{CreERT2}; *Rosa26*^{ChR2-tdTomato} mice were employed in separate electrophysiological experiments; here we recovered the morphology of the recorded neurons in the same way as *Dbx1*^{CreERT2}; *Rosa26*^{tdTomato}, which was possible because both expressed native tdTomato in *Dbx1*-derived neurons. Channelrhodopsin, while important for

physiological tests, has no impact on morphological studies. Figure 10 only indicates *Dbx1^{CreERT2}; Rosa26^{tdTomato}* mice for simplicity.

Animal genotypes were verified using real-time PCR using primers for *Cre* and tandem dimer red fluorescent protein (Transnetyx, Cordova, TN). Timed matings were monitored such that embryonic day 0.5 (E0.5) was defined as 12 hours after the start of cohabitation. *Cre* recombination was then induced by administering tamoxifen (T5648; Sigma Aldrich, St Louis, MO) at E10.5 when *Dbx1* is at or near peak expression in the hindbrain (Bouvier et al., 2010; Gray et al., 2010; Hirata et al., 2009; Pierani et al., 2001). Tamoxifen was administered by oral gavage to pregnant dams at a concentration of 0.9 mg / 40 g body mass.

Transverse slice preparations

Neonatal *Dbx1^{CreERT2}; Rosa26^{tdTomato}* and *Dbx1^{CreERT2}; Rosa26^{ChR2-tdTomato}* mice were anesthetized then euthanized via decapitation at postnatal days 0-5 (P0-5), consistent with protocols outlined by the American Veterinary Medical Association Guidelines for euthanasia of animals (Leary et al., 2013).

Transections were made at the bregma and the thorax. The neuraxis, from the pons to the lower thoracic spinal cord, was then removed within two minutes and further dissected in artificial cerebrospinal fluid (ACSF) containing (mM): 124 NaCl, 3 KCl, 1.5 CaCl₂, 1 MgSO₄, 25 NaHCO₃, 0.5 NaH₂PO₄ and 30 dextrose, equilibrated with 95% O₂ and 5% CO₂ (pH 7.4) (Fig. 10, step 2). The neuraxis was then glued to an agar block with the ventral surface facing out and placed in

the vise of a vibratome. We cut 550- μ m-thick transverse brainstem slices that exposed the preBötC at the rostral face and retained the rostral XII nerve rootlets (Ruangkittisakul et al., 2014) (Fig. 10, step 3). Slices were perfused with ACSF at 28°C in a recording chamber on a fixed-stage upright microscope equipped with differential interference contrast optics and epifluorescence, which enables visual identification and selective recording of target neurons. The K⁺ concentration in the ACSF was elevated to 9 mM to maintain long-term stability of the preBötC rhythm (Funk and Greer, 2013; Ruangkittisakul et al., 2006, 2014). Rhythmic inspiratory-related motor output was recorded from the XII nerve rootlets using suction electrodes and a differential amplifier. Whole-cell patch-clamp recordings were acquired using capillary glass micro-pipettes and a current-clamp amplifier. Patch pipettes were positioned under visual control after fluorescent identification of Dbx1 neurons. The patch solution contained (mM): 140 potassium gluconate, 10 HEPES, 5 NaCl, 1 MgCl₂, 0.1 EGTA, 2 Mg-ATP, 0.3 Na₃-GTP and 2 mg/mL biocytin (B4261; Sigma Aldrich). All of the neurons in this data set were rhythmically active in sync with inspiratory XII motor output.

After the recordings, transverse slices containing biocytin-filled neurons were fixed in 4% paraformaldehyde in 0.1 M sodium phosphate buffer for at least 16 h at 4°C (Fig. 10, step 4). Then, the slices were treated with *Scale* solution containing 4 M urea, 10% (mass/volume) glycerol and 0.1% (m/v) Triton X-100, for 10 days to clear the tissue and remove opaque background staining (Hama et al., 2011) (Fig. 10, step 5). Slices were washed three times for 15 minutes each in phosphate buffer solution (PBS) + 1% Triton X-100 (PBST) and then blocked

in PBST with 10% heat-inactivated fetal bovine sera (F4135; Sigma Aldrich) for 45 minutes. The biocytin was revealed by incubating the slices with fluorescein isothiocyanate-conjugated ExtrAvidin (E2761; Sigma Aldrich) overnight at 4°C with three-dimensional rotation on a nutator (Fig. 10, step 6). Next, the slices were rinsed with PBS five times for 15 minutes each and cover-slipped in Vectashield (H-1500; Vector Laboratories, Burlingame, CA).

Confocal microscopy and digital neuronal reconstruction

We visualized recorded neurons using a spinning-disk confocal microscope (Olympus BX51, Center Valley, PA) and a laser scanning confocal microscope (Zeiss LSM 510, Thornwood, NY). Three-dimensional (3D) confocal images of the individual neurons were obtained using a 20x objective (Olympus numerical aperture 0.5, Zeiss LSM numerical aperture 1.0) at increments of 1 μm in the z-axis (Fig. 10, step 7). The series of confocal images (i.e., z-stacks) were aligned in three-dimensions, merged or 'stitched together' at contiguous borders using ImageJ software (Schneider et al., 2012) and the Stitching plugin (Preibisch et al., 2009) (Fig. 10, step 8). This stitching process was iterated until the entire morphology of the neuron was contained within a single three-dimensional image file. Finally we digitized neuronal morphologies using the Neuromantic reconstruction tool, which is also free and in the public domain (Myatt et al., 2012). The digital reconstructions were scaled to the appropriate size based on the micron-to-pixel ratio for each microscope (Fig. 10, step 9).

Images acquired from the LSM microscope were scaled with a 0.41 micron-to-pixel ratio and images from the Olympus microscope were scaled using a 0.322 micron-to-pixel ratio. This chapter (and its associated data descriptor) pertain to 47 digital morphologies of inspiratory modulated Dbx1 preBötC neurons, six of which are previously unpublished (Data Citations 1-6) and 41 which are associated with previous publications (Data Citations 7-47). The morphologies are all publicly available via NeuroMorpho.org.

DATA RECORDS

Digital reconstructions of Dbx1 neurons are located in the Del Negro archive of the NeuroMorpho database (Data Citations 1-47). Digital reconstruction files are in SWC format, which is a commonly used format for neuron morphologies (Jacobs et al., 2010). The reconstruction files contain an x-coordinate, y-coordinate, and z-coordinate of each neuronal segment. The type of neuronal process, such as cell body, axon, or dendrite is also specified by type 1, 2, and 4, respectively. (Type 3 represents basal dendrites, but there is no such distinction in brainstem interneurons, so type 3 is omitted as a classifier in our dataset. Our dendrites were all designated type 4.) The radius in microns is given for each neuronal segment as well as the “parent” segment or the index number of the previous segment. Table 1 provides an example of an SWC file output for a neuron reconstruction. Physiological properties of Dbx1 preBötC and Dbx1

reticular neurons have been described (Picardo et al., 2013; Revill et al., 2015; Wang et al., 2014).

Index	Type	x	y	z	Radius	Parent
1	1	967.7	1539.0	9	13.81	-1
2	4	970.0	1533.0	10	7.35	1
3	4	971.3	1530.5	10	4.59	2
4	4	972.0	1528.5	11	3.58	3
5	4	972.1	1525.2	11	3.27	4
6	4	971.9	1522.6	11	2.57	5
7	4	971.6	1520.1	11	2.17	6
8	4	971.1	1517.3	10	1.77	7
9	4	971.0	1514.7	9	1.68	8
10	4	970.4	1513.3	9	1.61	9
11	4	969.2	1510.2	9	1.50	10
12	4	968.5	1509.6	9	1.50	11
13	4	967.5	1509.4	9	1.50	12
14	4	966.9	1507.9	8.5	1.50	13
15	4	966.5	1506.2	8	1.50	14
16	4	966.3	1504.9	8	1.50	15
17	4	965.9	1503.5	8	1.49	16

Table 1. Sample SWC file data for digital neuron reconstruction. This table contains the first 17 rows of an SWC file generated for a digital reconstruction. For each reconstruction segment there is an index number, segment type (soma (1), axon (2), dendrite (4)), x-, y-, and z-coordinates, radius (in microns), and parent segment.

TECHNICAL VALIDATION

In newborn *Dbx1^{CreERT2}; Rosa26^{GtdTomato}* and *Dbx1^{CreERT2}; Rosa26^{ChR2}*

tdTomato mice, *Dbx1* neurons form an inverted U-shape in the transverse (coronal) plane, which is visible in brainstem slices at the level of the preBötC. The inverted U-shape originates at the lateral border of the hypoglossal motor nucleus, located within the dorso-medial portion of the slice, and continues

ventrolaterally until the ventral border of the tissue slice (Ruangkittisakul et al., 2014). The dorsal border of the preBötC is identifiable because it is immediately ventral to the semi-compact division of the nucleus ambiguus, which does not express Dbx1 (Ruangkittisakul et al., 2014). Visual identification of the principal loop of the inferior olive and the flattening of the V-shape of the fourth ventricle are other indicators that the rostral surface of the transverse slice is at the level of the preBötC (Ruangkittisakul et al., 2014).

Slices remained in the recording chamber for at least 15 minutes after biocytin dialysis to maximize biocytin diffusion throughout the cytoplasm (Jacobs et al., 2010; Picardo et al., 2013). A clearing agent was used to facilitate visualization of the morphology; however clearing reagents can cause tissue shrinkage or expansion which could distort morphological features (Hama et al., 2011). The *Scale* solution used to clear the tissue in these experiments minimizes or completely precludes tissue expansion (compared to other methods) (Hama et al., 2011).

The quality of digital reconstructions depends on histology methods, image acquisition, as well as the digital reconstruction algorithms. To minimize disparities, we consistently used the same method of histological labeling. The software Neuromantic (Myatt et al., 2012), used for digitizing our image stacks, offers up to 16,000% magnification. This zoom feature enables the user to adhere to the most minute details captured in the image, which results in the most accurate reconstruction possible.

Two of the six new neurons and nine of the previously published neurons had no discernible axon, which might have indicated insufficient biocytin filling or that the axon was severed during tissue preparation. We recommend that the end user of the data draw no firm conclusions regarding connectivity from the lack of an axon in reconstructed digital morphology.

For those neurons whose axons were discernible, we distinguished the axons from the dendrites according to these criteria: 1) axons generally have a constant diameter whereas dendrites taper distal to the soma. 2) Axons exhibit fewer branches and never show spine-like protrusions. 3) Truncated axons near the slice surface exhibit a bleb or fluorescent circle from the cut end (Furness et al., 2003; Swietek et al., 2016).

Digital reconstructions were uploaded to NeuroMorpho.org, where they undergo a standardization process. The soma (type 1) should be the initial parent segment for all subsequent segments, whether dendritic or axonal. Neuronal processes should only connect to either the soma or to segments of the same type; for example, dendrite segments connect to dendrite segments and axon segments connect to axon segments. All processes should have a designated type and should not be undefined. A process can branch into no more than two processes at any given point.

Some irregularities can be fixed automatically during the standardization process (Halavi et al., 2008). If a neuronal segment is designated as a different type than its parent and daughter segments (e.g., a type 3 surrounded by type 2s) the erroneous segment type is automatically changed to match the type of its

parent and daughter segments. If the soma is not the initial segment in the file, the soma segment is automatically changed to the first segment in the file. If a segment has a radius of zero microns, then the radius is automatically changed to match the radius of its parent. Other digitization issues must be corrected by the submitting investigator (Halavi et al., 2008). For example, if a segment has not been designated with a process type, the correct type must be manually entered, rather than automatically assigned, which ensures that the proper type has been documented. Segments with a radius of zero (i.e., less than 0.05 μm), or larger than four standard deviations above the average radius of the cell are flagged as physiologically unrealistic during standardization and must be resolved by the submitting investigator. After the standardization process, digital reconstruction files and images are then reviewed and approved by the submitting investigator before being added to the public database (Halavi et al., 2008).

DATA CITATIONS

Del Negro, C. A. NeuroMorpho.org NMO_45917 (2017)

Del Negro, C. A. NeuroMorpho.org NMO_45918 (2017)

Del Negro, C. A. NeuroMorpho.org NMO_45921 (2017)

Del Negro, C. A. NeuroMorpho.org NMO_45922 (2017)

Del Negro, C. A. NeuroMorpho.org NMO_45923 (2017)

Del Negro, C. A. NeuroMorpho.org NMO_45924 (2017)

- Del Negro, C. A. NeuroMorpho.org NMO_09581 (2013)
- Del Negro, C. A. NeuroMorpho.org NMO_09582 (2013)
- Del Negro, C. A. NeuroMorpho.org NMO_09583 (2013)
- Del Negro, C. A. NeuroMorpho.org NMO_09584 (2013)
- Del Negro, C. A. NeuroMorpho.org NMO_09585 (2013)
- Del Negro, C. A. NeuroMorpho.org NMO_09586 (2013)
- Del Negro, C. A. NeuroMorpho.org NMO_09587 (2013)
- Del Negro, C. A. NeuroMorpho.org NMO_09588 (2013)
15. Del Negro, C. A. NeuroMorpho.org NMO_09589 (2013)
16. Del Negro, C. A. NeuroMorpho.org NMO_09590 (2013)
17. Del Negro, C. A. NeuroMorpho.org NMO_09591 (2013)
18. Del Negro, C. A. NeuroMorpho.org NMO_09592 (2013)
19. Del Negro, C. A. NeuroMorpho.org NMO_09592 (2013)
20. Del Negro, C. A. NeuroMorpho.org NMO_09594 (2013)
21. Del Negro, C. A. NeuroMorpho.org NMO_09595 (2013)
22. Del Negro, C. A. NeuroMorpho.org NMO_09596 (2013)
23. Del Negro, C. A. NeuroMorpho.org NMO_09597 (2013)
24. Del Negro, C. A. NeuroMorpho.org NMO_09598 (2013)
25. Del Negro, C. A. NeuroMorpho.org NMO_09599 (2013)
26. Del Negro, C. A. NeuroMorpho.org NMO_09600 (2013)
27. Del Negro, C. A. NeuroMorpho.org NMO_09601 (2013)
28. Del Negro, C. A. NeuroMorpho.org NMO_09602 (2013)
29. Del Negro, C. A. NeuroMorpho.org NMO_09603 (2013)

30. Del Negro, C. A. NeuroMorpho.org NMO_09604 (2013)
31. Del Negro, C. A. NeuroMorpho.org NMO_09605 (2013)
32. Del Negro, C. A. NeuroMorpho.org NMO_09606 (2013)
33. Del Negro, C. A. NeuroMorpho.org NMO_45919 (2016)
34. Del Negro, C. A. NeuroMorpho.org NMO_45920 (2016)
35. Del Negro, C. A. NeuroMorpho.org NMO_45925 (2016)
36. Del Negro, C. A. NeuroMorpho.org NMO_45926 (2016)
37. Del Negro, C. A. NeuroMorpho.org NMO_45927 (2016)
38. Del Negro, C. A. NeuroMorpho.org NMO_45928 (2016)
39. Del Negro, C. A. NeuroMorpho.org NMO_45929 (2016)
40. Del Negro, C. A. NeuroMorpho.org NMO_45930 (2016)
41. Del Negro, C. A. NeuroMorpho.org NMO_45931 (2016)
42. Del Negro, C. A. NeuroMorpho.org NMO_45932 (2016)
43. Del Negro, C. A. NeuroMorpho.org NMO_45933 (2016)
44. Del Negro, C. A. NeuroMorpho.org NMO_45934 (2016)
45. Del Negro, C. A. NeuroMorpho.org NMO_45935 (2016)
46. Del Negro, C. A. NeuroMorpho.org NMO_45936 (2016)
47. Del Negro, C. A. NeuroMorpho.org NMO_45937 (2016)

CHAPTER 2. Analysis of dendritic arbor and axon projections of Dbx1 preBötC and reticular formation neurons

INTRODUCTION

Information about neural network structure as well as insights into the roles of neuron subpopulations can be obtained through morphological analysis of key neurons within the circuit (Parekh and Ascoli, 2014). Here, we seek to understand the neural mechanisms underlying breathing behavior via morphological analyses.

Breathing is a rhythmic behavior essential to humans and all mammalian life, yet the neural circuit(s) responsible for this vital behavior are incompletely understood. The putative populations of neurons that generate the respiratory rhythm are known, but the cellular and network properties that make this population unique are still being elucidated. In addition to their biophysical properties, the morphometric properties of respiratory neurons must be examined in order to obtain a more comprehensive picture of their role in the neural network. The specific objective of this study is to examine dendritic morphometric properties and axon trajectories of key respiratory neurons in order to better understand the neural origins of the rhythm underlying inspiratory breathing movements in mammals.

Inspiratory rhythm is generated within the preBötzinger complex (preBötC), a bilaterally distributed site in the ventral medulla (Feldman et al.,

2013; Smith et al., 1991). Putatively rhythmogenic neurons in the preBötC are derived from a single genetic line, whose precursors express homeodomain transcription factor *Dbx1*, hereafter *Dbx1* neurons (Bouvier et al., 2010; Gray et al., 2010). *Dbx1* neurons are involved in important motor behaviors such as left-right alternation of limb movements during locomotion at any speed (Lanuza et al., 2004; Talpalar et al., 2013). Respiratory *Dbx1* preBötC neurons project to various neuron populations including the intermediate reticular formation. The reticular formation contains neurons that drive whisking and sniffing rhythms, which must be coordinated with the breathing rhythm generated by the preBötC. (Gestreau et al., 2005; Kleinfeld et al., 2014; Moore et al., 2013, 2014).

Inspiratory breathing movements in terrestrial mammals must be coordinated with orofacial behaviors that include phonation, chewing, suckling, whisking, licking, and sniffing. While we know the preBötC generates the breathing rhythm and coordinates breathing with other orofacial behaviors (Kleinfeld et al., 2014; Moore et al., 2013, 2014), the cellular and morphological properties, as well as axon projection patterns, of respiratory rhythm and pattern-generating interneurons that may coordinate breathing with orofacial behaviors remain incompletely understood.

Respiratory modulated neurons, some of which express *Dbx1*, have been recognized in the region of the dorsal medulla near the preBötC. Respiratory modulated *Dbx1* neurons may serve as premotor neurons for the airway and tongue that help maintain airway patency during respiration and may also coordinate respiration with other orofacial behaviors (Kleinfeld et al., 2014;

Koizumi et al., 2008; Moore et al., 2013, 2014). This chapter aims to characterize the morphologies of Dbx1 preBötC and reticular formation neurons to gain insight into mechanisms of respiratory premotor function or coordination of breathing with orofacial behaviors; we suspect respiratory Dbx1 reticular formation neurons will be premotor neurons that send signals to the hypoglossal motor nucleus (XII).

METHODS

Methods involving mouse genetics, dissection, labeling neurons via biocytin, tissue fixation, confocal microscopy, and digitization were covered in the previous chapter (See Figure 10). This chapter describes the analyses of the dendritic arbor that I performed on the digitized morphologies introduced in chapter 1. The 3D reconstructions functioned as digital objects that we analyzed further using L-Measure ([L-measure Link](#)) (Scorcioni et al., 2008) and NeuronStudio ([NeuronStudio Link](#)) (Wearne et al., 2005), which are additional tools that are freely available in the public domain. Eighty-five transverse slices containing biocytin-filled neurons were processed, resulting in a total of 23 digitized morphologies of Dbx1 preBötC neurons and 12 digitized morphologies of Dbx1 reticular formation neurons. As described in the literature review, our framework for analysis is that inspiratory-modulated Dbx1 preBötC interneurons are core rhythm-generators for respiration, whereas inspiratory-modulated Dbx1 neurons of the reticular formation may be premotor neurons for inspiratory

tongue movements (because motoneurons for the genioglossus muscle reside in the hypoglossal nucleus). We compared the morphometric properties of Dbx1 preBötC neurons (n=23) and inspiratory modulated Dbx1 reticular formation neurons (n=12) according to 40 different measurements computed by L-measure. The 40 measurements are defined in Table 2.

We also performed a Sholl analysis for each dendritic tree, which measures dendritic length, surface area, volume, and branching at concentric segments beginning at the soma, increasing in diameter throughout the dendritic tree and is used to provide a sense of dendritic complexity (Langhammer et al., 2010; Sholl, 1953). Sholl analysis was performed using NeuronStudio at 25 μm increments for reconstructed neurons in the preBötC and the reticular formation.

Statistical analysis of data was performed using the free and publicly available statistical software PAST, version 3.06, designed for analysis of scientific data in life sciences, earth science, engineering, and economics (Hammer et al., 2001). PAST, a creative acronym for *paleontological statistics*, originally developed to facilitate the use of quantitative methods in paleontology, is now a comprehensive software package offering, univariate statistics, multivariate statistics, curve fitting of data, time series analysis, and data plotting among other features. The Shapiro-Wilk test, the Anderson-Darling test, normal probability plots, and an analysis of the residuals were performed to determine whether the morphometric properties of Dbx1 preBötC neurons and Dbx1 reticular formation neurons were normally distributed. The Shapiro-Wilk test determines a statistic, W , which quantifies the extent to which sample data

depart from normality by generating a normal probability plot and testing the correlation between the predicted normal data and the actual data. W values close to 0 suggest a small departure from normality and as W approaches a value of 1, the departure from normality increases. (Liang et al., 2009; Shapiro and Wilk, 1965). The Anderson-Darling test determines the goodness of fit for the sample data to a normal distribution.

Based on the Shapiro-Wilk test results and the Anderson-Darling test results, some of the morphometric data have a normal distribution but not all. In order to be consistent in the comparison of these data, the same test should be used for each comparison. Parametric tests could not be used for each metric since not all of the metrics were normally distributed. Therefore, a nonparametric test was most appropriate for further data evaluation.

The Mann-Whitney U test is a non-parametric test to evaluate whether two independent samples are likely to be drawn from the same underlying population. Assumptions for the Mann-Whitney U test are that the data are randomly distributed, values are continuous, and values are ordinal meaning that they can be ranked higher or lower than one another. The collected data are in compliance with the assumptions of the Mann-Whitney test and thus was used to compare the morphometric data for respiratory Dbx1 preBötC neurons and respiratory Dbx1 reticular formation neurons.

When comparing two independent samples, the null hypothesis for the Mann-Whitney U test is that a randomly chosen value from one group is equal to the value of the second group; thus, an alternative hypothesis would state that a

sample from the first group has a higher probability of having a larger value than a randomly chosen sample from the second group. The Mann-Whitney test is performed in the following manner for two independent samples. A value is randomly chosen from the first group, then a random value is chosen from the second group, and the larger of the two values is determined. This method is repeated for all of the values in both groups. The total number of times a value in each group was the largest is calculated. The smaller of these two totals is the test statistic U . The maximum number of comparisons made to compute the U statistic is the product of the number of values in group A and group B. The 23 reconstructed preBötC neurons and 12 reconstructed reticular formation neurons result in 276 comparisons between the two groups for each data category. The null hypothesis for the Mann Whitney test is that the distributions of both populations are equal, suggesting that the two groups are drawn from the same underlying population.

RESULTS

Axon projections

We expect Dbx1 neurons in the preBötC to be commissural (i.e., to project axons across the midline) to synapse with their counterparts in the contralateral half of the preBötC and thus synchronize the bilaterally distributed neuron population (Bouvier et al., 2010). Ten of the twenty-six Dbx1 preBötC neurons

that we patch-recorded to verify their inspiratory burst-generating functionality showed axons that projected toward the midline, four of which definitively cross the midline. Six of the midline-projecting Dbx1 preBötC neurons have their morphologies published in a previous master's thesis (Weragalaarachchi, 2012). The author of this work assisted with data collection and collaborative analyses pertaining to that work. Five of the preBötC neurons had axons with ipsilateral projections, all of which are shown in Figures 25-29.

We expect Dbx1 respiratory modulated premotor neurons in the reticular formation to project axons to the hypoglossal motor nucleus. Three of the Dbx1 reticular formation neurons had ipsilateral projecting neurons that approach the hypoglossal motor nucleus, which is consistent with the expected axon projection. However, seven axons in respiratory Dbx1 reticular formation neurons projected across the midline, which was a surprise. In the entire data set of 35 Dbx1 neurons, eleven had short axons or no discernible axon perhaps due to severance during the slice-cutting procedure or due to a fault in biocytin filling.

Dendritic analysis of Dbx1 neurons with no discernible axon in PreBötC

Respiratory Dbx1 preBötC neurons with no discernible axon from the newly reconstructed data set are shown in Figures 30-32. The neurons without discernible axons were viable for dendritic analysis since their morphometric data were not outliers among the entire Dbx1 preBötC population. In fact, some dendrites of neurons without discernible axons had a larger number of stems,

bifurcations and branches that their neighbors with axons as with neuron 130212, whose data are in Table 3 and whose morphology is shown in Figure 30. This particular neuron also has similar height and greater depth (Table 3) than its neighbor from the same slice preparation in which it was recorded and biocytin-filled. Therefore, the morphological data from this neuron was included and analyzed with Dbx1 preBötC neurons that showed discernible axon projections.

Figure 31 showing neuron 120621 had the lowest number of stems (Table 3), which are dendritic protrusions originating at the soma; however, the dendritic height and depth (Table 3) are comparable to the dendritic height and depth (Table 3) of neuron 140117, shown in Figure 23. Figure 32 showing neuron 120623 has the same number of stems as 4 other neurons from the new reconstructions as well as one of the largest values in depth (Table 3). While the neuron shown in Figure 32 has the smallest width (Table 3) of the analyzed neurons, it does not have the smallest height (Table 3). The smallest height belongs to the neuron in Figure 28, whose reconstruction exhibits an axon. While the neurons in Figures 30-32 do not have fluorescently labeled axons, their dendritic morphologies do not appear to be outliers and will be pooled with the rest of the data from the preBötC in the morphometric analysis between respiratory Dbx1 neurons in the preBötC and the reticular formation.

Somatic and dendritic morphometric analysis

Of the forty morphometric measurements, defined in Table 2, used to compare respiratory Dbx1 neurons in the reticular formation and the preBötC, 23 are significantly different based on Mann-Whitney analysis (Table 5). The morphometric properties are categorized by their type: area and volume, branching, path, proportion, angle, and terminal (defined below). Area and volume measurements relate to the surface area and volume of the soma and dendritic compartments. Branching measurements involve the subdivisions or bifurcations of the dendritic tree. Path measurements encompass the span of the individual neurites in all three dimensions. Proportional metrics are ratios between path metrics and branching measurements. Angle measurements pertain to the space between branches within the dendritic tree. Terminal measurements involve the region of the dendritic tree after the last bifurcation.

Area and volume measurements

Neuronal soma sizes have been analyzed in the nervous system to monitor proper development, define certain cell types, and may suggest a relationship between morphology and physiology in some neuronal classes (Oyster et al., 1981). Respiratory Dbx1 neurons in the preBötC and reticular formation have different tasks – Dbx1 preBötC neurons are putative rhythm generators while *Dbx1* reticular formation neurons are thought to be premotor

neurons sending signals to motor nuclei. As they have different roles, we might expect their soma sizes to differ. We found that respiratory preBötC neurons have a smaller average soma surface area compared to respiratory reticular formation neurons (Table 5). Mann-Whitney analysis revealed the difference was statistically significant.

Dendritic diameter will affect the length constant, which is a measure of how the electric potential propagates through the neurite passively, and is the basis for analyzing active dendritic properties (Stuart and Spruston, 2015). A larger length constant will mean that the electrical potential will propagate farther with less attenuation of the input signal, and can thus contribute to synaptic integration more effectively. Respiratory Dbx1 preBötC neurons have a significantly smaller diameter than respiratory reticular formation neurons (Table 5). Dendritic surface area and volume are directly related to the dendritic diameter. There was a statistically significant difference in volume, but not surface area (Table 5).

Branching

Respiratory Dbx1 reticular formation and preBötC neurons do not differ significantly in the number of protrusions from the soma, or stems, nor do they differ significantly in branch order, which is a measure progressive branching within the dendritic tree. The soma, which has no branch points, has a branch

order of 0, the first branch point has an order of 1, the next branch point has an order of two, and this process continues until the final branch point.

A significant difference was computed for respiratory Dbx1 reticular formation compared to Dbx1 preBötC neurons in the number of dendritic bifurcations, which are the branch points, and total number of branches (Table 5). Respiratory Dbx1 reticular formation neurons have significantly fewer bifurcations and branches than respiratory Dbx1 preBötC neurons. Branching patterns will be further analyzed via Sholl Analysis in the subsequent section of the results.

Path Measurements

Respiratory Dbx1 preBötC and reticular formation neurons differ significantly in height, which is the span of the dendrites in the vertical direction, width, which is the span of the dendrites in the horizontal plane, and depth, which is the span of the dendrites perpendicular to the horizontal and vertical planes. Respiratory Dbx1 reticular formation neurons have a smaller average height, width, and depth compared to respiratory Dbx1 preBötC neurons (Table 5).

Respiratory preBötC Dbx1 neurons have a significantly greater total dendritic length than respiratory Dbx1 reticular formation neurons (Table 5), yet they have less dendritic volume (Table 5). The lower average volume in respiratory Dbx1 preBötC neurons is directly related to the smaller diameter of preBötC neurons compared to respiratory Dbx1 reticular formation neurons.

Volume is calculated via the equation $\pi r^2 h$, where r is the radius of the dendrite and h is the height of the dendrite.

Respiratory Dbx1 reticular formation neurons are significantly smaller in average and maximum path distance as well as average and maximum Euclidean distance (Table 5).

Proportional measurements

Respiratory Dbx1 reticular formation neurons are significantly larger in Burke taper and maximum Hillman taper (Table 5), though similar in average Hillman taper (Table 5). Though respiratory Dbx1 preBötC and respiratory Dbx1 reticular formation neurons differ based on the Mann Whitney results for the contraction ratio, their averages and standard error are the same (Table 5). The average and standard error for the fractal diameter is also identical between respiratory Dbx1 preBötC and reticular formation neurons, yet their data differ significantly based on the Mann-Whitney analysis (Table 5). Respiratory Dbx1 preBötC and respiratory Dbx1 reticular formation neurons are similar in daughter ratio, parent-daughter ratio, partition asymmetry, and Rall power.

Angle measurements

Six metrics provide information about the relationships between bifurcation nodes, which are bifurcation points or terminating points, and bifurcation planes,

which is defined by the two daughter compartments. The first two bifurcation metrics are concerned with the bifurcation amplitude. Local amplitude determines the angle between the first two compartments after the bifurcation point. Remote amplitude is the angle between two consecutive bifurcation nodes or between two terminal points. Bifurcation tilt measures the angle between parent or “father” nodes and child or “daughter” compartments to make an outer angle between the father and daughter compartments. Local bifurcation tilt is determined by the angle between the father compartment of the current bifurcation point and the two daughter compartments of the current bifurcation. Remote bifurcation tilt is the angle between the previous father node of the current bifurcation and the two daughter nodes. Bifurcation torque is a measure of the inner angle between the current bifurcation and the parent bifurcation. Local bifurcation torque is the angle between the bifurcation plane, of the previous bifurcation node and the current bifurcation plane. Remote bifurcation torque defines the angle between the current bifurcation plane and the previous bifurcation plane. Respiratory Dbx1 preBötC and respiratory Dbx1 reticular formation neurons are similar in all of these measurements

Terminal measurements

Last parent diameter and diameter threshold both differ significantly between respiratory Dbx1 preBötC and respiratory Dbx1 reticular formation neurons with the reticular formation neurons having the largest in both cases

(Table 5). The Hillman threshold is significantly larger in reticular formation neurons (Table 5). While the Mann-Whitney analysis indicates differences in fractal diameter among respiratory Dbx1 preBötC neurons and respiratory Dbx1 reticular formation neurons, their average values and standard error are equivalent (Table 5). Respiratory Dbx1 reticular neurons have a significantly smaller number of terminal tips and terminal segments than respiratory Dbx1 preBötC neurons (Table 5). The smaller number of terminal segments, which are the compartments of the reconstructed neuron between a bifurcation and a terminal tip, suggests that the respiratory Dbx1 reticular formation neurons have more branch points further out in the more distal parts of the dendritic tree than preBötC neurons.

Reticular Formation – Midline Axon Projections

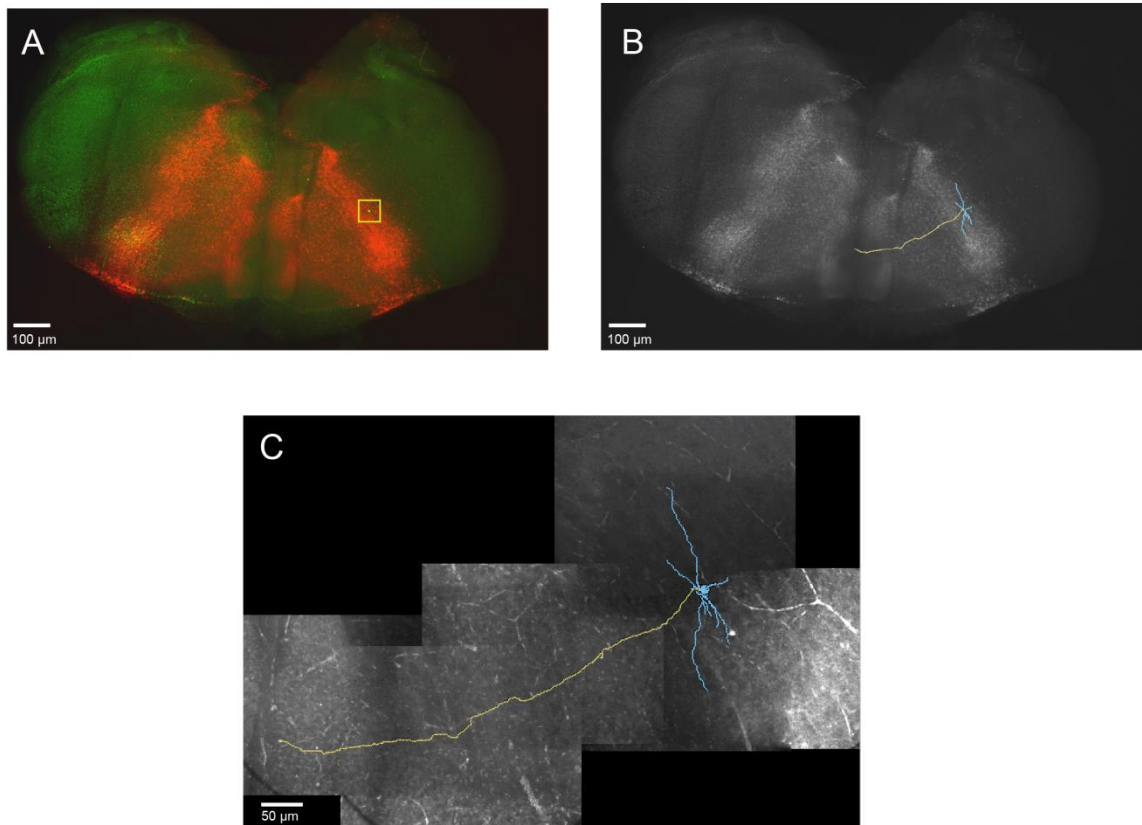


Figure 11. *Dbx1* inspiratory cell 130624 in the reticular formation A, slice mosaic showing *Dbx1* expression via tdTomato transgenic labeling. Location of the cell body is highlighted with a yellow box; B, reconstructed cell morphology on the slice mosaic shows the axon crosses the midline; C, enlarged view of cell morphology showing dendritic tree.

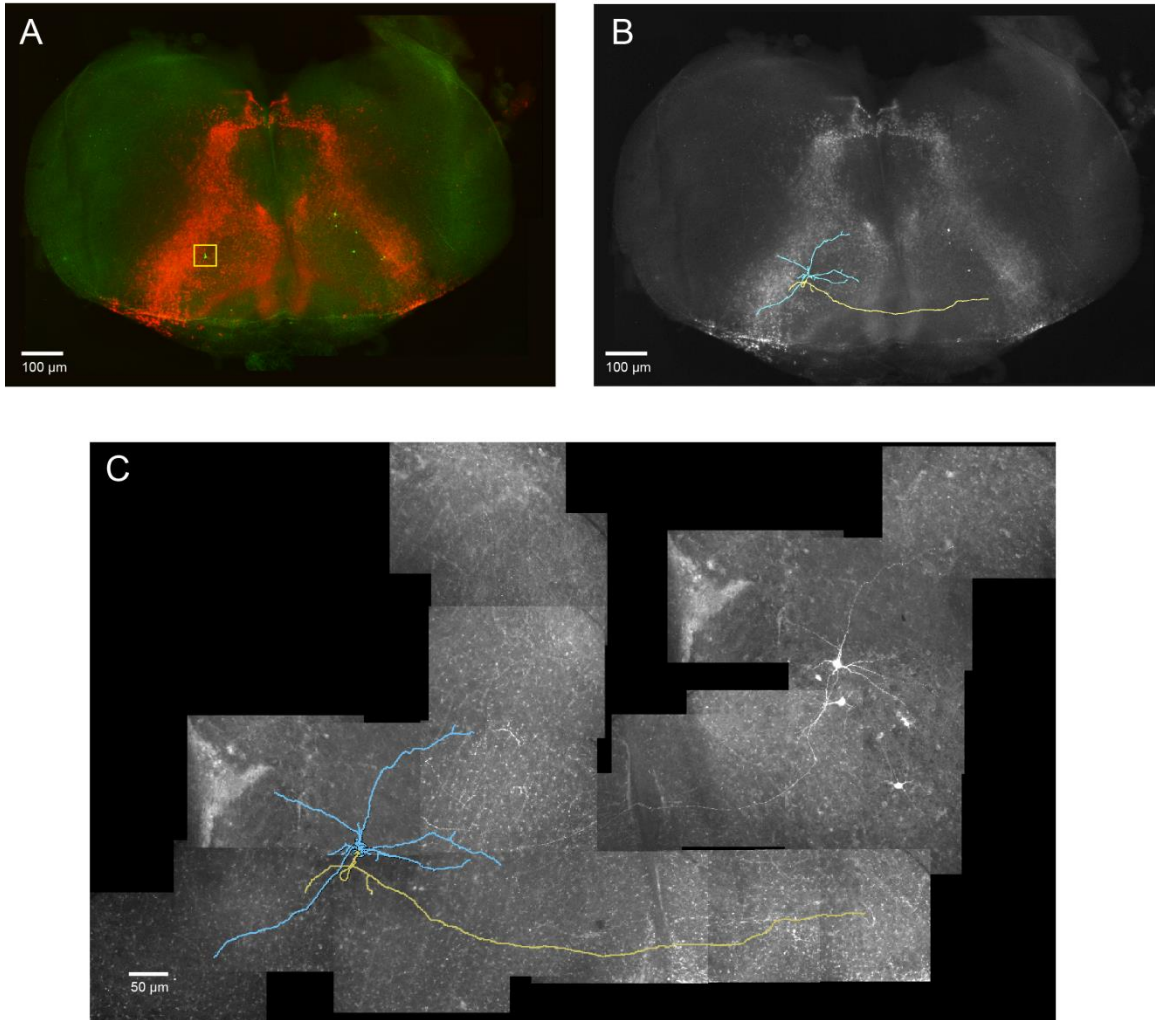


Figure 12. *Dbx1* inspiratory cell 140114 in the reticular formation. A, slice mosaic showing *Dbx1* expression via tdTomato transgenic labeling. Location of the cell body is highlighted with a yellow box; B, reconstructed cell morphology on the slice mosaic shows the axon crosses the midline; C, enlarged view of cell morphology showing dendritic tree

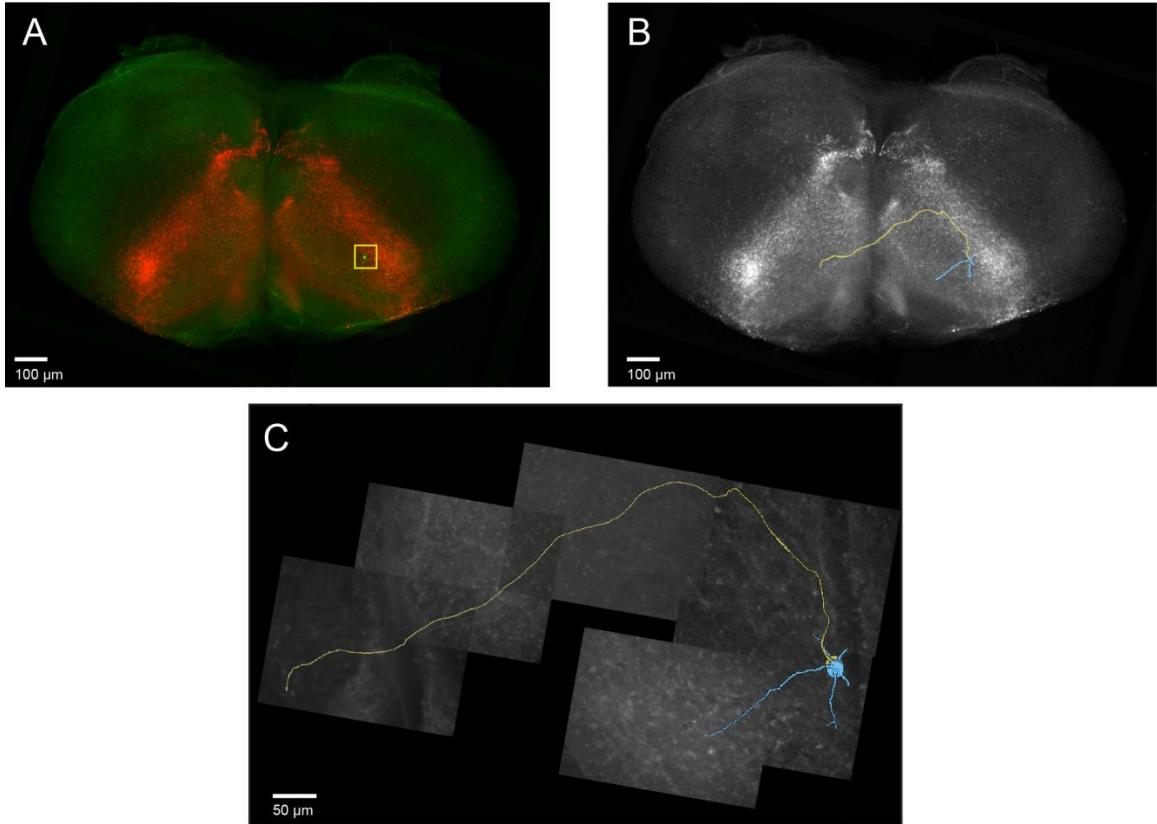


Figure 13. Dbx1 inspiratory cell 140120 in the reticular formation. A, slice mosaic showing Dbx1 expression via tdTomato transgenic labeling. Location of the cell body is highlighted with a yellow box; B, reconstructed cell morphology on the slice mosaic shows the axon crosses the midline; C, enlarged view of cell morphology showing dendritic tree

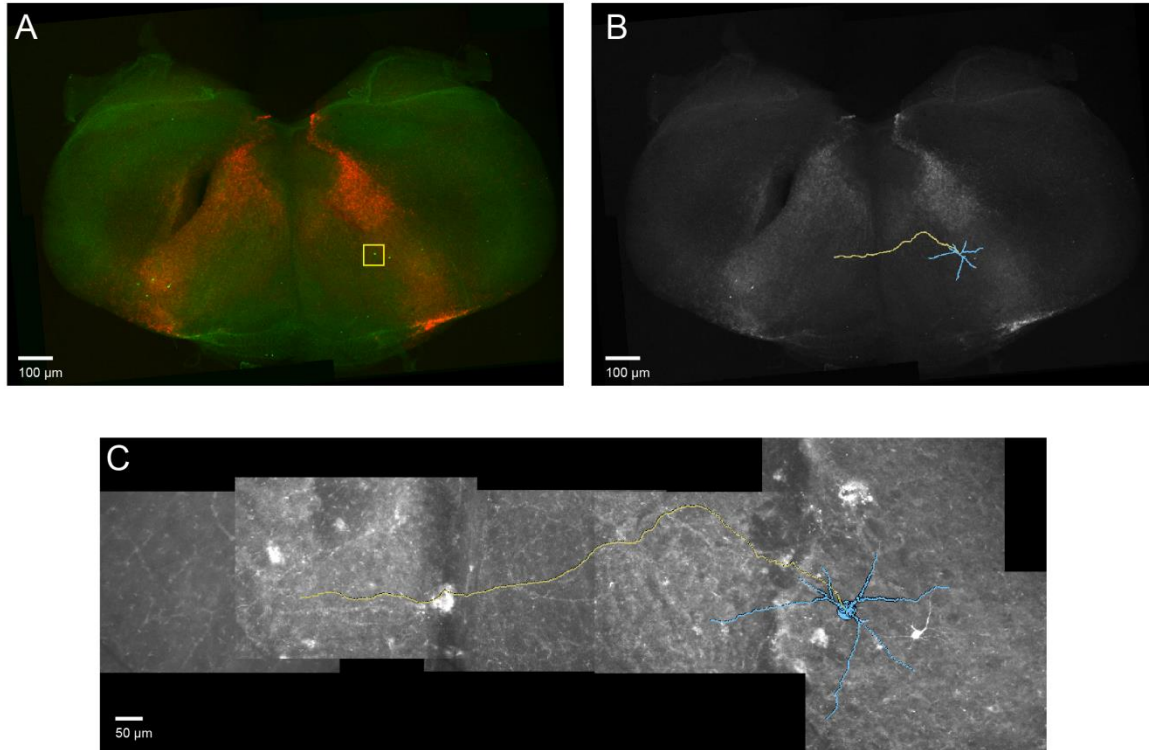


Figure 14. Dbx1 inspiratory cell 140124 in the reticular formation. A, slice mosaic showing Dbx1 expression via tdTomato transgenic labeling. Location of the cell body is highlighted with a yellow box; B, reconstructed cell morphology on the slice mosaic shows the axon crosses the midline; C, enlarged view of cell morphology showing dendritic tree

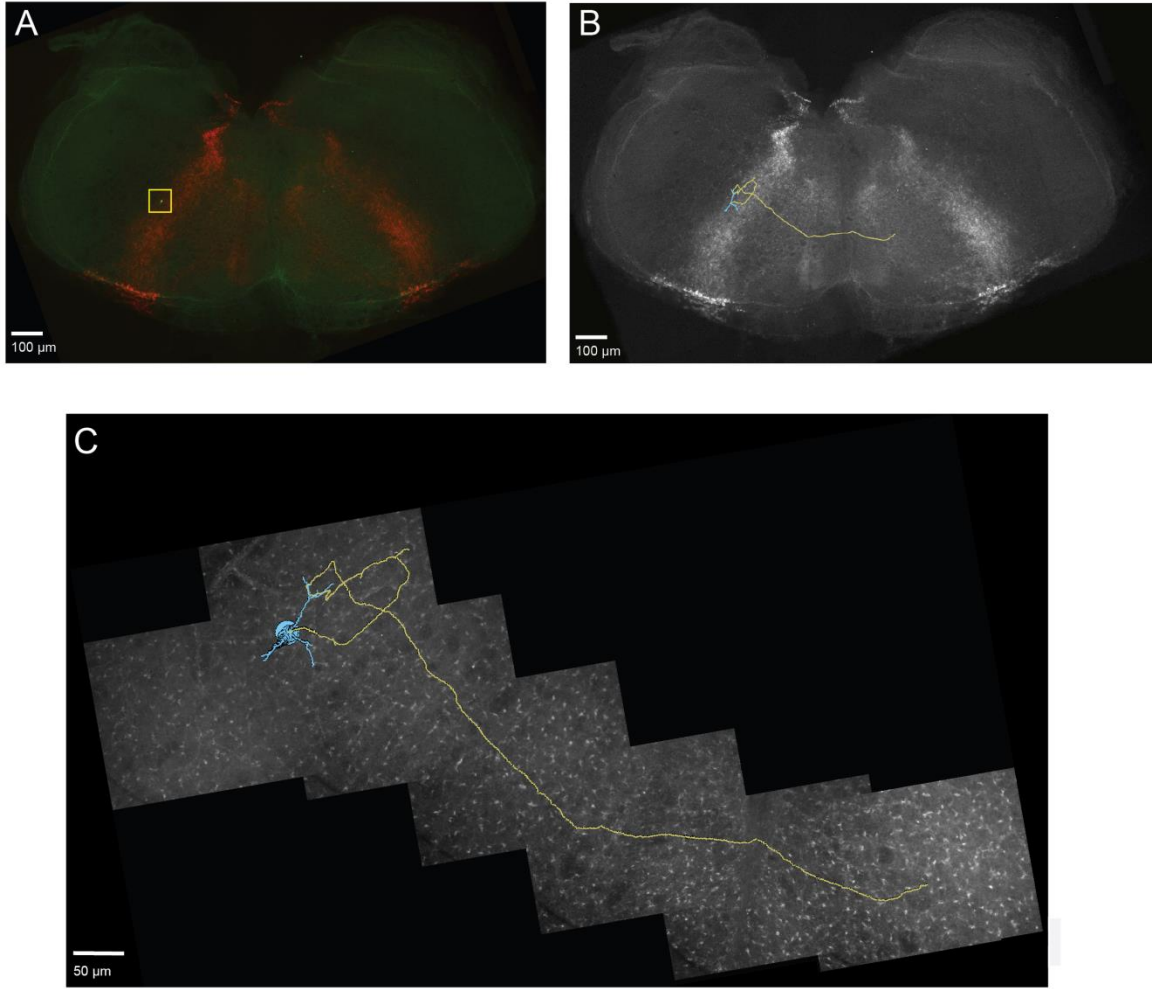


Figure 15. Dbx1 inspiratory cell 140207 in the reticular formation. A, slice mosaic showing Dbx1 expression via tdTomato transgenic labeling. Location of the cell body is highlighted with a yellow box; B, reconstructed cell morphology on the slice mosaic shows the axon crosses the midline; C, enlarged view of cell morphology showing dendritic tree

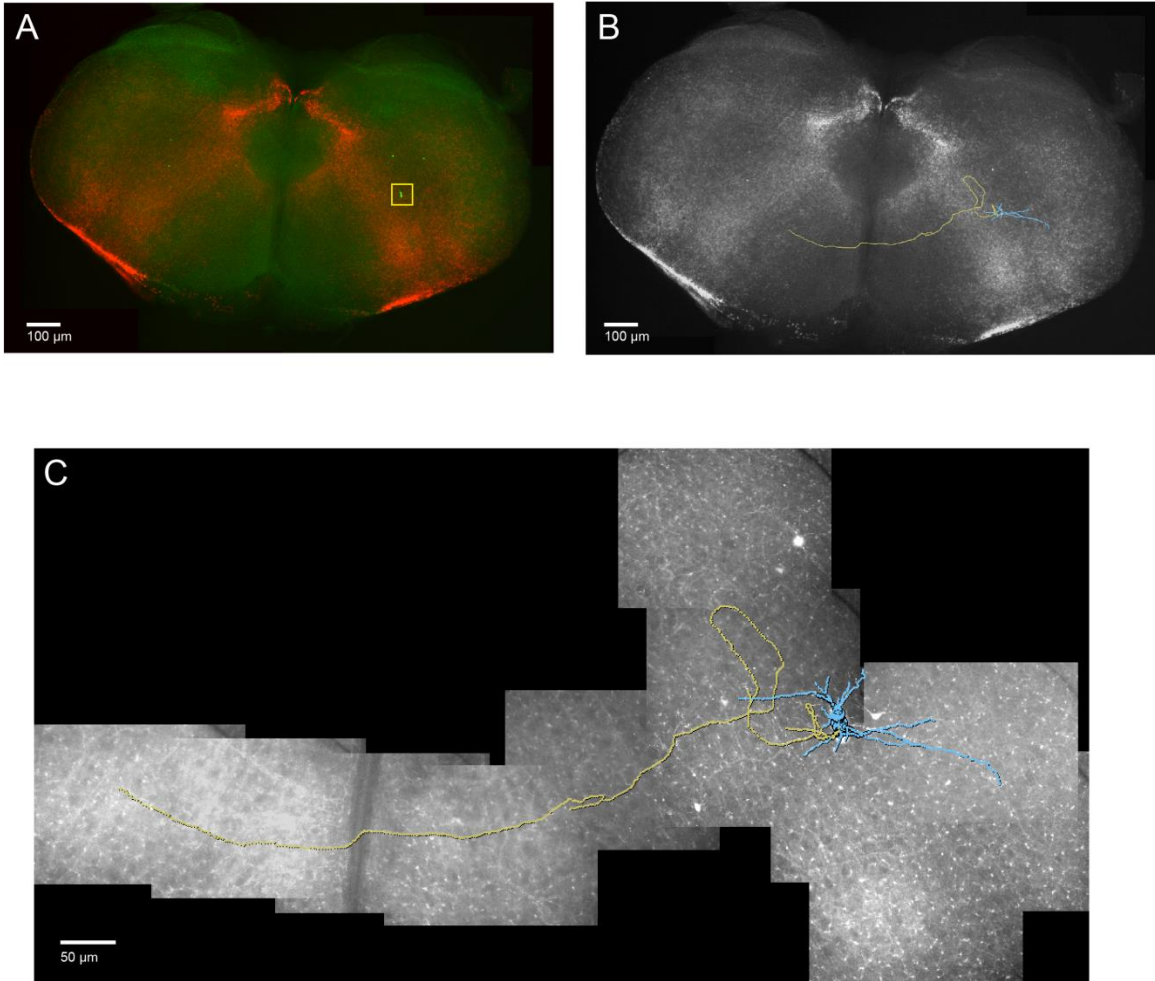


Figure 16. Dbx1 inspiratory cell 140221 in the reticular formation. A, slice mosaic showing Dbx1 expression via tdTomato transgenic labeling. Location of the cell body is highlighted with a yellow box; B, reconstructed cell morphology on the slice mosaic shows the axon crosses the midline; C, enlarged view of cell morphology showing dendritic tree

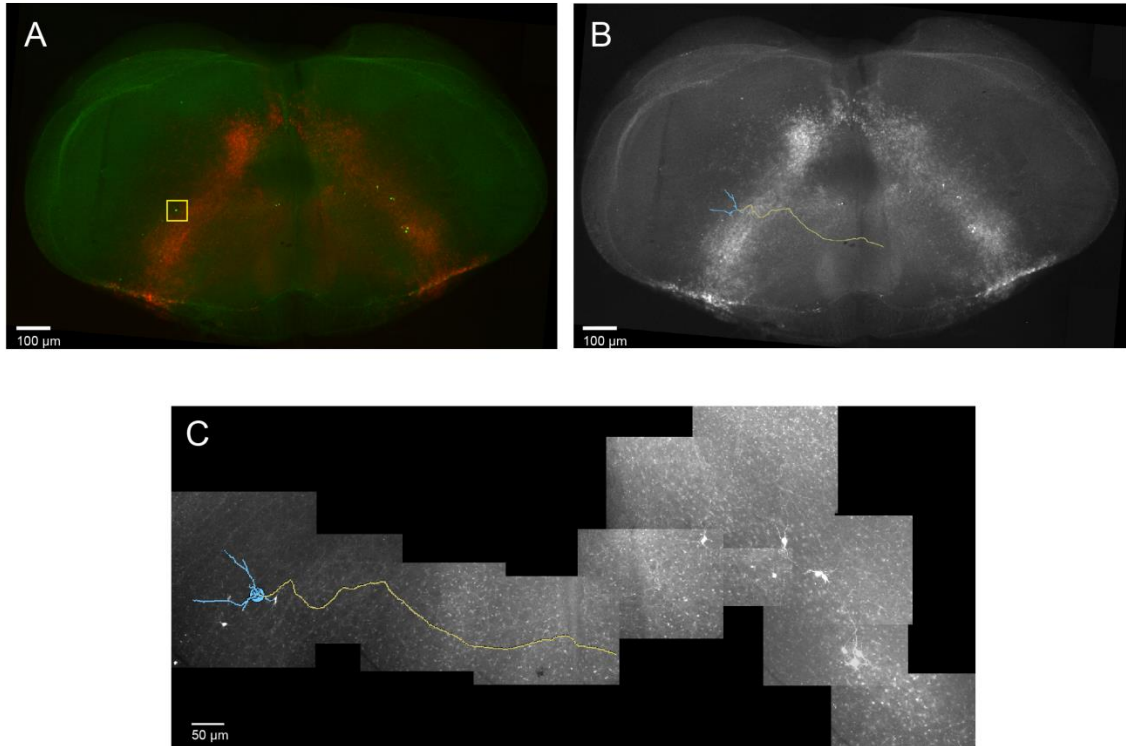


Figure 17. Dbx1 inspiratory cell 140306 in the reticular formation. A, slice mosaic showing Dbx1 expression via tdTomato transgenic labeling. Location of the cell body is highlighted with a yellow box; B, reconstructed cell morphology on the slice mosaic shows the axon crosses the midline; C, enlarged view of cell morphology showing dendritic tree

Reticular Formation – Ipsilateral Axon Projections

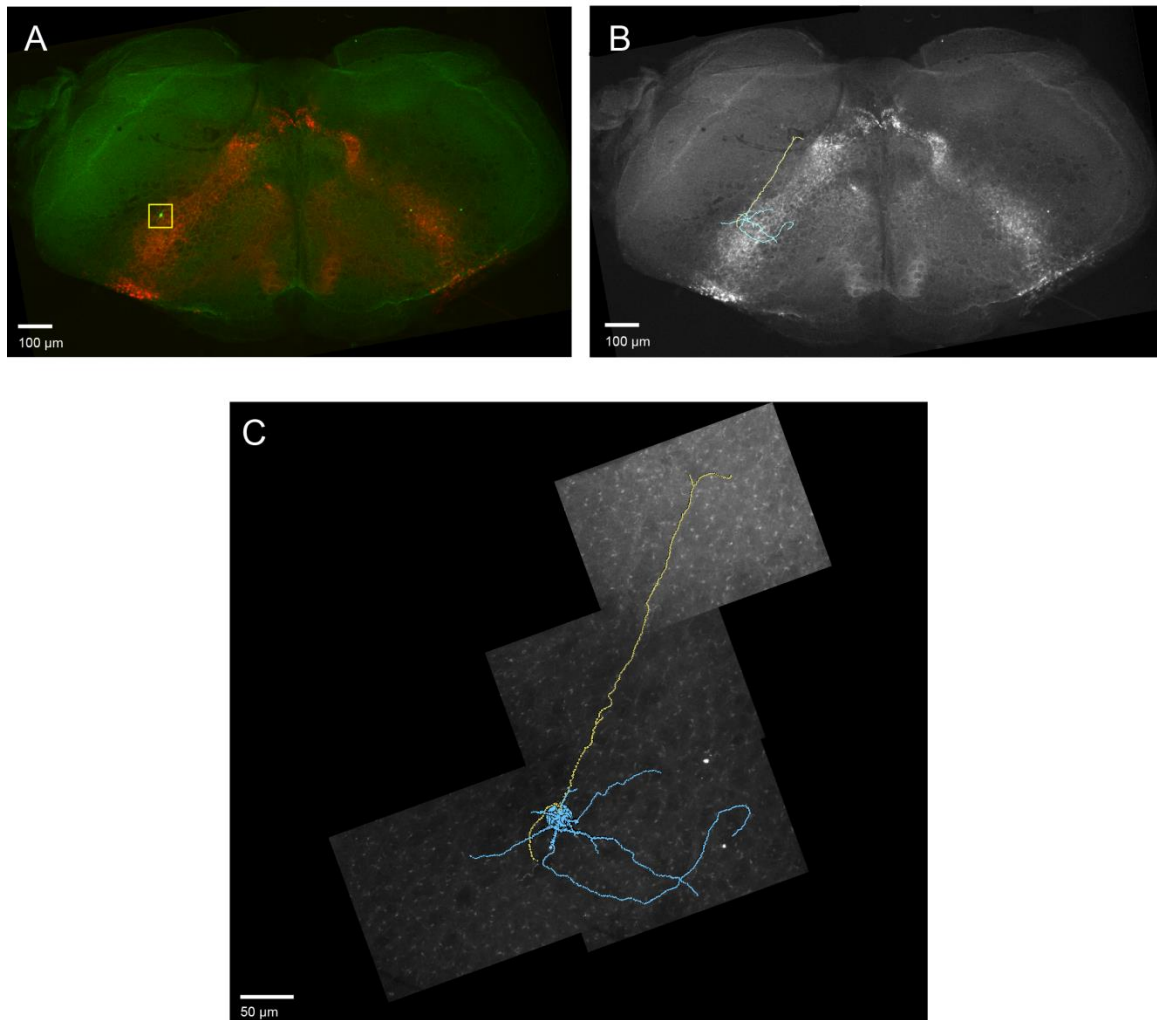


Figure 18. Dbx1 inspiratory cell 140208 in the reticular formation. A, slice mosaic showing Dbx1 expression via tdTomato transgenic labeling. Location of the cell body is highlighted with a yellow box; B, reconstructed cell morphology on the slice mosaic shows an ipsilateral axon projection toward the hypoglossal nucleus; C, enlarged view of cell morphology showing dendritic tree

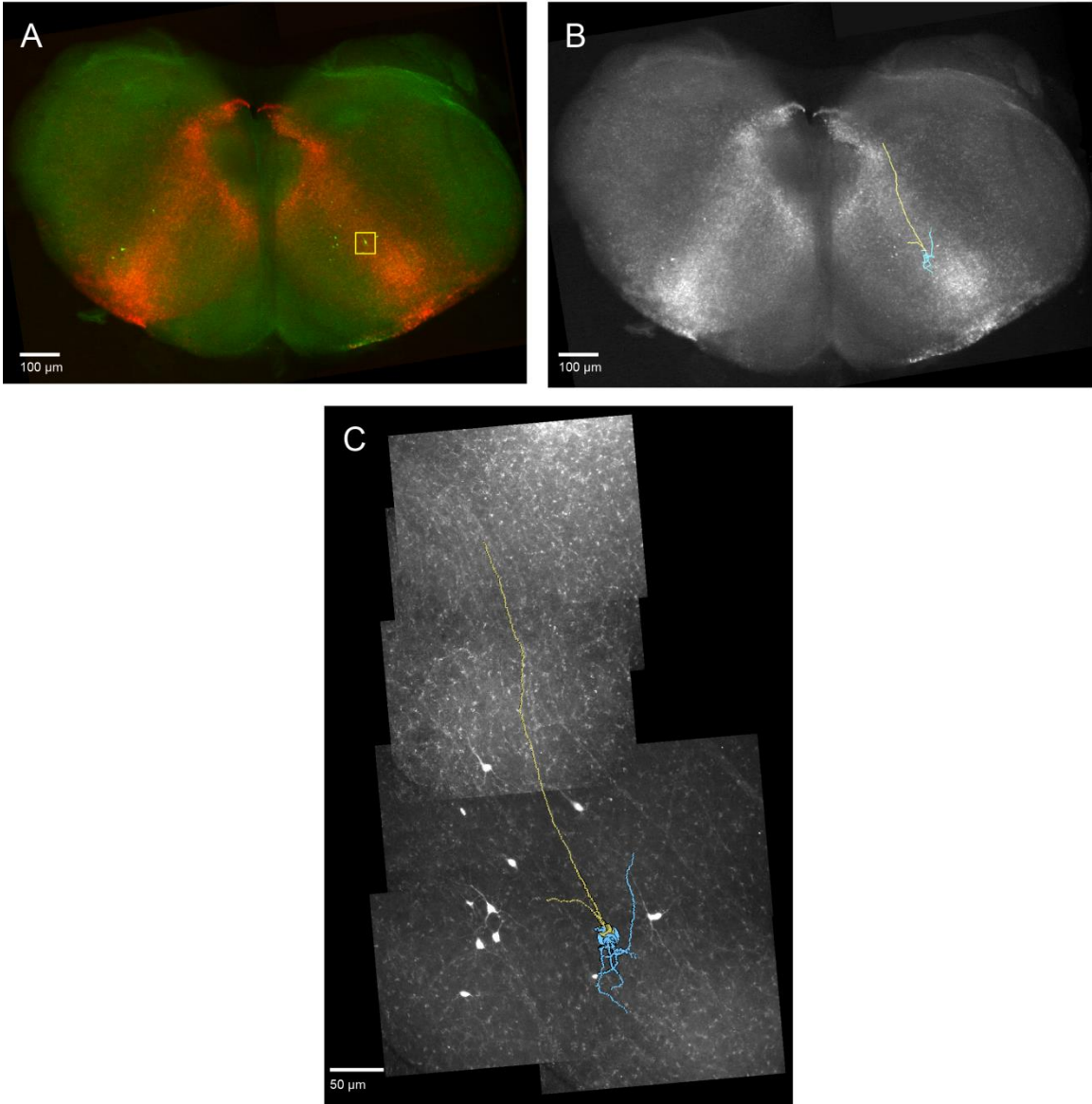


Figure 19. Dbx1 inspiratory cell 140220 in the reticular formation A, slice mosaic showing Dbx1 expression via tdTomato transgenic labeling. Location of the cell body is highlighted with a yellow box; B, reconstructed cell morphology on the slice mosaic shows an ipsilateral axon projection toward the hypoglossal motor nucleus; C, enlarged view of cell morphology showing dendritic tree

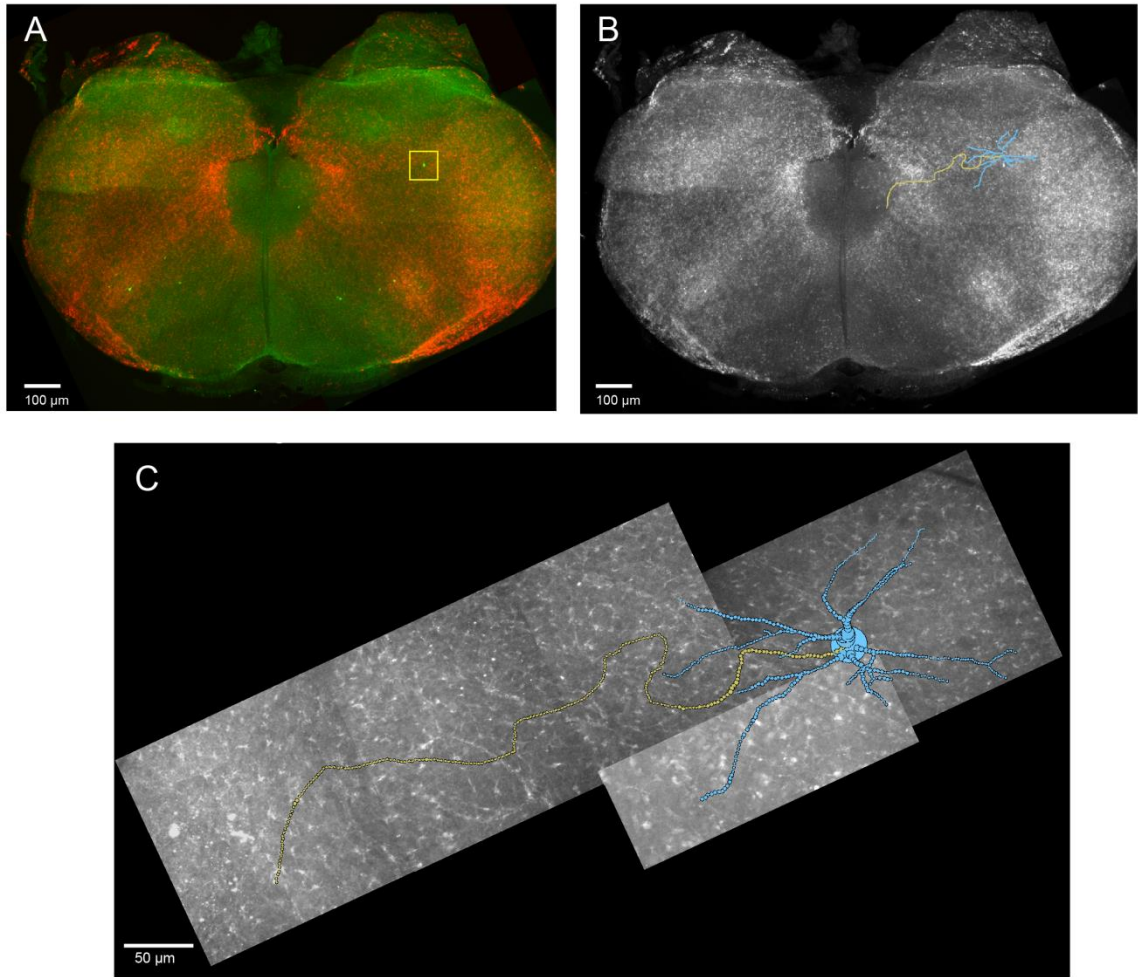


Figure 20. Dbx1 inspiratory cell 140301 in the reticular formation. A, slice mosaic showing Dbx1 expression via tdTomato transgenic labeling. Location of the cell body is highlighted with a yellow box; B, reconstructed cell morphology on the slice mosaic shows an ipsilateral axon projection toward the hypoglossal nucleus; C, enlarged view of cell morphology showing dendritic tree

PreBötC - Midline Axon Projections

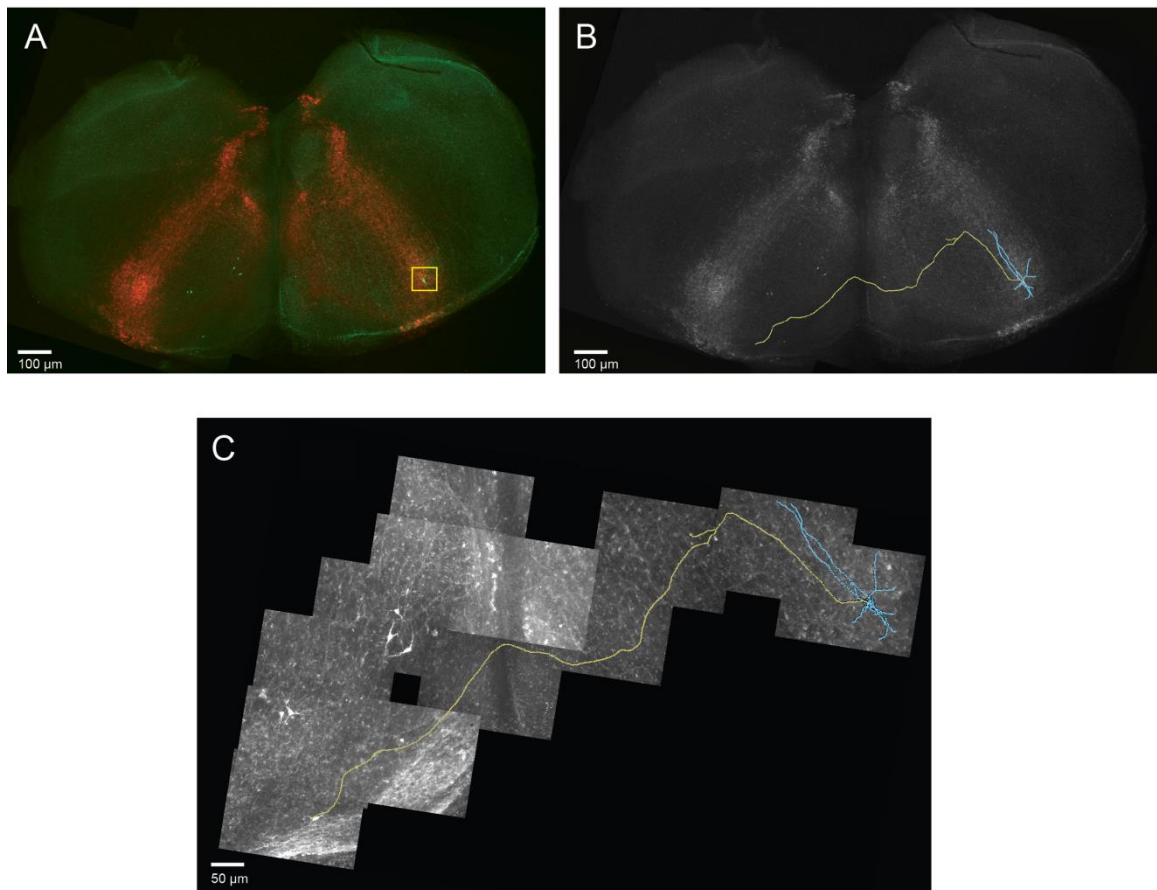


Figure 21. Dbx1 inspiratory cell 140127 in the preBötC. A, slice mosaic showing Dbx1 expression via tdTomato transgenic labeling. Location of the cell body is highlighted with a yellow box; B, reconstructed cell morphology on the slice mosaic shows a midline axon projection; C, enlarged view of cell morphology showing dendritic tree

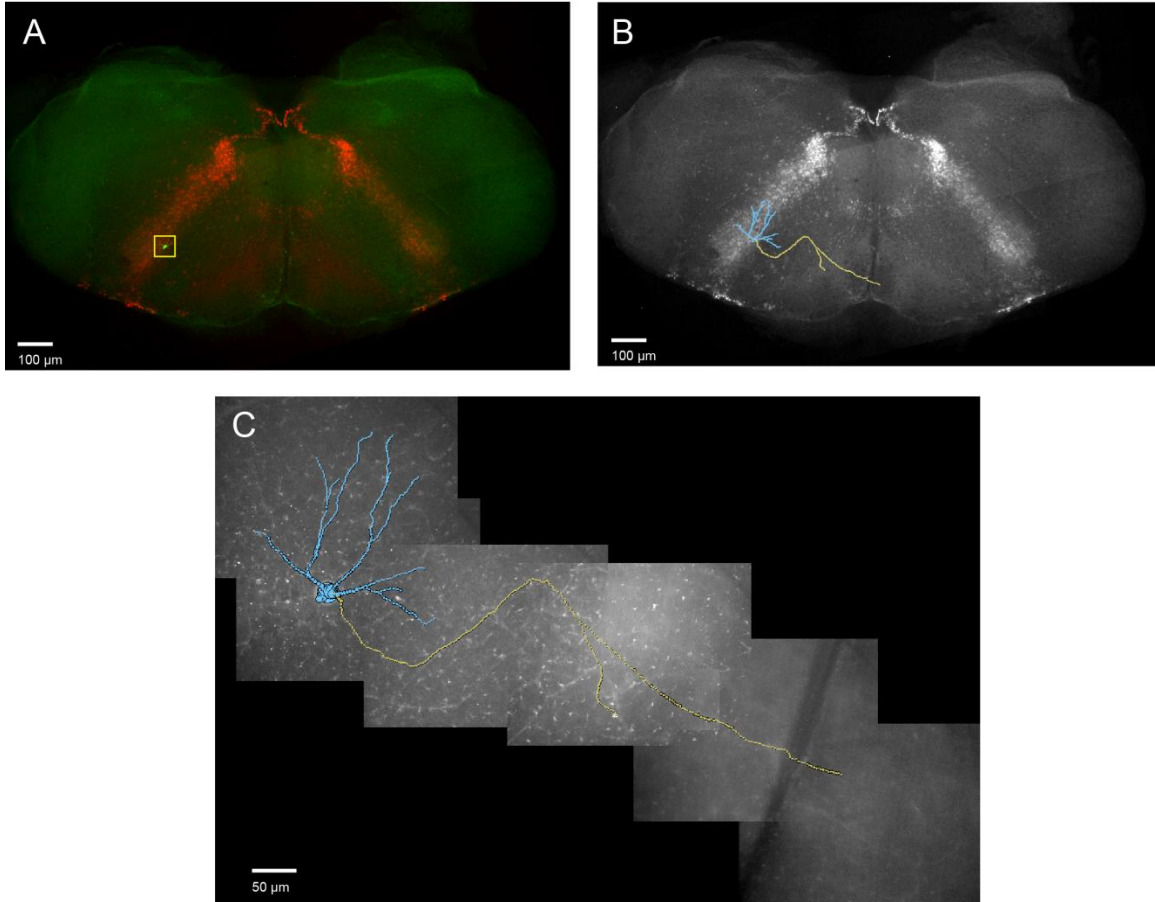


Figure 22. Dbx1 inspiratory cell 140109 in the preBötC. A, slice mosaic showing Dbx1 expression via tdTomato transgenic labeling. Location of the cell body is highlighted with a yellow box; B, reconstructed cell morphology on the slice mosaic shows a midline axon projection; C, enlarged view of cell morphology showing dendritic tree

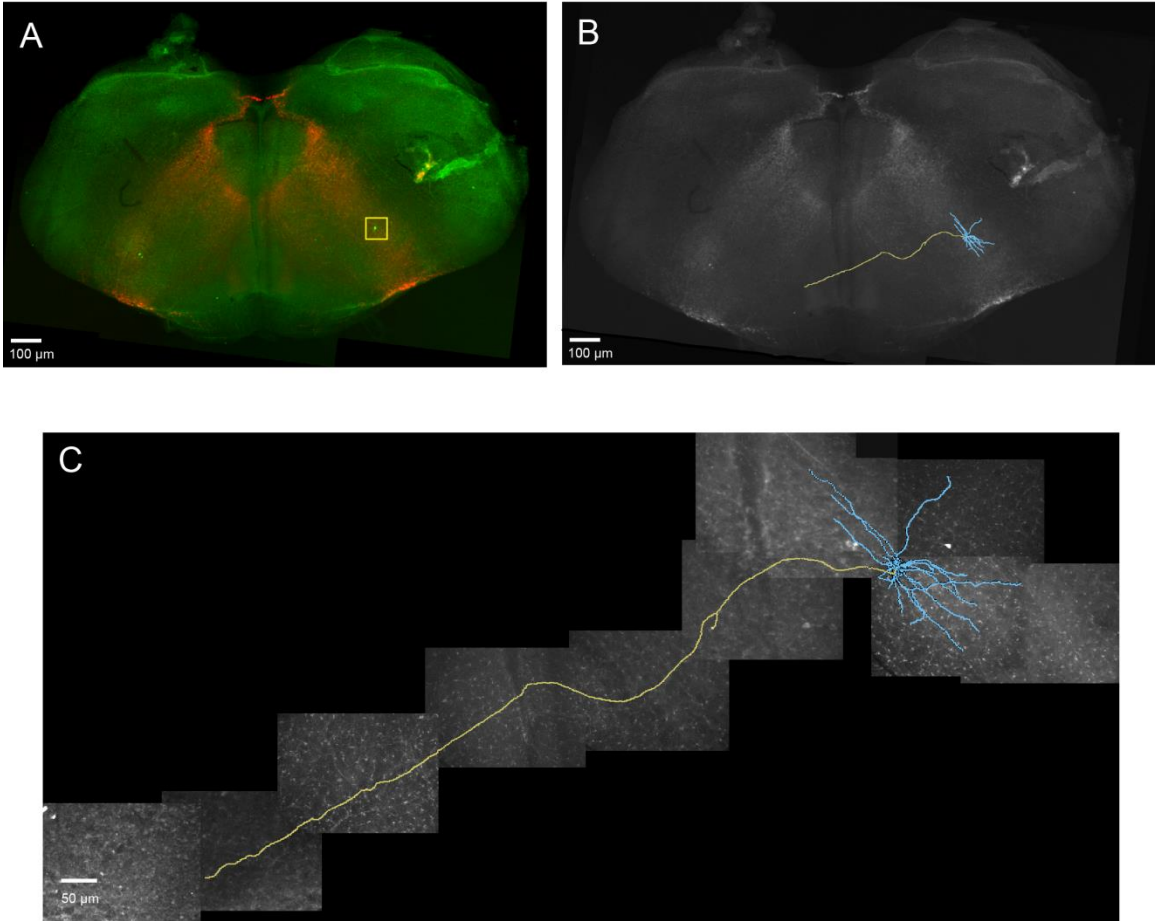


Figure 23. Dbx1 inspiratory cell 140117 in the preBötC A, slice mosaic showing Dbx1 expression via tdTomato transgenic labeling. Location of the cell body is highlighted with a yellow box; B, reconstructed cell morphology on the slice mosaic shows a midline axon projection; C, enlarged view of cell morphology showing dendritic tree

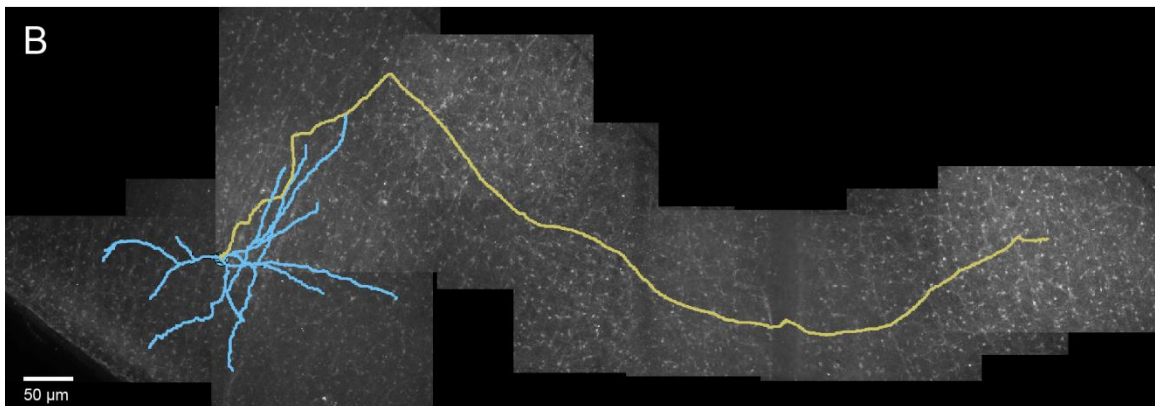
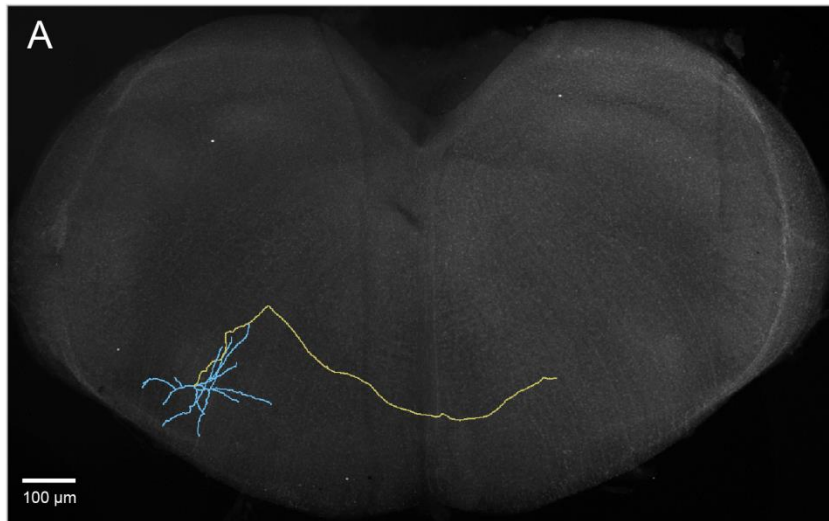


Figure 24. Dbx1 inspiratory cell 130910 in the preBötC. A, slice mosaic with reconstructed cell morphology on the slice mosaic shows a midline axon projection; tdTomato expression in Dbx1 neurons was not visible after histological processing but was present and visible during the experiment; C, enlarged view of cell morphology showing dendritic tree

PreBötC - Ipsilateral Axon Projections

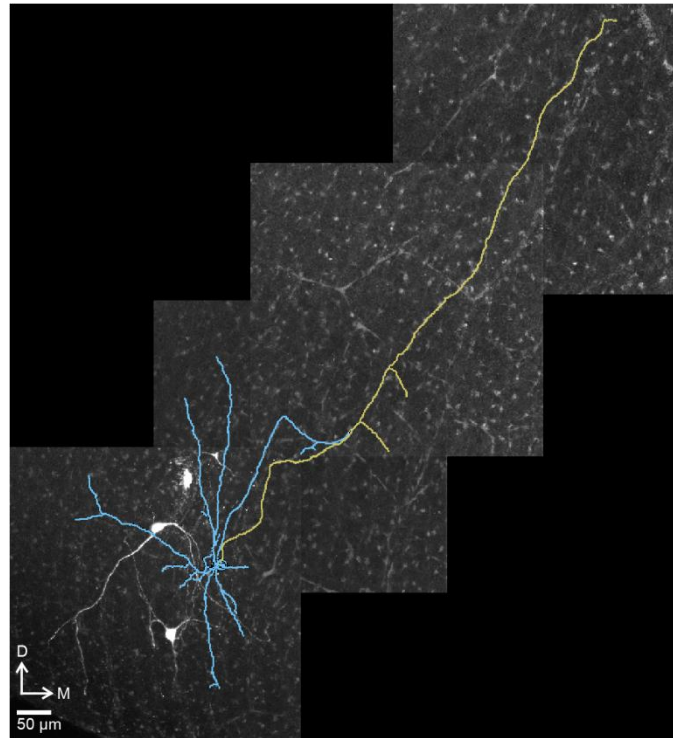


Figure 25. Dbx1 inspiratory cell 1 130212_1 in the preBötC. The reconstructed neuron is shown as an overlay over the confocal microscopy image. Dorsal and medial direction arrows indicate the slice orientation.

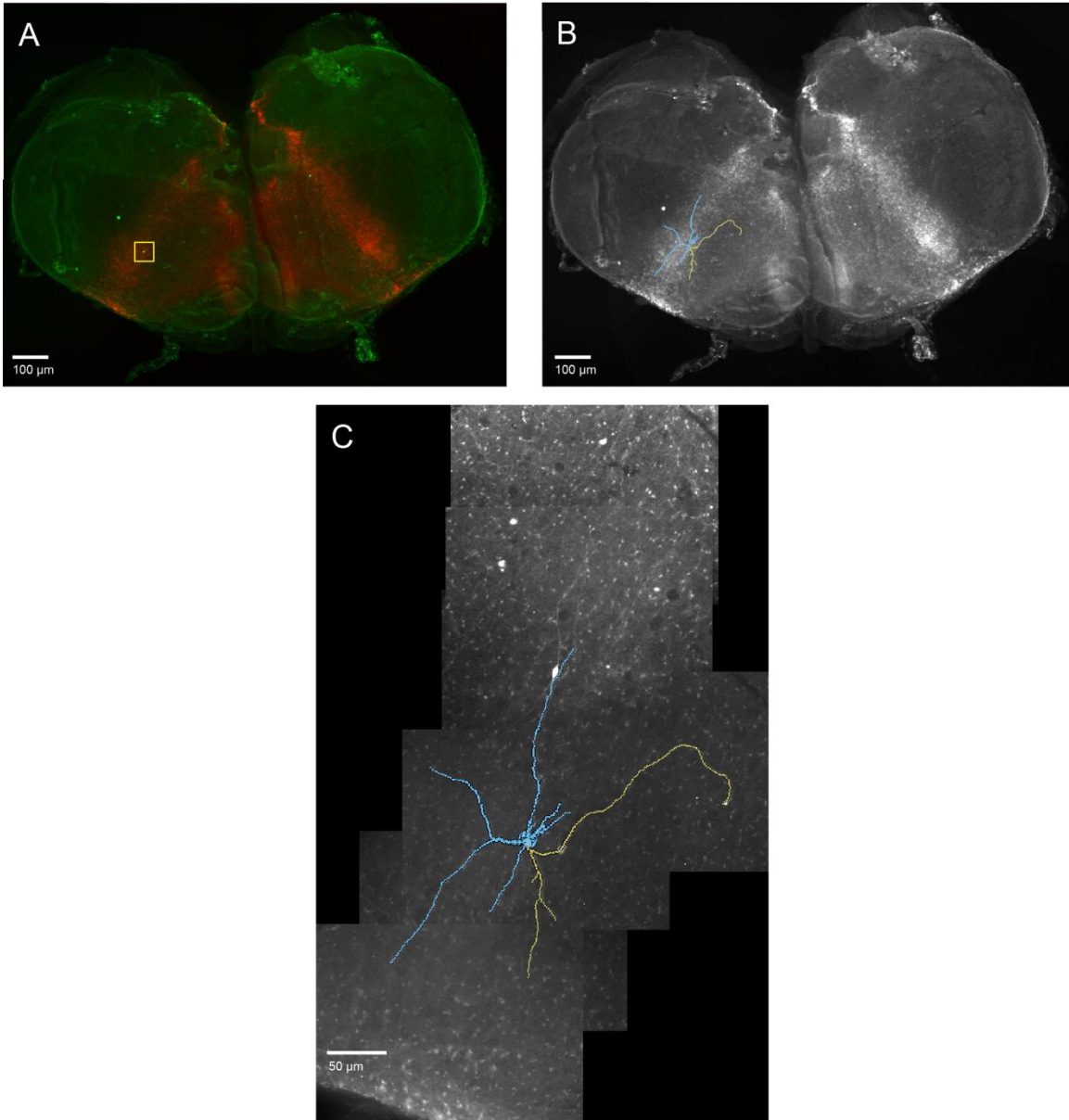


Figure 26. Dbx1 inspiratory cell 130625 in the preBötC. A, slice mosaic showing Dbx1 expression via tdTomato transgenic labeling. Location of the cell body is highlighted with a yellow box; B, reconstructed cell morphology on the slice mosaic shows an ipsilateral axon projection; C, enlarged view of cell morphology showing dendritic tree

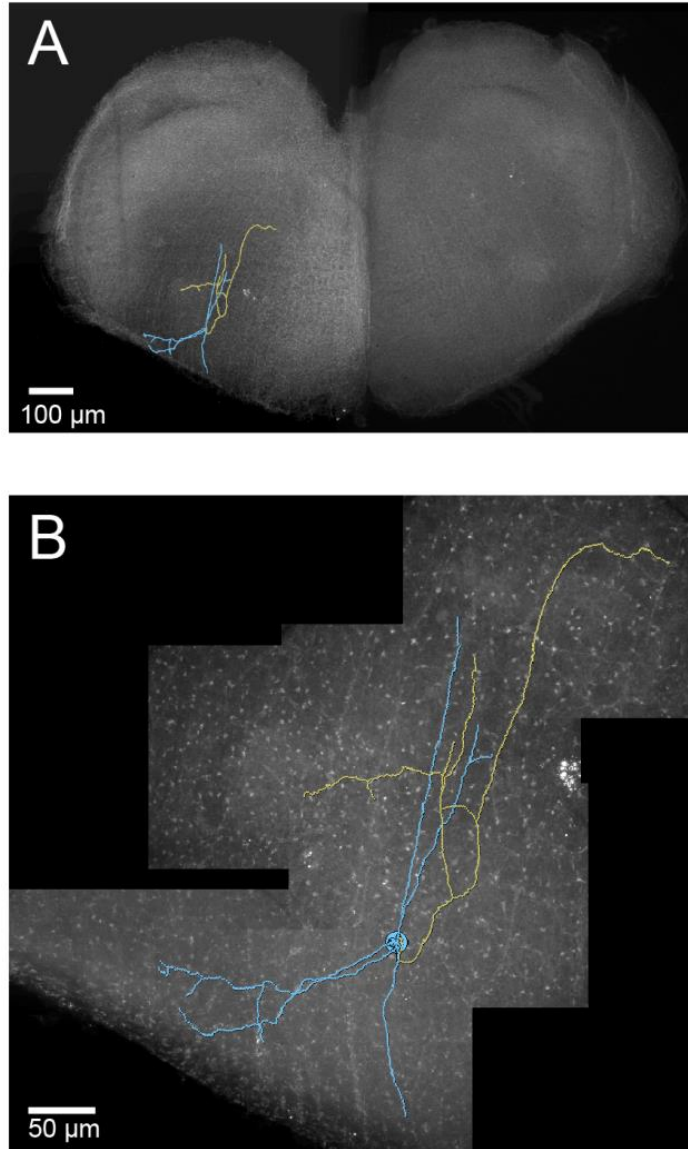


Figure 27. Dbx1 inspiratory cell 130819 in the preBötC. A, slice mosaic with reconstructed cell morphology on the slice mosaic shows an ipsilateral axon projection; tdTomato expression in Dbx1 neurons was not visible after histological processing but was present and visible during the experiment; C, enlarged view of cell morphology showing dendritic tree

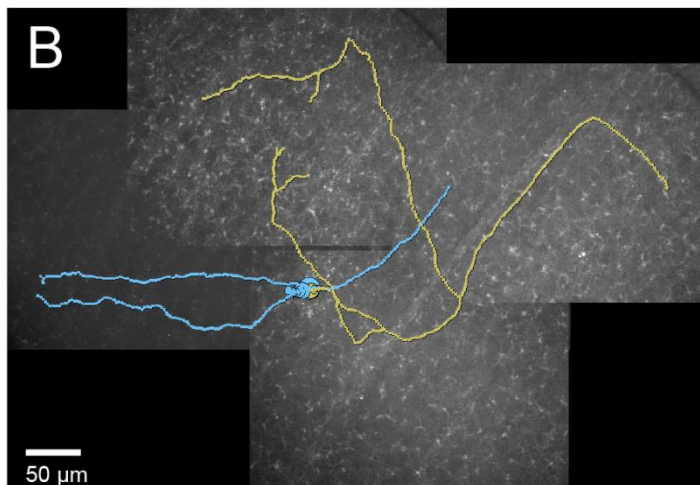
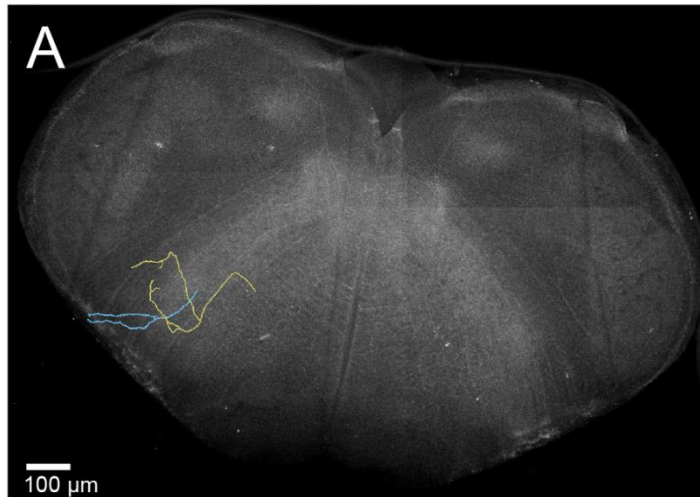


Figure 28. Dbx1 inspiratory cell 140110 in the preBötC. A, slice mosaic with reconstructed cell morphology on the slice mosaic shows an ipsilateral axon projection; tdTomato expression in Dbx1 neurons was not visible after histological processing but was present and visible during the experiment; C, enlarged view of cell morphology showing dendritic tree

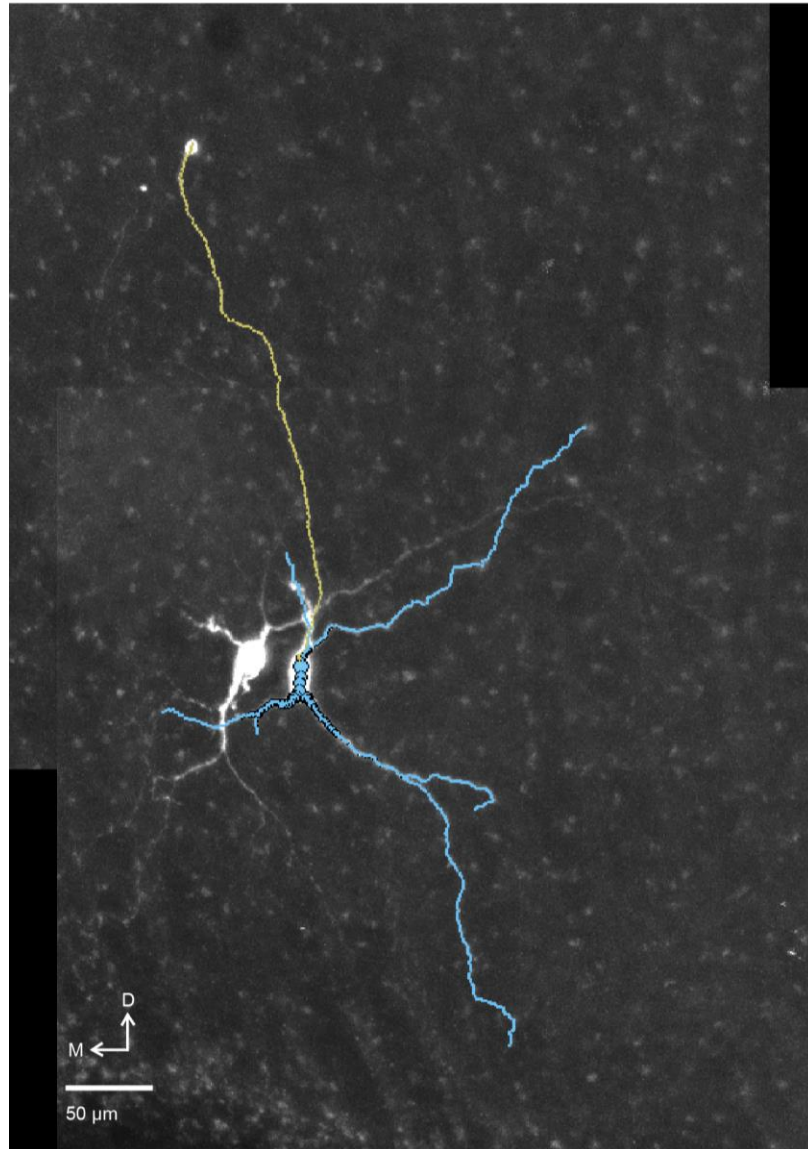


Figure 29. Dbx1 inspiratory cell 120417 in the preBötC. The reconstructed neuron is shown as an overlay over the confocal microscopy image. Dorsal and medial direction arrows indicate the slice orientation.

Dendritic Analysis Only

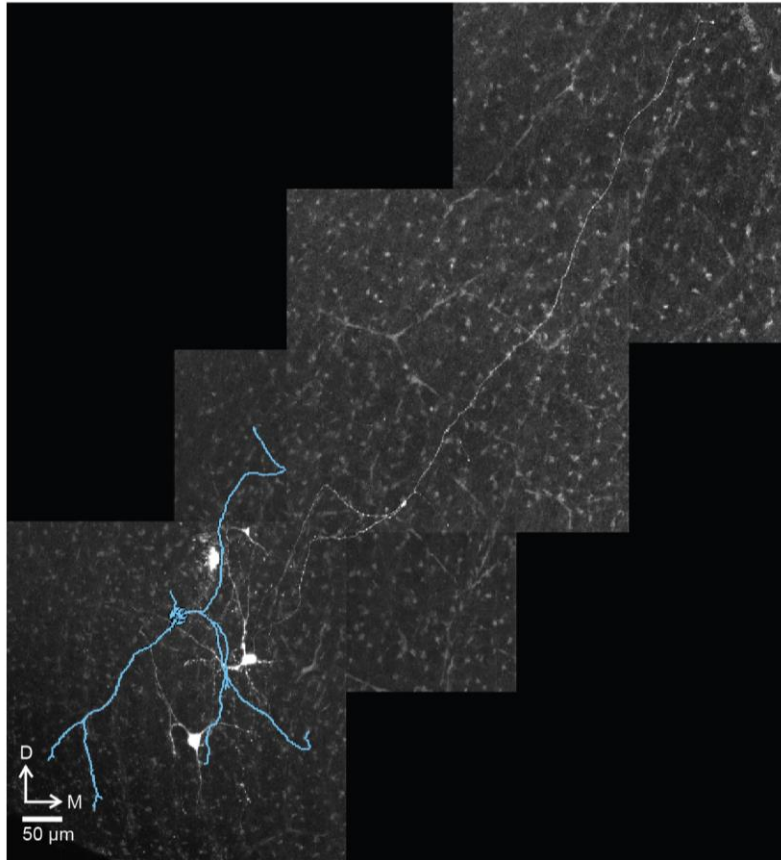


Figure 30. Dbx1 inspiratory cell 130212_2 in the preBötC. The reconstructed neuron is shown as an overlay over the confocal microscopy image. Dorsal and medial direction arrows indicate the slice orientation.

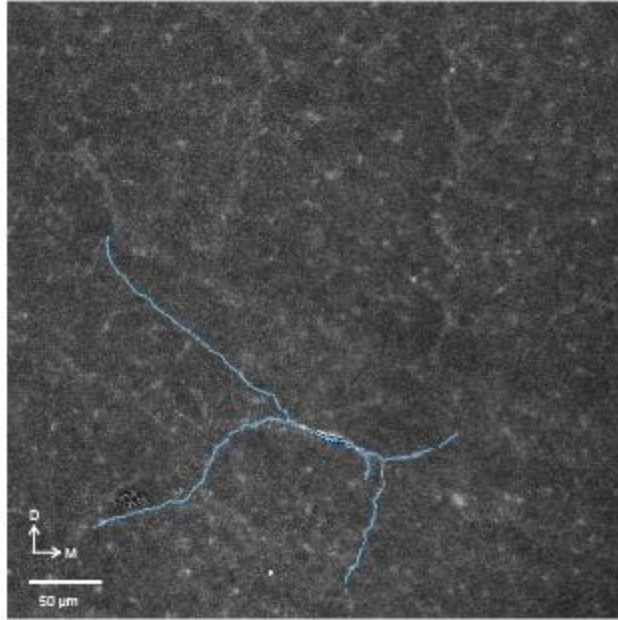


Figure 31. Dbx1 inspiratory cell 120621 in the preBötC. The reconstructed neuron is shown as an overlay over the confocal microscopy image. Dorsal and medial direction arrows indicate the slice orientation.

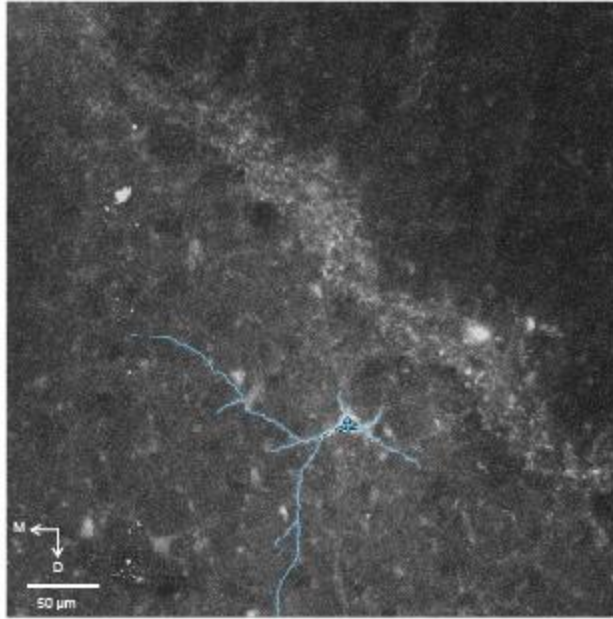


Figure 32. Dbx1 inspiratory cell 120623 in the preBötC. The reconstructed neuron is shown as an overlay over the confocal microscopy image. Dorsal and medial direction arrows indicate the slice orientation.

Morphometric property	Definition
Soma Surface	Surface area of the soma (area of a sphere) calculated with the equation $4\pi r^2$, where r is the radius of the soma
Number of Stems	Number of protrusions attached to the soma
Number of Bifurcations	Branch points resulting in two daughter branches
Number of Branches	Branch consists of dendritic compartments that lie between 2 branching points or between one branching point and a termination point
Number of tips	Final compartment or endpoint of each dendritic branch
Width	Horizontal span of dendrites calculated by the difference between maximum and minimum of x-coordinates in the xyz plane
Height	Vertical span of dendrites calculated by the difference between maximum and minimum of y-coordinates in the xyz plane
Depth	Span of dendrites perpendicular to the surface of the slice calculated by the difference between maximum and minimum of z-coordinates in the xyz plane
Diameter	Diameter of each compartment of the neuron
Length	Sum of the length of the entire dendritic tree
Surface Area	Surface area of each compartment (area of a cylinder) calculated by the equation $2\pi r h$, where r is the radius of the dendrite and h is the height
Volume	Calculated with the equation $\pi r^2 h$, where r is the radius of the dendrite and h is the height

Table 2. Definitions of morphometric properties analyzed

Morphometric property	Definition
Euclidean Distance	Straight line distance of the dendritic compartment from the soma
Path Distance	Sum of the lengths of the dendritic compartment from the soma
Branch Order	Hierarchy of branching where the soma = 0, the first bifurcation results in a branch order of 1, the second bifurcation the branch order = 2, etc.
Terminal Segment	Number of compartments in a branch that ends as a terminal branch (returns a 1 for all compartments in a terminal branch). This gives an idea of the length of the final branch
Burke Taper	Burke Taper which is measured between 2 bifurcation points (Diameter of bifurcation compartment minus previous bifurcation compartment diameter divided by total length of the branch)
Hillman Taper	Hillman Taper is measured by computing the ratio between the final diameter and initial diameter of a branch
Contraction	Ratio between Euclidean distance of a branch and its path length
Fragmentation	Total number of compartments that constitute a branch between 2 bifurcation points or between a bifurcation point and a terminal tip
Daughter Ratio	Ratio between 2 daughter compartments of a bifurcation (Daughter compartments are the two compartments that follow a bifurcation point)
Parent Daughter Ratio	Ratio between diameter of daughter and parent compartments of a bifurcation
Partition asymmetry	Calculated for each bifurcation via the equation $\frac{abs n1-n2 }{(n1+n2-2)}$, where n1 is the number of terminal tips on the left side of the bifurcation and n2 is the number of tips on the right side of the bifurcation
Rall power	The diameter value that best fits Ralls three-halves power law. This is the idealistic dendritic diameter that can propagate signal transmission without loss from the starting point to the terminal point in a cable model.

Table 2 (continued). Definitions of morphometric properties analyzed.

Morphometric property	Definition
Bifurcation amplitude local	Returns the angle (in degrees) between the first two compartments in a bifurcation
Bifurcation amplitude remote	Angle between 2 bifurcation points, between bifurcation point and terminal point, or between 2 terminal points (computed at each bifurcation point)
Bifurcation tilt local	angle between previous compartment of bifurcating parent and the 2 daughter compartments of the bifurcation; smaller of the 2 child angles is reported (consider as angle of deflection of the parent orientation compared to the orientation of the midline of the bifurcation amplitude angle)
Bifurcation tilt remote	angle between previous parent node and two daughter nodes of a bifurcation (node is terminating point, bifurcation point, or root point) The smaller of the 2 angles is returned; not computed for the root node
Bifurcation torque local	angle between the plane of previous bifurcation and the current bifurcation (bifurcation plane is defined by the two daughter compartments leaving the bifurcation)(torque is the inner angle measured between 2 planes of bifurcations)
Bifurcation torque remote	Angle between the current plane of bifurcation and previous plane of bifurcation
last-parent diameter	Diameter of last bifurcation before the terminal tips
Diameter threshold	Diameter of the first compartment after the last bifurcation leading to a terminal tip
Hilmann threshold	Weighted average between 50% of parent and 25% of daughter diameters of the terminal bifurcation
Fractal diameter	Slope of linear fit of regression line obtained from the log-log plot of path distance vs Euclidean distance

Table 2 (continued). Definitions of morphometric properties

Row Number	preBötC Neuron Index	1	2	3	4	5	6
		Soma Surface (μm^2)	Number of Stems	Number of Bifurcations	Number of Branches	Number of Tips	Width (μm)
1	111101	364	5	14	33	19	703
2	111102_1	606	4	6	16	10	348
3	111102_2	354	5	9	23	14	565
4	111108	702	5	8	21	13	351
5	111109_1	467	4	17	38	21	518
6	111109_2	856	6	22	50	28	397
7	111208	466	4	6	16	10	271
8	111209	497	4	12	28	16	576
9	111212	742	3	28	59	31	524
10	111214	864	5	5	15	10	626
11	111219_S1	664	4	16	36	20	722
12	111219_S2	416	4	13	30	17	620
13	111220_1	524	5	10	25	15	1021
14	111220_2	337	6	16	38	22	1081
15	120621	81	2	4	10	7	246
16	120623	134	3	6	15	10	194
17	130819	452	3	8	19	12	250
18	130910	333	3	11	25	15	296
19	130212_1	947	3	8	19	12	392
20	130212_2	603	6	17	40	24	321
21	140110	402	3	3	9	7	288
22	140117	1198	6	20	46	27	295
23	140127	509	5	7	19	13	224

Table 3. Morphometric properties of Dbx1 neurons in the preBötC. Data shaded gray were reported in a previous thesis (Weragalaarachchi, 2012), but used in the current analysis. Unshaded data are calculated from new digital reconstructions. The entire table spans 37 columns and 23 rows. Columns 1-6 are shown in this portion of the table. The subsequent columns will be continued on the following pages.

		7	8	9	10	11	12
Row Number	preBötC Neuron Index	Height (µm)	Depth (µm)	Average diameter (µm)	Length (µm)	Surface Area (µm ²)	Volume (µm ³)
1	111101	353	42	0.9	3578	10108	3155
2	111102_1	313	51	1.1	1379	4861	1922
3	111102_2	340	48	0.9	1620	4893	2085
4	111108	500	19	1	1355	4214	1600
5	111109_1	481	41	1.4	2655	11740	5701
6	111109_2	361	38	1.1	2268	8432	4354
7	111208	260	30	0.9	1018	2853	904
8	111209	270	67	0.7	1402	2955	901
9	111212	489	40	0.9	2682	7946	3719
10	111214	578	65	0.5	2621	4039	1096
11	111219_S1	410	31	0.7	2254	4967	1460
12	111219_S2	192	67	0.8	1606	4009	929
13	111220_1	555	67	0.6	2590	4878	1484
14	111220_2	764	25	0.4	2753	3700	759
15	120621	242	30	1.0	708	2159	725
16	120623	191	38	0.9	637	1715	730
17	130819	373	21	1.7	1177	7090	6749
18	130910	258	29	1.9	1565	9873	7487
19	130212_1	475	24	2.4	1317	11470	18945
20	130212_2	465	38	2.2	1963	14771	15880
21	140110	100	24	2.3	585	4878	6203
22	140117	252	32	2.4	1987	17937	30964
23	140127	197	33	2.5	914	8055	10481

Table 3 (continued). Morphometric properties of Dbx1 neurons in the preBötC. Data shaded gray was reported in a previous thesis, but used in the current analysis. Unshaded data are calculated from new reconstructions. The entire table spans 37 columns and 23 rows. Columns 7-12 are shown in this portion of the table. The subsequent columns will be continued on the following pages.

		13	14	15	16	17
Row Number	preBötC Neuron Index	Average Euclidean Distance (μm)	Maximum Euclidean Distance (μm)	Average Path Distance (μm)	Maximum Path Distance (μm)	Average Branch Order
1	111101	156	419	308	891	2.0
2	111102_1	102	250	150	363	2.3
3	111102_2	146	416	164	457	1.4
4	111108	157	429	174	480	1.4
5	111109_1	136	452	218	763	2.0
6	111109_2	106	315	134	344	2.1
7	111208	99	286	204	480	1.8
8	111209	153	378	201	444	3.0
9	111212	146	436	162	475	2.9
10	111214	193	427	239	608	1.2
11	111219_S1	233	730	467	1295	3.5
12	111219_S2	158	500	191	645	1.6
13	111220_1	294	850	359	1084	1.0
14	111220_2	365	1183	496	1570	1.4
15	120621	82	204	102	234	1.2
16	120623	65	158	86	218	1.6
17	130819	101	247	117	284	1.1
18	130910	73	192	107	292	2.2
19	130212_1	134	258	164	362	1.5
20	130212_2	123	300	143	369	1.4
21	140110	89	190	98	222	0.4
22	140117	70	186	89	241	2.1
23	140127	79	226	88	243	1.4

Table 3 (continued). Morphometric properties of Dbx1 neurons in the preBötC. Data shaded gray was reported in a previous thesis, but used in the current analysis. Unshaded data are calculated from new reconstructions. The entire table spans 37 columns and 23 rows. Columns 13-17 are shown in this portion of the table. The subsequent columns will be continued on the following pages.

		18	19	20	21	22	23
Row Number	preBötC Neuron Index	Terminal segments	Average Burke Taper (μm)	Maximum Burke taper (μm)	Average Hillman Taper (μm)	Maximum Hillman Taper (μm)	Average Contraction
1	111101	758	0.06	0.37	0.53	0.9	0.89
2	111102_1	324	0.03	0.16	0.62	1.0	0.87
3	111102_2	409	0.04	0.25	0.65	1.0	0.89
4	111108	293	0.04	0.15	0.73	1.0	0.93
5	111109_1	534	0.03	0.14	0.39	1.0	0.91
6	111109_2	476	0.04	0.20	0.50	1.0	0.88
7	111208	156	0.01	0.05	0.56	1.0	0.86
8	111209	207	0.03	0.13	0.50	1.0	0.90
9	111212	782	0.04	0.28	0.61	1.0	0.92
10	111214	1286	0.00	0.01	0.86	1.0	0.86
11	111219_S1	834	0.03	0.11	0.46	1.0	0.90
12	111219_S2	807	0.04	0.20	0.52	1.0	0.87
13	111220_1	1038	0.04	0.30	0.70	1.0	0.89
14	111220_2	1310	0.02	0.11	0.66	1.0	0.89
15	120621	365	0.05	0.27	0.37	0.7	0.88
16	120623	145	0.09	0.74	0.49	0.9	0.83
17	130819	348	0.21	2.87	0.27	0.9	0.87
18	130910	671	0.11	1.128	0.18	0.8	0.88
19	130212_1	373	0.07	0.66	0.21	0.9	0.90
20	130212_2	573	0.13	1.20	0.29	0.9	0.91
21	140110	170	0.14	1.00	0.35	0.9	0.95
22	140117	1114	0.64	9.19	0.42	0.9	0.90
23	140127	461	0.24	1.28	0.50	0.9	0.92

Table 3 (continued). Morphometric properties of Dbx1 neurons in the preBötC. Data shaded gray was reported in a previous thesis, but used in the current analysis. Unshaded data are calculated from new reconstructions. The entire table spans 37 columns and 23 rows. Columns 18-23 are shown in this portion of the table. The subsequent columns will be continued on the following pages.

		24	25	26	27	28	29
Row Number	preBötC Neuron Index	Average Daughter Ratio	Average Parent-Daughter Ratio	Average partition asymmetry	Average Rall power	Average Bifurcation amplitude local	Average Bifurcation amplitude remote
1	111101	1.31	0.78	0.41	3.2	84.0	81.4
2	111102_1	1.13	0.77	0.50	0.0	95.0	75.7
3	111102_2	1.21	0.78	0.57	2.5	80.7	66.9
4	111108	1.10	0.76	0.52	2.6	54.3	56.9
5	111109_1	1.16	0.91	0.55	1.3	68.7	54.3
6	111109_2	1.13	0.84	0.49	3.8	65.2	50.4
7	111208	1.16	0.75	0.64	2.6	118.1	118.1
8	111209	1.28	0.82	0.70	3.6	68.2	71.3
9	111212	1.11	0.92	0.55	3.7	65.7	52.0
10	111214	1.08	0.71	0.67	0.0	94.0	92.2
11	111219_S1	1.10	0.88	0.48	4.5	91.7	84.1
12	111219_S2	1.17	0.83	0.61	3.5	69.3	65.6
13	111220_1	1.33	0.79	0.46	2.4	86.6	66.5
14	111220_2	1.13	0.84	0.55	3.4	70.2	75.0
15	120621	1.13	0.92	0.50	2.9	93.1	100.8
16	120623	1.05	0.88	0.39	3.9	66.2	59.4
17	130819	1.09	0.85	0.63	2.0	61.7	59.2
18	130910	1.13	0.97	0.59	0.0	59.9	70.3
19	130212_1	1.06	0.90	0.25	3.9	68.6	57.8
20	130212_2	1.26	0.85	0.53	1.7	96.9	82.8
21	140110	1.07	0.79	0.33	0.0	62.8	63.5
22	140117	1.29	0.77	0.51	2.4	60.3	39.3
23	140127	1.11	0.81	0.57	2.3	56.9	60.9

Table 3 (continued). Morphometric properties of Dbx1 neurons in the preBötC. Data shaded gray was reported in a previous thesis, but used in the current analysis. Unshaded data are calculated from new reconstructions. The entire table spans 37 columns and 23 rows. Columns 24-29 are shown in this portion of the table. The subsequent columns will be continued on the following pages.

		30	31	32	33	34
Row Number	preBötC Neuron Index	Average bifurcation tilt local	Average bifurcation tilt remote	Average bifurcation torque local	Average bifurcation torque remote	Average last-parent diameter
1	111101	111.4	95.6	96.4	81.9	1.2
2	111102_1	91.1	103.9	110.7	119.1	1.2
3	111102_2	121.3	127.4	108.9	97.3	0.9
4	111108	125.8	117.0	92.4	100.9	1.0
5	111109_1	122.5	135.4	96.4	78.9	1.5
6	111109_2	125.4	130.4	106.6	92.3	1.1
7	111208	91.4	93.8	73.1	50.0	1.0
8	111209	123.8	118.1	47.7	78.2	0.6
9	111212	129.7	138.5	108.9	97.7	0.8
10	111214	96.8	126.0	80.7	81.8	5.8
11	111219_S1	111.1	112.3	106.7	101.8	0.9
12	111219_S2	112.6	117.2	99.2	76.3	1.0
13	111220_1	108.9	128.5	87.4	84.4	0.6
14	111220_2	120.8	111.3	90.2	73.4	0.3
15	120621	127.0	120.4	166.7	116.9	1.1
16	120623	126.9	129.8	82.4	89.8	0.9
17	130819	118.9	135.3	110.2	81.5	1.9
18	130910	125.7	128.3	100.1	83.9	1.7
19	130212_1	120.1	131.8	70.6	70.5	2.0
20	130212_2	91.6	102.4	125.4	89.8	2.1
21	140110	119.7	121.8	82.1	81.4	4.4
22	140117	118.6	139.0	102.0	106.6	2.9
23	140127	135.6	133.1	75.4	51.6	3.7

Table 3 (continued). Morphometric properties of Dbx1 neurons in the preBötC. Data shaded gray was reported in a previous thesis, but used in the current analysis. Unshaded data are calculated from new reconstructions. The entire table spans 37 columns and 23 rows. Columns 30-34 are shown in this portion of the table. The subsequent columns will be continued on the following pages.

		35	36	37
Row Number	preBötC Neuron Index	Average Diameter threshold	Average Hilmann threshold	Average fractal Diameter
1	111101	1.11	0.93	1.03
2	111102_1	1.96	0.98	1.03
3	111102_2	1.07	0.70	1.04
4	111108	1.26	0.67	1.02
5	111109_1	1.60	1.30	1.03
6	111109_2	1.07	0.89	1.05
7	111208	1.47	0.82	1.04
8	111209	0.84	0.44	1.06
9	111212	0.89	0.53	1.03
10	111214	1.16	2.95	1.02
11	111219_S1	0.96	0.75	1.04
12	111219_S2	1.03	0.73	1.05
13	111220_1	0.95	0.42	1.04
14	111220_2	0.53	0.18	1.05
15	120621	2.30	2.31	1.04
16	120623	2.31	2.45	1.08
17	130819	4.55	4.62	1.05
18	130910	3.65	3.60	1.03
19	130212_1	5.98	6.87	1.03
20	130212_2	4.15	4.23	1.04
21	140110	7.57	8.46	1.02
22	140117	5.18	6.01	1.04
23	140127	6.23	7.24	1.03

Table 3 (continued). Morphometric properties of Dbx1 neurons in the preBötC. Data shaded gray was reported in a previous thesis, but used in the current analysis. Unshaded data are calculated from new reconstructions. The entire table spans 37 columns and 23 rows. Columns 35-37 are shown in this portion of the table.

		1	2	3	4	5	6
Row Number	Reticular Formation Neuron Index	Soma Surface (μm^2)	Number of Stems	Number of Bifurcations	Number of Branches	Number of Tips	Width (μm)
1	130624	490	4	6	16	11	58
2	130625	450	4	5	14	10	152
3	140109	644	4	8	20	13	164
4	140114	685	5	11	27	17	364
5	140120	628	5	2	9	8	146
6	140124	530	3	7	17	11	219
7	140207	473	3	5	13	9	82
8	140208	1142	4	8	20	13	265
9	140220	739	2	7	17	11	43
10	140221	1214	2	6	16	11	204
11	140301	1184	5	10	25	16	255
12	140306	921	3	5	13	9	123

Table 4. Morphometric properties of Dbx1 neurons in the reticular formation. The entire table consists of 37 columns and 12 rows. Columns 1-6 are shown in this portion of the table. The table will continue on the subsequent pages.

		7	8	9	10	11	12
Row Number	Reticular Formation Neuron Index	Height (μm)	Depth (μm)	Average Diameter (μm)	Length (μm)	Surface Area (μm ²)	Volume (μm ³)
1	130624	188	6	2.4	417	3468	3787
2	130625	262	17	3.0	647	6622	8866
3	140109	175	40	2.7	929	9155	13685
4	140114	295	25	1.9	1248	9088	13255
5	140120	134	13	3.4	381	5315	11430
6	140124	152	24	2.6	616	5778	8596
7	140207	88	14	3.3	250	4157	14877
8	140208	139	41	2.7	954	10418	24236
9	140220	144	27	3.1	383	4854	11246
10	140221	89	28	2.8	582	7282	21156
11	140301	157	15	3.4	816	10655	24759
12	140306	92	18	2.8	318	4323	13600

Table 4 (continued). Morphometric properties of Dbx1 neurons in the reticular formation. The entire table consists of 37 columns and 12 rows. Columns 7-12 are shown in this portion of the table. The table will continue on the subsequent pages.

		13	14	15	16	17
Row Number	Reticular Formation Neuron Index	Average Euclidean Distance (μm)	Maximum Euclidean Distance (μm)	Average Path Distance (μm)	Maximum Path Distance (μm)	Average Branch Order
1	130624	36.4	102	39	109	1.0
2	130625	62.7	164	71	194	1.1
3	140109	79.0	156	94	196	1.4
4	140114	92.3	229	109	226	1.3
5	140120	64.5	163	70	176	0.1
6	140124	50.9	128	58	148	1.7
7	140207	31.2	67	36	78	0.7
8	140208	78.0	182	118	363	1.7
9	140220	32.1	80	47	126	2.1
10	140221	66.1	149	90	249	2.3
11	140301	56.6	157	64	177	1.3
12	140306	42.5	100	48	116	1.5

Table 4 (continued). Morphometric properties of Dbx1 neurons in the reticular formation. The entire table consists of 37 columns and 12 rows. Columns 13-17 are shown in this portion of the table. The table will continue on the subsequent pages.

		18	19	20	21	22
Row Number	Reticular Formation Neuron Index	Terminal segments	Average Burke Taper (μm)	Maximum Burke taper (μm)	Average Hillman Taper (μm)	Maximum Hillman Taper (μm)
1	130624	217	0.32	1.16	0.42	0.8
2	130625	418	0.31	0.89	0.46	0.9
3	140109	307	0.15	1.30	0.39	0.9
4	140114	661	0.30	1.67	0.43	0.9
5	140120	163	0.23	0.70	0.49	0.9
6	140124	301	0.23	1.50	0.40	0.8
7	140207	113	0.20	0.83	0.33	0.9
8	140208	549	0.53	3.34	0.51	0.9
9	140220	200	0.43	2.11	0.39	0.8
10	140221	317	0.33	2.15	0.46	0.9
11	140301	231	0.24	1.20	0.38	0.9
12	140306	141	0.40	2.44	0.44	0.9

Table 4 (continued). Morphometric properties of Dbx1 neurons in the reticular formation. The entire table consists of 37 columns and 12 rows. Columns 18-22 are shown in this portion of the table. The table will continue on the subsequent pages.

		23	24	25	26	27
Row Number	Reticular Formation Neuron Index	Average Contraction	Average Daughter Ratio	Average Parent-Daughter Ratio	Average partition asymmetry	Average Rall power
1	130624	0.92	1.2	0.83	0.50	3.1
2	130625	0.91	1.1	0.83	0.43	4.4
3	140109	0.90	1.0	0.89	0.63	0.0
4	140114	0.91	1.2	0.80	0.50	1.3
5	140120	0.95	1.1	0.74	0.50	0.0
6	140124	0.94	1.0	0.89	0.57	0.0
7	140207	0.92	1.1	0.88	0.40	0.0
8	140208	0.88	1.1	0.78	0.38	2.1
9	140220	0.91	1.1	0.84	0.50	3.0
10	140221	0.89	1.3	0.75	0.50	1.4
11	140301	0.92	1.1	0.84	0.50	0.0
12	140306	0.95	1.1	0.76	0.60	3.7

Table 4 (continued). Morphometric properties of Dbx1 neurons in the reticular formation. The entire table consists of 37 columns and 12 rows. Columns 23-27 are shown in this portion of the table. The table will continue on the subsequent pages.

		28	29	30	31	32
Row Number	Reticular Formation Neuron Index	Average Bifurcation amplitude local (°)	Average Bifurcation amplitude remote (°)	Average bifurcation tilt local (°)	Average bifurcation tilt remote (°)	Average bifurcation torque local (°)
1	130624	77.6	43.7	126.3	138.8	180.0
2	130625	60.0	55.9	131.5	130.5	92.7
3	140109	57.7	32.6	125.0	152.2	103.9
4	140114	71.5	63.7	118.4	129.8	115.1
5	140120	73.7	74.4	123.3	116.6	54.0
6	140124	66.2	47.3	134.1	137.1	119.1
7	140207	79.4	43.9	122.0	145.3	70.3
8	140208	59.1	81.5	119.0	115.0	89.2
9	140220	107.0	97.4	95.0	106.4	176.0
10	140221	85.6	95.7	105.9	106.5	76.2
11	140301	71.2	61.8	126.4	132.8	78.8
12	140306	45.2	44.0	145.1	134.2	140.9

Table 4 (continued). Morphometric properties of Dbx1 neurons in the reticular formation. The entire table consists of 37 columns and 12 rows. Columns 28-32 are shown in this portion of the table. The table will continue on the following page.

		33	34	35	36	37
Row Number	Reticular Formation Neuron Index	Average bifurcation torque remote (°)	Average last-parent diameter	Average Diameter threshold	Average Hilmann threshold	Average fractal Diameter
1	130624	125.9	2.6	5.3	5.6	1.1
2	130625	99.4	3.5	3.9	4.3	1.0
3	140109	111.1	2.6	6.2	6.6	1.0
4	140114	106.4	4.9	4.6	5.70	1.0
5	140120	23.7	2.6	9.8	12.7	1.0
6	140124	116.4	3.2	5.8	5.9	1.0
7	140207	35.0	2.4	7.2	7.2	1.0
8	140208	90.2	4.4	8.2	9.1	1.0
9	140220	94.9	3.2	6.8	7.2	1.0
10	140221	63.6	4.0	7.9	8.4	1.0
11	140301	59.0	3.7	6.5	6.6	1.0
12	140306	122.9	2.9	8.0	9.2	1.0

Table 4 (continued). Morphometric properties of Dbx1 neurons in the reticular formation. The entire table consists of 37 columns and 12 rows. Columns 33-37 are shown in this portion of the table.

	PreBötC Average	Reticular Formation Average	U	p
Soma Surface (μm^2)	544.2 \pm 54	758.3 \pm 82.5	77	0.02
Number of Stems	4.3 \pm 0.2	3.7 \pm 0.3	101	0.09
Number of Bifurcations	11.6 \pm 1.3	6.7 \pm 0.7	70.5	0.01
Number of Branches	27.4 \pm 2.8	17.3 \pm 1.5	71.5	0.01
Number of Tips	16.2 \pm 1.4	11.6 \pm 0.8	80	0.02
Width (μm)	470.8 \pm 50.6	172.9 \pm 27.1	21	4E-06
Height (μm)	366.0 \pm 32.5	159.6 \pm 18.7	24	9E-06
Depth (μm)	39.1 \pm 3.1	22.3 \pm 3.1	47.5	5E-04
Average Diameter (μm)	1.3 \pm 0.1	2.8 \pm 0.1	7.5	2E-07
Length (μm)	1766.6 \pm 166.6	628.5 \pm 88.0	20	3E-06
Surface Area (μm^2)	6849.5 \pm 875.0	6759.6 \pm 729.5	124	0.32
Volume (μm^3)	5575.4 \pm 1540.2	14124.3 \pm 1840.6	38	1E-04
Average Euclidean Distance (μm)	141.7 \pm 15.2	57.7 \pm 5.7	13.5	9E-07
Maximum Euclidean Distance (μm)	392.6 \pm 50.6	139.8 \pm 13.4	35	3E-07

Table 5. Mann Whitney U test comparison of morphometric data obtained from L-measure for preBötC and reticular formation neurons. P values <0.05 values are highlighted in yellow

	PreBötC Average			Reticular Formation Average			U	p
Average Path Distance (μm)	194.0	\pm	23.7	70.3	\pm	7.8	19	3E-06
Maximum Path Distance (μm)	537.6	\pm	75.4	179.8	\pm	22.1	16.5	2E-06
Average Branch Order	1.8	\pm	0.1	1.4	\pm	0.2	95.5	0.07
Terminal segments	584.1	\pm	73.7	301.5	\pm	48.2	65	5E-03
Average Burke Taper (μm)	0.1	\pm	0.03	0.3	\pm	0.03	19	3E-05
Maximum Burke taper (μm)	0.9	\pm	0.4	1.6	\pm	0.2	39.5	2E-04
Average Hillman Taper (μm)	0.5	\pm	0.04	0.4	\pm	0.01	93	0.06
Maximum Hillman Taper (μm)	0.9	\pm	0.01	0.9	\pm	0.01	58.5	1E-03
Average Contraction	0.9	\pm	0.01	0.9	\pm	0.01	61.5	3E-03
Average Daughter Ratio	1.2	\pm	0.02	1.1	\pm	0.02	99	0.09
Average Parent-Daughter Ratio	0.8	\pm	0.01	0.8	\pm	0.02	122.5	0.30
Average partition asymmetry	0.5	\pm	0.02	0.5	\pm	0.02	110.5	0.17
Average Rall power	2.4	\pm	0.3	1.6	\pm	0.5	95	0.70

Table 5 (continued). Mann Whitney U test comparison of morphometric data obtained from L-measure for preBötC and reticular formation neurons. P values <0.05 values are highlighted in yellow

	PreBötC Average		Reticular Formation Average		U	p
Average Bifurcation amplitude local (°)	75.6	± 3.4	71.2	± 4.6	123.5	0.31
Average Bifurcation amplitude remote (°)	69.8	± 3.7	61.8	± 6.2	102	0.11
Average bifurcation tilt local (°)	116.4	± 2.7	122.7	± 3.7	101	0.10
Average bifurcation tilt remote (°)	121.6	± 2.8	128.8	± 4.2	97.5	0.08
Average bifurcation torque local (°)	96.5	± 4.8	108.0	± 11.6	123	0.30
Average bifurcation torque remote (°)	86.3	± 3.6	87.4	± 9.9	115	0.21
Average last-parent diameter	1.7	± 0.3	3.3	± 0.2	35.5	8E-05
Average Diameter threshold	2.5	± 0.4	6.7	± 0.5	21	5E-06
Average Hilmann threshold	2.5	± 0.5	7.4	± 0.6	28	2E-05
Average fractal Diameter	1.0	± 0.003	1.0	± 0.003	32.5	3E-05

Table 5 (continued). Mann Whitney U test comparison of morphometric data obtained from L-measure for preBötC and reticular formation neurons. P values <0.05 values are highlighted in yellow

Sholl and branching pattern analysis

Dendritic Sholl analysis results were compared from 0 μm to 500 μm distal from the cell soma in 50 μm increments. Only eight of the analyzed neuron morphologies in the preBötC and three neurons in the reticular formation have dendritic trees extending beyond 500 μm , so a comparison beyond 500 μm would not provide much value. Our Sholl analysis provided data about the number of branch points, total dendritic length, total dendritic volume, and total dendritic surface area for each 50 μm increment.

Branch Points

Branch points are similar for respiratory Dbx1 reticular formation neurons and respiratory Dbx1 preBötC neurons between 0 μm and 50 μm from the soma (Table 6). Between 50 μm and 200 μm from the soma, the Mann Whitney test (Table 6) indicates respiratory Dbx1 preBötC branch points and Dbx1 reticular formation branch points differ. After 300 μm , there were no differences between the respiratory Dbx1 neuron populations. Neither neuron group had branch points beyond 450 μm from the soma. Both groups branch most extensively between 0 μm and 50 μm from the soma; however, the branching in reticular formation neurons drops dramatically beyond 50 μm from the soma while the branching in the preBötC neurons decreases more gradually as the dendritic tree develops further away from the soma (Table 6).

Dendritic Length

Dendritic length is similar among respiratory Dbx1 preBötC neurons and respiratory Dbx1 reticular formation neurons closest to the soma, between 0 μm and 50 μm . Dendritic length becomes disparate between 50 μm and 250 μm (Table 7). The respiratory Dbx1 preBötC neurons have greater average dendritic length than the Dbx1 reticular formation neurons from 50 μm to 400 μm , indicating Dbx1 preBötC neurons have more dendritic fiber in this range. Beyond 400 μm , the two neuron groups are nearly even in dendritic length (Table 7).

Dendritic Volume

Respiratory Dbx1 reticular formation neurons have greater average dendritic volume than respiratory Dbx1 preBötC neurons for each measured increment (Table 8). The two respiratory Dbx1 neuron populations differ significantly for the majority of the dendritic tree, based on the Mann Whitney analysis (Table 8).

Dendritic Surface Area

Respiratory *Dbx1* reticular formation neurons have greater average dendritic surface area than respiratory Dbx1 preBötC neurons for all but one measured increment, between 150 μm and 200 μm from the soma (Table 9).

Differences between the two respiratory Dbx1 neuron populations differed significantly closest to the soma and beyond 250 μm from the soma (Table 9).

Distance from the Soma	PreBötC Branch point average	Reticular Formation Branch point average	Mann Whitney U	p
0 μm - 50 μm	6.0 \pm 0.8	6.8 \pm 0.7	103	0.11
50 μm - 100 μm	2.7 \pm 0.5	0.6 \pm 0.2	52.5	8E-4
100 μm - 150 μm	1.6 \pm 0.5	0.3 \pm 0.1	88	0.03
150 μm - 200 μm	1 \pm 0.3	0.1 \pm 0.1	79.5	0.01
200 μm - 250 μm	0.4 \pm 0.2	0.1 \pm 0.1	112.5	0.10
250 μm - 300 μm	0.4 \pm 0.1	0.1 \pm 0.1	100.5	0.04
300 μm - 350 μm	0.2 \pm 0.1	0.1 \pm 0.1	130.5	0.32
350 μm - 400 μm	0.1 \pm 0.1	0 \pm 0	126	0.15
400 μm - 450 μm	0.1 \pm 0.1	0 \pm 0	132	0.42
450 μm - 500 μm	0 \pm 0	0 \pm 0	138	0.5

Table 6. Sholl analysis branch points data and Mann Whitney U test. Average and standard error given for both respiratory Dbx1 preBötC neurons and respiratory Dbx1 reticular formation neurons. Mann-Whitney U statistic and p value for comparison between respiratory Dbx1 preBötC and respiratory reticular formation neurons. Statistically significant p values ($p < 0.05$) are highlighted in yellow.

Distance from the Soma	PreBötC Dendritic Length (μm)	Reticular Formation Dendritic Length (μm)	Mann Whitney U	p
0 μm - 50 μm	404 \pm 35	393 \pm 32	132	0.42
50 μm - 100 μm	437 \pm 41	171 \pm 44	35	7E-5
100 μm - 150 μm	337 \pm 34	184 \pm 30	56	2E-3
150 μm - 200 μm	253 \pm 32	105 \pm 18	49	6E-4
200 μm - 250 μm	150 \pm 23	71 \pm 11	69.5	8E-3
250 μm - 300 μm	94 \pm 19	77 \pm 13	132.5	0.43
300 μm - 350 μm	76 \pm 17	57 \pm 6	135.5	0.47
350 μm - 400 μm	53 \pm 14	54 \pm 7	114.5	0.21
400 μm - 450 μm	33 \pm 7	45 \pm 9	104	0.12
450 μm - 500 μm	19 \pm 6	37 \pm 9	93	0.06

Table 7. Sholl analysis dendritic length data and Mann Whitney U test. Average and standard error given for both respiratory Dbx1 preBötC neurons and respiratory Dbx1 reticular formation neurons. Mann-Whitney U statistic and p value for comparison between respiratory Dbx1 preBötC and respiratory reticular formation neurons. Statistically significant p values ($p < 0.05$) are highlighted in yellow.

Distance from the Soma	PreBötC Dendritic Volume (μm^3)	Reticular Formation Dendritic Volume (μm^3)	Mann Whitney U	p
0 μm - 50 μm	4666 \pm 939	8447 \pm 1120	51	8E-4
50 μm - 100 μm	651 \pm 137	1108 \pm 181	75	0.01
100 μm - 150 μm	443 \pm 101	604 \pm 110	96	0.07
150 μm - 200 μm	274 \pm 71	307 \pm 63	93	0.06
200 μm - 250 μm	152 \pm 54	210 \pm 35	71.5	0.01
250 μm - 300 μm	97 \pm 36	230 \pm 51	56.5	2E-3
300 μm - 350 μm	53 \pm 17	155 \pm 27	54.5	1E-3
350 μm - 400 μm	39 \pm 17	143 \pm 28	44.5	3E-4
400 μm - 450 μm	23 \pm 10	135 \pm 41	68	6E-3
450 μm - 500 μm	18 \pm 8	101 \pm 34	76	0.01

Table 8. Sholl analysis dendritic volume data and Mann Whitney U test. Average and standard error given for both respiratory Dbx1 preBötC neurons and respiratory Dbx1 reticular formation neurons. Mann-Whitney U statistic and p value for comparison between respiratory Dbx1 preBötC and respiratory reticular formation neurons. Statistically significant p values ($p < 0.05$) are highlighted in yellow.

Distance from the Soma	PreBötC Dendritic Surface Area (μm^2)	Reticular Formation Dendritic Surface Area (μm^2)	Mann Whitney U	p
0 μm - 50 μm	3549 \pm 542	5629 \pm 525	47	4E-4
50 μm - 100 μm	1720 \pm 254	1935 \pm 242	104	0.12
100 μm - 150 μm	1202 \pm 193	1150 \pm 184	135	0.46
150 μm - 200 μm	788 \pm 132	613 \pm 102	130	0.39
200 μm - 250 μm	449 \pm 112	425 \pm 65	95.5	0.07
250 μm - 300 μm	285 \pm 78	459 \pm 86	73.5	0.01
300 μm - 350 μm	187 \pm 47	321 \pm 39	72.5	0.01
350 μm - 400 μm	123 \pm 36	297 \pm 41	50.5	8E-4
400 μm - 450 μm	75 \pm 22	261 \pm 64	69	7E-3
450 μm - 500 μm	57 \pm 21	200 \pm 55	78	0.02

Table 9. Sholl analysis dendritic volume data and Mann Whitney U test. Average and standard error given for respiratory Dbx1 preBötC neurons and respiratory Dbx1 reticular formation neurons. Mann-Whitney U statistic and p value for comparison between respiratory Dbx1 preBötC and respiratory reticular formation neurons. Statistically significant p values ($p < 0.05$) are highlighted in yellow.

DISCUSSION

The preBötC is the kernel of respiratory rhythm generation in mammals (Feldman and Del Negro, 2006; Feldman et al., 2013; Ramirez et al., 2016; Rekling and Feldman, 1998; Richter and Smith, 2014; Smith et al., 1991) and the preBötC has been definitively identified in humans (Schwarzacher et al., 2011). Glutamatergic (excitatory) neurons derived from precursors that express the transcription factor Dbx1 comprise the crucial rhythmogenic population in preBötC (Bouvier et al., 2010; Gray et al., 2010). The preBötC is responsible for generating the inspiratory phase of the respiratory rhythm and projecting to other centers of the brain, such as the reticular formation, to convey respiratory motor output (Wang et al., 2014) and facilitate breathing coordination with other orofacial behaviors (Kleinfeld et al., 2014; Koizumi et al., 2008; Moore et al., 2014).

Three-dimensional digital representations of Dbx1 preBötC and reticular formation neurons offer a considerable amount of geometric information, which we analyze to help unravel the rhythmogenic and premotor nature of these neurons. This morphological study showed that Dbx1 preBötC and reticular formation neurons are similar in a great many aspects of their dendritic trees that have physiological relevance, except for diameter which was significantly different from one population to the other. Also, this study further confirms the prior suggestion that Dbx1 preBötC neurons exhibit contralateral axonal projections (Bouvier et al., 2010; Gray et al., 2010; Pierani et al., 2001; Lanuza et

al., 2004), but surprisingly, only two of the twelve Dbx1 reticular formation neurons project toward the hypoglossal motor nucleus to generate respiratory related motor output, suggesting Dbx1 reticular neurons are involved in additional orofacial behaviors that must function harmoniously with respiration.

Dbx1 reticular formation neurons may have larger passive conductance

Input received via dendrites is attenuated before reaching the soma, which is the nature of cable properties. The way in which electrical signals from the dendrites are combined and influenced by the properties of dendrites is the basis of cable theory (Beierlein, 2014). Cable theory models dendrites as cylinders with separate conductances (resistances) governing flow of passive current across the plasma membrane (which is the radial boundary of the cylinder) and through the cylinder longitudinally. The plasma membrane also has intrinsic capacitance in parallel with membrane resistance.

Membrane resistance, r_m , will be proportional to the membrane area if the passive ion channels are uniformly distributed over that area of membrane; therefore the membrane resistance will be inversely proportional to the area. This relationship is quantified in the equation $r_m = \frac{R_m}{\pi r^2}$ (Beierlein, 2014) where R_m is the specific resistance of the membrane (in units of Ω -cm), r is the radius (in units of cm). The denominator of the equation for input resistance is the area of the dendrite. Specific resistance is defined for a 1-cm² patch of membrane, while

membrane resistance varies based on the diameter and length of the segment of dendrite analyzed.

The data suggest Dbx1 reticular formation neurons have a larger mean diameter, thus a larger radius, than Dbx1 preBötC neurons. In the equation for membrane resistance, r_m , the term for the diameter is on the bottom of the fraction. Therefore, the larger diameter among respiratory *Dbx1* reticular formation neurons will result in a lower membrane resistance. Since resistance and conductance have an inverse relationship, respiratory Dbx1 reticular formation neurons may have a greater conductance than respiratory Dbx1 preBötC neurons if their specific resistance is the same, which is a reasonable assumption since both neuron types are from the same genetic precursors, are located in the respiratory medulla, and are from the same age of mice.

Conductance, measured in Siemens (S), is a measure of how much electric current flows given an applied electromotive force. Thus, a larger conductance means that more current can flow across the membrane, making the neuron more leaky. Note that disparate specific membrane values or the presence of some active membrane properties may affect the conductance such that the difference in diameter does not lead to a distinct difference in conductance.

Six of the analyzed morphometric properties provide information about the relationships between bifurcation nodes and bifurcation planes within the dendritic arbor. Respiratory Dbx1 neurons in the preBötC and the reticular formation are similar in all of these measurements. Similarities in bifurcation amplitude suggest the dendritic trees among respiratory Dbx1 neurons in both

the preBötC and the reticular formation have a similar radial spread. Bifurcation tilt and torque give a sense of how the dendritic tree twists as it progresses away from the soma. Similarities in these bifurcation measurements suggest that the three-dimensional radial spread of the dendrites of respiratory Dbx1 neurons in the preBötC and reticular formation will be similar. The process through which dendrites develop and orient their dendritic trees is not yet completely understood, but neighboring electrical activity, nerve growth factors, and expression of specific genes that govern branching such as *kak* may play a role in dendritic growth and branching (Scott and Luo, 2001). *Kak* may govern microtubules that are involved in branch formation. (Scott and Luo, 2001). Since respiratory Dbx1 preBötC and respiratory Dbx1 reticular formation neurons have similar bifurcation or branching, they may experience similar microtubule activity during development resulting in similar branching properties.

Closest to the soma, between 0 μm and 50 μm , respiratory Dbx1 neurons in the preBötC and reticular formation are similar in number of branch points and dendritic length, but differ in dendritic volume and surface area. This difference is likely attributable to the difference in diameter between the two neuron groups. Reticular formation neurons have a larger dendritic diameter than preBötC neurons and so it follows that their dendritic volume and surface area would be larger. Between 50 μm and 450 μm away from the soma, there is a difference in at least one of the four categories evaluated in the Sholl analysis.

The morphometric data depend on analysis of the digital reconstructions and visual identification of the neuron's location. The rostrocaudal distribution of

Dbx1 neurons is uniform throughout the ventral respiratory column and does not have a region that is visually distinct as the preBötC (Ruangkittisakul et al 2014). The dorsal border of the preBötC is identifiable as it is immediately ventral to the nucleus ambiguus. The dorsal-most Dbx1 preBötC neurons blend into the ventral-most region of the reticular formation. Respiratory Dbx1 neurons are aligned in a continuum in a dorsomedial to ventrolateral manner. Therefore, there may be a few neurons that are designated as being part of the reticular formation where they could in fact be in the dorsal region of the preBötC (Wang et al., 2014). There is not a clear border between preBötC and reticular formation, particularly given that Dbx1 neurons are continuous throughout.

Digital reconstructions are known to be different depending on the way the structure of the neuron is labeled, the type of imaging used to acquire the neuron image, the method of reconstruction, and even the person who transcribes confocal images into the digital reconstructions of morphology. We endeavored to minimize these differences in several ways. We used the same method of labeling for the morphology of all of the reconstructed neurons. While there were two people creating the reconstructions that were analyzed in this study (the vast majority done by me, the author of this dissertation), both used the same software to create the digital reconstructions and used the same software to assemble the microscopy images to use. Also, the reconstruction software that we used, Neuromantic, allows the user to zoom in to the microscopy images up to 16000%, as mentioned in the previous chapter. This considerable amount of zoom makes it easy for the user to determine the details of the microscopy image

in order to make the most accurate reconstruction possible, up to the point of the resolution of the images and their underlying pixels. Respiratory Dbx1 neurons have a simpler morphology than other neuron types such as Purkinje neurons, which have extensively branched dendritic arbors. Some preBötC neurons that express bursting properties in neonatal rats may have spines and protrusions (Koizumi et al., 2013) but Dbx1 preBötC neurons in mice do not have spines or protrusions (Picardo et al., 2013). Spines and protrusions within the dendritic tree would provide another level of complexity in the reconstructions leaving room for greater discrepancy between Dbx1 preBötC and IRT neurons. Also, while respiratory Dbx1 neurons do have branched dendritic trees, their dendritic trees are not heavily branched compared to other common dendritic morphologies such as Purkinje neurons or basket neurons (Okhotin and Kalinichenko, 2002).

There were eleven analyzed neurons that did not have a discernible axon. The neurons with short axons or no axon at all may be making local connections within the preBötC or were not complete axon fills, or the axons were cut off during the slicing procedure. Axons were identified and distinguished from dendrites in several ways, described in the previous chapter. Only neurons with dendritic morphometric properties that had at least 100 μm in height and/or width were considered as part of this study. Neurons with less than 100 μm of dendrite were considered to be incomplete or unsuccessfully filled with biocytin and would not be appropriate to include. We recommend that the reader draw no firm conclusions from the lack of a reconstructed axon because one cannot determine for certain whether the axon was removed by virtue of being cut or it never filled.

Respiratory Dbx1 reticular formation neurons may coordinate breathing with orofacial behaviors

The intermediate reticular formation contains a mixture of premotor neurons including trigeminal premotor neurons, hypoglossal premotor neurons, and vibrissa premotor neurons (Kleinfeld et al., 2014; Stanek et al., 2014). We hypothesized that respiratory modulated Dbx1 neurons in the reticular formation would mainly be hypoglossal premotor neurons as the hypoglossal motor nucleus is a pool of motor neurons that innervates all of the intrinsic muscles of the tongue and four out of five of the extrinsic tongue (Ono et al., 1998). The hypoglossal motor nucleus helps maintain airway patency during respiration via tongue protrusion (Fregosi and Ludlow, 2014).

Only three respiratory modulated Dbx1 neurons in the reticular formation exhibited axon projections toward the hypoglossal nucleus. A larger proportion of Dbx1 reticular formation neurons were commissural than anticipated and did not project toward the hypoglossal motor nucleus. Commissural reticular formation neurons may have a role in coordinating respiration with orofacial behaviors that include phonation, chewing, suckling, licking, and sniffing (Kleinfeld et al., 2014; Moore et al., 2013, 2014). Since whisking or vibrissa premotor neurons are present in the reticular formation, it is possible that these commissural respiratory modulated reticular formation neurons are vibrissa premotor neurons. However, lesions of the vibrissa neurons in the intermediate reticular formation only

affected ipsilateral whisking (Moore et al., 2013) so the contralateral Dbx1 reticular formation neurons may not be vibrissa neurons, but could be involved in inspiratory drive for airway tongue movements or coordination of orofacial behaviors aside from whisking (Ono et al., 1998; Peever et al., 2002)

In summary, the morphometric properties and axon projections of respiratory Dbx1 neurons in the preBötC and reticular formation were evaluated in order to further ascertain their contribution to the respiratory neural network. Respiratory Dbx1 neurons in the preBötC and reticular formation are similar in many dendritic morphometric measurements. However, there was a difference in diameter which may contribute to a greater passive conductance in respiratory Dbx1 reticular formation neurons. Some respiratory Dbx1 reticular formation neurons projected to the ipsilateral hypoglossal motor nucleus, as was expected since we suspected respiratory Dbx1 reticular formation neurons were premotor neurons. More respiratory Dbx1 neurons in the reticular formation were commissural than expected and are thought to coordinate orofacial behaviors with breathing.

CHAPTER 3: Trpc3 and Nav1.6 ion channels in preBötC neurons

INTRODUCTION

Inspiratory breathing rhythm originates in the preBötC of the ventral medulla (Feldman and Del Negro, 2006; Feldman et al., 2013; Smith et al., 1991). Neuroscientists striving to elucidate the cellular-level origins of breathing have determined that Dbx1 preBötC neurons are crucial for respiratory rhythmogenesis (Bouvier et al., 2010; Cui et al., 2016; Gray et al., 2010; Koizumi et al., 2016; Picardo et al., 2013; Vann et al., 2016; Wang et al., 2014). Knowing the site, and that Dbx1-derived neurons are the rhythmogenic cellular substrate, I now turn my attention to the molecular (ion channel) level mechanisms of inspiratory burst- and rhythm generation.

The ion channels that give rise to rhythm-generating whole-cell ion currents have not been identified, and will be investigated in this chapter using principally an anatomical approach. These anatomical experiments are a key step in ultimately testing the roles of these ion channels in respiratory rhythm generation in *in vitro* models of breathing as well as real breathing *in vivo*.

For nearly the past three decades, investigators have suspected two ionic mechanisms may underlie rhythmic network bursts in the preBötC: a voltage sensitive mechanism depending on subthreshold activation of persistent sodium current, I_{NaP} , and a less voltage-sensitive mechanism linked to a non-specific cation current I_{CAN} (Feldman and Del Negro, 2006; Feldman et al., 2013; Ramirez

et al., 2016). In respiratory rhythmogenesis, I_{NaP} has been implicated but without any conclusive demonstration of its putative rhythmogenic role (Ben-Mabrouk and Tryba, 2010; Del Negro et al., 2005, 2010, Pace et al., 2007b, 2007a; Peña et al., 2004; Rubin et al., 2009; Thoby-Brisson and Ramirez, 2001), although for an alternative view of the role of I_{NaP} in rhythmogenesis for inspiration see: (Koizumi and Smith, 2008). On the other hand, I_{CAN} underlies robust inspiratory drive potentials in the preBötC, which are rhythmic bursts driven by network activity and I_{CAN} may itself be rhythmogenic (Crowder et al., 2007; Mironov, 2008; Mironov and Skorova, 2011; Pace and Del Negro, 2008; Pace et al., 2007b; Rubin et al., 2009). Although its putative role in eupnea and inspiratory rhythms *in vitro* is equivocal, I_{NaP} may play a role in the production of robust bursts when respiration is challenged in such cases as anoxia or hypoxia (Paton et al., 2006).

Physiology, simulations, and pharmacology have examined the potential roles of I_{NaP} and I_{CAN} in respiratory rhythm. However, immunohistochemistry is needed to verify the presence of specific ion channels that may give rise to these whole-cell currents. If we can unravel what specific ionophores underlie I_{NaP} and I_{CAN} , then we can design genetic experiments to definitively test their roles in inspiratory rhythm generation and breathing.

Identifying ion channels via immunohistochemistry is notoriously difficult: antibodies react with epitopes found on multiple (genetically distinct) Na^+ channel subunits that share similar protein structure. Moreover, Trp channels have few existing commercial or custom-built antibodies. A great fraction of the work presented in this dissertation was preceded by years of screening and testing

antibodies for effectiveness. That background work was necessary to finalize protocols and thereby provide anatomical evidence for ion channel presence in Dbx1 preBötC neurons to complement our recently published the mRNA transcriptome (Hayes et al., 2017). Note: the presence of mRNA transcripts does not guarantee translation as protein.

Intracellular Ca^{2+} transients have been measured during inspiratory drive potentials, which is consistent with the ability to evoke I_{CAN} during the inspiratory phase (Del Negro et al., 2011). Drive potentials are sensitive to flufenamic acid (FFA), an I_{CAN} antagonist. Ion channels in the Trp family are the leading candidates for mediating I_{CAN} in Dbx1 preBötC neurons because several members of the Trpm and Trpc subfamilies are modulated (usually activated) by intracellular Ca^{2+} and are sensitive to blockade by FFA (Del Negro et al., 2010; Guinamard et al., 2014; Pace et al., 2007b). mRNA for several Trp channels are present in Dbx1 preBötC neurons; in fact, transcriptome data (Hayes et al., 2017) show that Trpc3 is a strong candidate because its mRNA expression is the highest among Trp channels analyzed in Dbx1 preBötC neurons. Since mRNA expression does not guarantee protein translation, I will determine whether Trpc3 ion channel proteins are expressed on Dbx1 preBötC neurons in neonatal and adult mice through immunohistochemistry. Those data would provide direct evidence for a potential ion channel candidate that may mediate I_{CAN} . Trpc3 ion channel expression in Dbx1 preBötC neurons has not been shown before – and such data are scarcely available for any neuron class *in situ* in the nervous

system (Trpc1 and Trpc5 expression in cultured neurons does not constitute the same criteria for *in situ* expression, see (Strübing et al., 2001).

Physiological data demonstrates that the I_{NaP} is ubiquitous in preBötC inspiratory neurons (Del Negro et al., 2002a, 2002b, 2005; Paton et al., 2006; Ptak et al., 2005; Rybak et al., 2003). Despite its being expressed throughout the ventral medulla including, of course, the preBötC the role of I_{NaP} in respiratory rhythm has never been documented convincingly, although a definitive test – by genetically knocking out the underlying ion channel specifically in respiratory rhythmogenic neurons – has yet to be performed. In mice that do not express ion channel $Na_v1.6$ (a genome-wide knockout, not specific to preBötC), I_{NaP} is greatly reduced, although fast (Hodgkin-Huxley-like) and resurgent Na^+ currents are largely unaffected (Osorio et al., 2010). Our mRNA data from Dbx1 and non-Dbx1-derived preBötC neurons (Hayes et al., 2017) also suggests that *Scn8a*, which codes for $Na_v1.6$ channels, is present in Dbx1 and non-Dbx1 neurons, which implicates this channel type as a potential source of I_{NaP} in the preBötC and thus a good target for my studies.

In this chapter, I will examine the expression of $Na_v1.6$ in Dbx1 preBötC neurons and verify the absence of $Na_v1.6$ expression in an intersectional mouse genetic model that enables us to target *Scn8a* knockout to Dbx1 preBötC neurons, the source of the inspiratory rhythm. The specific mouse model intersecting *Dbx1^{Cre}* mice with *Scn8a^{LoxP}* (floxed) reporter mice will be explained in the following methods section and will be used in further physiology experiments and behavioral experiments to examine the effects of $Na_v1.6$

deficiency in Dbx1 preBötC neurons. Verification of the knockout of Nav1.6 is important to validate that any changes, or lack thereof, of breathing behavior in knockout animals are in response to the lack of Nav1.6 ion channels.

METHODS

All of the animal protocols were approved by the Institutional Animal Care and Use Committee at The College of William and Mary, which follows the guidelines provided by the US National Institutes of Health Office of Laboratory Animal Welfare (NIH Office of Laboratory Animal Welfare, 2015).

Trpc3 immunohistochemistry in neonatal mice

Methods involving intersectional mouse genetics, dissection of neonatal tissue, and fixation of neonatal tissue covered in chapter 1 (See Figure 10, Steps 1, 2, and 4) will be the same for Trpc3 immunohistochemistry in neonatal mice. The brainstem and spinal cord were removed and placed in 4% paraformaldehyde (PFA) overnight on an orbital shaker. Brainstem-spinal cords were rinsed in 1X phosphate buffered solution (PBS) (BP399-1, Fisher Scientific, Hampton, NH) for at least 30 minutes after overnight fixation. The brainstem-spinal cords were then suspended in 4% low melting point agar for sectioning with a vibratome (Thermo Scientific Microm HM 650 V, Waltham, MA). Transverse 50- μ m-thick sections were cut from the preBötC region of the

brainstem. Neonatal sections were incubated with 20% normal donkey serum (50-413-367, Fisher Scientific) overnight at 4°C on an orbital shaker. The following day, the slices were washed with 1X PBS 2 x 30 min and were incubated in 1:500 rabbit anti- Trpc3 antibody (ACC-016, Alomone labs, Jerusalem, Israel) solution with 0.4% TritonX-100 overnight at 4°C on an orbital shaker. Sections were then washed 4 x 30 minutes with 1X PBS and placed in 1:200 donkey anti-rabbit Alexa 405 (711-475-152 Jackson ImmunoResearch Labs, West Grove, PA) for one hour. After washing for a minimum of 6 x 30 min with 1X PBS, sections were mounted on glass slides and cover-slipped with Vectashield hardset mounting medium (H-1500; Vector Laboratories, Burlingame, CA). Images were acquired with a 10x air (NA = 0.45) and 60x oil immersion (NA = 1.49) objectives on a Nikon A1R confocal laser scanning microscope using NIS Elements AR imaging software (Nikon Instruments Inc., Melville, NY).

Trpc3 immunohistochemistry in adult mice

To perform Trpc3 immunohistochemistry experiments in adult mice, neonatal *Dbx1^{CreERT2}; Rosa^{26tdTomato}* mice were aged for a minimum of 6 weeks. These adult mice were anesthetized by pentobarbital (100 mg·kg⁻¹), and then transcardially perfused with 1X PBS followed by 4% PFA. The brainstem and spinal cord were removed and placed in 4% PFA overnight at 4°C to complete fixation. Brainstem-spinal cord preparations were rinsed in 1X PBS, placed in 4%

low melting point agar, and sectioned at 50 μm in the same way as the neonatal tissue. The adult medullary slices were incubated in 1:400 rabbit anti- Trpc3 antibody (ACC-016, Alomone labs) solution with 0.4% TritonX-100 overnight at 4°C on an orbital shaker. Sections were then washed 2 x 30 minutes with 0.4% TritonX-100 1X PBS and incubated in 20% normal donkey serum with 0.4% TritonX-100 for 60-90 minutes on an orbital shaker at room temperature. Next, the sections were washed 2 x 10 minutes with 1X PBS and placed in 1:100 donkey anti-rabbit Alexa 405 (711-475-152 Jackson ImmunoResearch Labs) with 0.4% TritonX-100 for one hour. After washing for a minimum of 6 x 30 min with 0.4% TritonX-100, sections were mounted on glass slides and cover-slipped with Vectashield hardset mounting medium. Images were acquired with a 10x air (NA = 0.45) and 60x oil immersion (NA = 1.49) objectives on a Nikon A1R confocal laser scanning microscope using NIS Elements AR imaging software (Nikon Instruments Inc.).

Nav1.6 immunohistochemistry in neonatal mice

To perform Nav1.6 immunohistochemistry, mice with the potential for a genetic knockout of the *Scn8a* gene were bred using the following strategy, which begins with three strains of mice. The first mouse strain is a homozygous *Dbx1^{CreERT2}* mouse as described in Chapter 1. Since there are no alterations to the *Scn8a* gene or the *Rosa26* gene locus, this mouse can be denoted as *Dbx1^{Cre/Cre};Scn8a^{+/+};Rosa26^{+/+}*, where a + indicates a wild type allele. The

second mouse strain, also described in Chapter 1, is homozygous for floxed tdTomato and can be denoted as $Dbx1^{+/+};Scn8a^{+/+};Rosa26^{FtdT/FtdT}$, where FtdT indicates a tdTomato allele preceded by a LoxP-flanked STOP codon. The third mouse strain has LoxP sites flanking exon 1 of *Scn8a* and is denoted as $Dbx1^{+/+};Scn8a^{Flx/Flx};Rosa26^{+/+}$, where Flx indicated the floxed allele. In the first generation of the breeding strategy $Dbx1^{Cre/Cre};Scn8a^{+/+};Rosa26^{+/+}$ are crossed with $Dbx1^{+/+};Scn8a^{+/+};Rosa26^{FtdT/FtdT}$ mice to produce $Dbx1^{Cre/+};Scn8a^{+/+};Rosa26^{FtdT/+}$ mice. In the second generation, $Dbx1^{Cre/+};Scn8a^{+/+};Rosa26^{FtdT/+}$ mice are crossed with $Dbx1^{+/+};Scn8a^{Flx/Flx};Rosa26^{+/+}$, which produces 4 types of offspring: $Dbx1^{Cre/+};Scn8a^{Flx/+};Rosa26^{FtdT/+}$, $Dbx1^{Cre/+};Scn8a^{Flx/+};Rosa26^{+/+}$, $Dbx1^{+/+};Scn8a^{Flx/+};Rosa26^{FtdT/+}$, and $Dbx1^{+/+};Scn8a^{Flx/+};Rosa26^{+/+}$. The offspring of interest from this generation, $Dbx1^{Cre/+};Scn8a^{Flx/+};Rosa26^{FtdT/+}$, were mated and given tamoxifen at embryonic day 10.5 to produce 64 different combinations of genetic offspring resulting in 4 phenotypes. To simplify the genetic combinations, x will represent a mutant or wild type allele (e.g., $Dbx1^{Cre/x}$ would stand for both $Dbx1^{Cre/Cre}$ and $Dbx1^{Cre/+}$). 44% of the offspring are $Dbx1^{x/x};Scn8^{x/x};Rosa26^{x/x}$ and would not be useful for analysis. 28% of the offspring are $Dbx1^{Cre/x};Scn8a^{-/+};Rosa26^{TdT/x}$, signifying a heterozygous knockout of the *Scn8a* gene. 14% of the offspring are $Dbx1^{Cre/x};Scn8a^{+/+};Rosa26^{TdT/x}$, which will express tdTomato but do not have a genetic knockout of *Scn8a*. Finally, 14% of the offspring are $Dbx1^{Cre/x};Scn8a^{-/-};Rosa26^{TdT/x}$ which results in a genetic knockout of one exon (specifically exon 1) of the *Scn8a* gene. Only

Dbx1^{Cre/x};Scn8a^{x/x};Rosa26^{TdT/x} mice were used for immunohistochemistry experiments. Tails from the neonates were genotyped and a section of the spinal cord was used to perform polymerase chain reaction (PCR) fragment analysis to further verify the knockout of the *Scn8a* gene. Immunohistochemistry was performed on third generation offspring dissected and prepared in the same manner described in Chapter 1 (See Figure 10, Steps 2 and 4).

Brainstem-spinal cords were removed and placed in 4% PFA overnight and rinsed in PBS for at least 30 minutes after overnight fixation. The brainstem-spinal cords were then placed in 4% low melting point agar for sectioning with a vibratome (Thermo Scientific Microm HM 650 V). Transverse 50 to 60- μ m-thick sections were cut from the preBötC region of the brainstem. Two different protocols for antibody staining were used. In the first method, sections were incubated with 20% normal donkey serum (50-413-367, Fisher Scientific) overnight at 4°C on an orbital shaker. The slices were subsequently washed with PBS for one hour and were incubated in 1:5000 rabbit anti- Nav1.6 polyclonal antibody (ASC-009, Alomone labs) solution with 0.4% TritonX-100 overnight at 4°C on an orbital shaker. Sections were then washed 4 x 30 minutes with 1X PBS then placed in 1:1000 donkey anti-rabbit Alexa 405 (711-475-152 Jackson ImmunoResearch Labs) for one hour. After washing for a minimum of 6 x 30 min with 0.4% TritonX-100, sections were mounted on glass slides and cover-slipped with Vectashield hardset mounting medium (H-1500; Vector Laboratories).

For the second protocol, sections were incubated with 20% normal donkey serum (50-413-367, Fisher Scientific) and 10% donkey anti-mouse Fab fragment antibody (715-007-003) overnight at 4°C on an orbital shaker. In a separate tube, 1:1000 mouse anti- Nav1.6 monoclonal antibody (K87A/10, Antibodies Incorporated, Davis, CA) was combined with 1:500 donkey anti-mouse Alexa 647 (711-607-003 Jackson ImmunoResearch Labs) for 90 minutes on an orbital shaker to make an antibody complex. Next, 200-400 µL of normal mouse serum was added to the tube and placed on the orbital shaker for an additional 2 hours to remove any secondary antibody that had not bound to the primary antibody. Slices previously incubated with donkey serum and mouse Fab fragments were then incubated in the antibody complex solution overnight. After washing for a minimum of 8 x 30 min with PBS, sections were mounted on glass slides and cover-slipped with Vectashield hardset mounting medium (H-1500; Vector Laboratories).

Images for all Nav1.6 immunohistochemistry experiments were acquired with a 10x air (NA = 0.45) and 60x oil immersion (NA = 1.49) objectives on a Nikon A1R confocal laser scanning microscope using NIS Elements AR imaging software (Nikon Instruments Inc.). Note that Nav1.6 immunohistochemistry was not performed in adult animals because we have no reason *a priori* to suspect that Na⁺ channel expression changes with development and because the triple transgenic intersectional mice are so difficult to breed in sufficient numbers that we cannot reasonably accomplish adult and neonatal anatomical experiments. We opted for neonatal experiments because these animals can be used for *in*

vivo and in vitro experiments and thus provide an advantageous complement to physiological experimentation on the role of I_{NaP} , i.e., Nav1.6 (Hayes, 2017; Hayes, Dermer, Barnett, Hunt, Del Negro, 2017 (in preparation)).

RESULTS

Trpc3 ion channel expression in neonatal mice

To study Trpc3 ion channel expression in neurons of the preBötC, I used brainstem slices from neonatal and adult *Dbx1^{Cre/x};Scn8a^{x/x};Rosa26^{TdT/x}* mice. I found that Trpc3 ion channels are expressed in Dbx1 and non-Dbx1 preBötC neurons in both adult and neonatal mice, demonstrated in Figures 33 and 34. Glial cells are also labeled with tdTomato during Cre-lox recombination and tamoxifen-induced expression of tdTomato to label Dbx1 preBötC neurons, but glia can be distinguished from neurons as they are smaller in size (Kottick et al., 2017). I observed, as expected, that glial cells do not express Trpc3 ion channels.

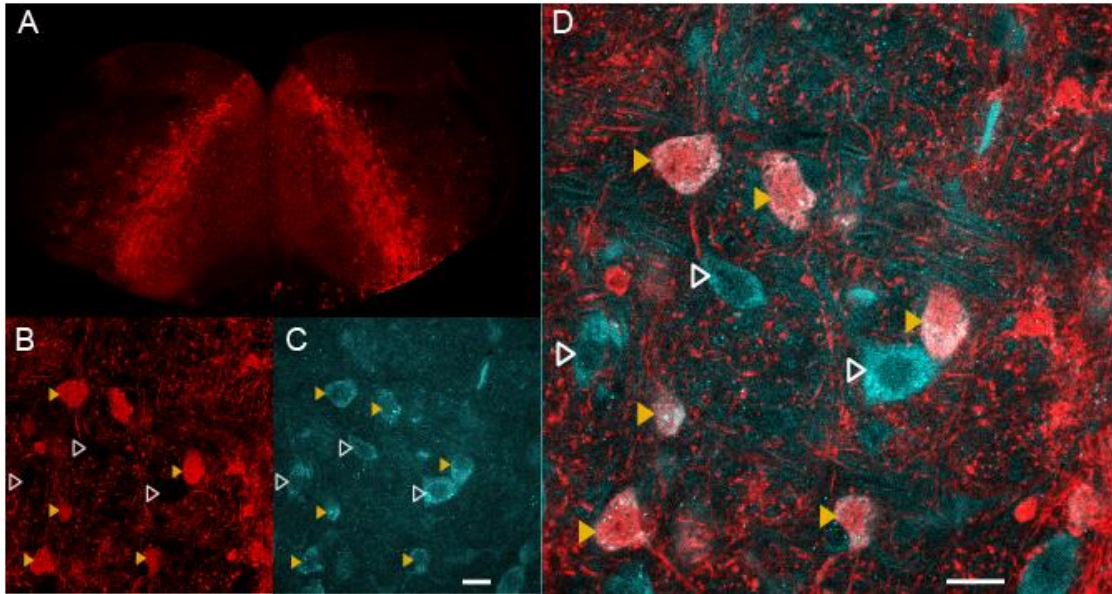


Figure 33. *Trpc3* expression in *Dbx1* and non-*Dbx1* preBötC neurons of adult mice. A, image of the slice demonstrating the immunohistochemistry was performed at the level of the preBötC. B, immunohistochemistry against *Trpc3*. C, tdTomato labeling of *Dbx1* neurons. D, composite of B and C. Filled yellow arrowheads indicate examples of co-localization of *Dbx1* tdTomato preBötC neurons and *Trpc3*. White triangles indicate examples of non-*Dbx1* neurons that express *Trpc3*. Scale bars in both C and D are 20 μm .

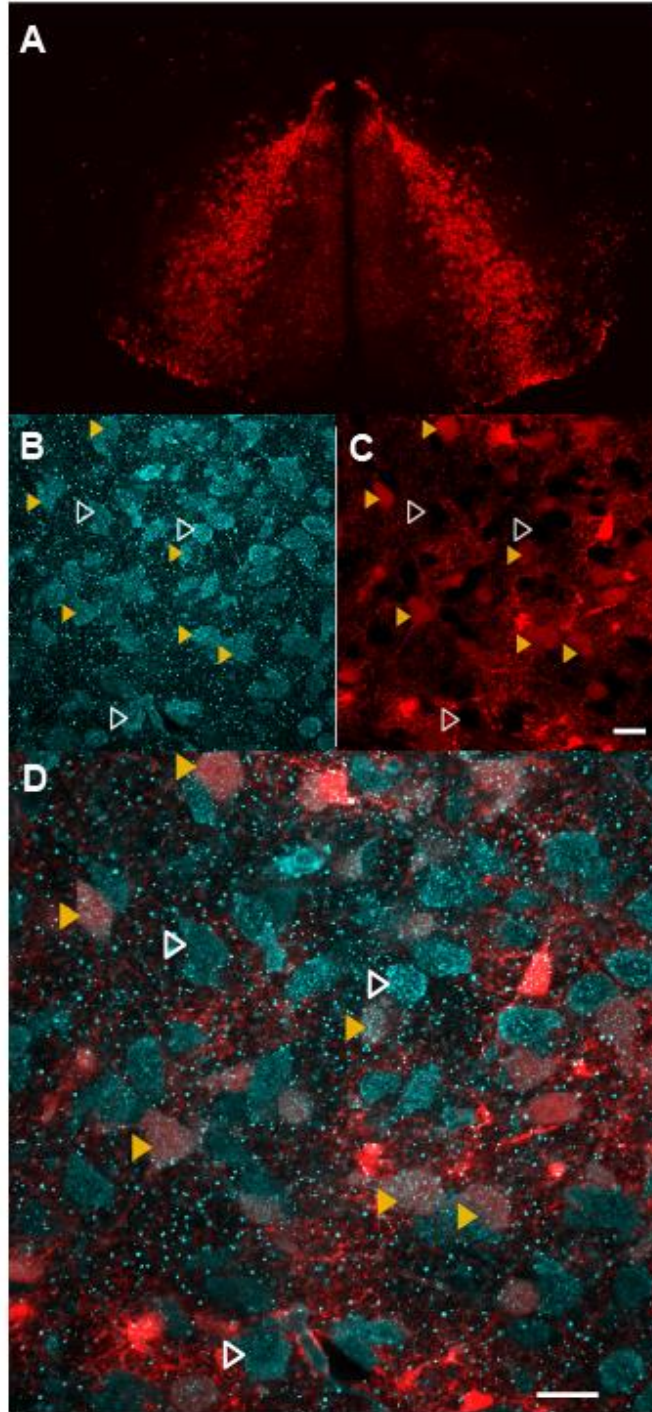


Figure 34. *Trpc3* expression in *Dbx1* and non-*Dbx1* preBötC neurons of neonatal mice. A, image of the slice showing the immunohistochemistry was performed at the level of the preBötC. B, immunohistochemistry against *Trpc3*. C, tdTomato labeling of *Dbx1* neurons. D, composite of B and C. Filled yellow arrowheads indicate examples of co-localization of *Dbx1* tdTomato preBötC neurons and *Trpc3*. White triangles indicate examples of non-*Dbx1* neurons that express *Trpc3*. Scale bars in both C and D are 20 μm .

Nav1.6 ion channel expression in neonatal mice

To study Nav1.6 ion channel expression in key neurons of the preBötC, we used brainstem slices from neonatal *Dbx1^{Cre/x};Scn8a^{x/x};Rosa26^{TdT/x}* mice. We found that Nav_v1.6 ion channels are ubiquitously expressed in both Dbx1 and non-Dbx1 preBötC neurons in mice, demonstrated in Figures 35 and 36. Glial cells do not express Nav_v1.6 ion channels.

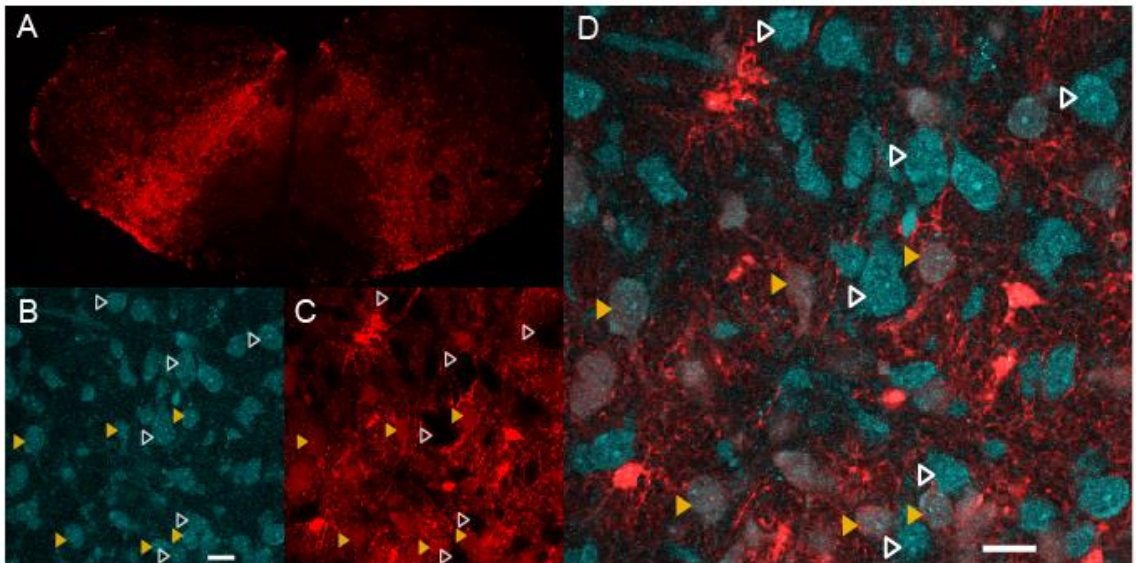


Figure 35. Nav_v1.6 monoclonal immunohistochemistry in neonatal mice. A, image of the slice showing the immunohistochemistry was performed at the level of the preBötC. B, immunohistochemistry against Nav_v1.6. C, tdTomato labeling of Dbx1 neurons. D, composite of B and C. Filled yellow arrowheads indicate examples of co-localization of Dbx1 tdTomato preBötC neurons and Nav_v1.6. White triangles indicate examples of non-Dbx1 neurons that express Nav_v1.6. Scale bars in both C and D are 20 μm.

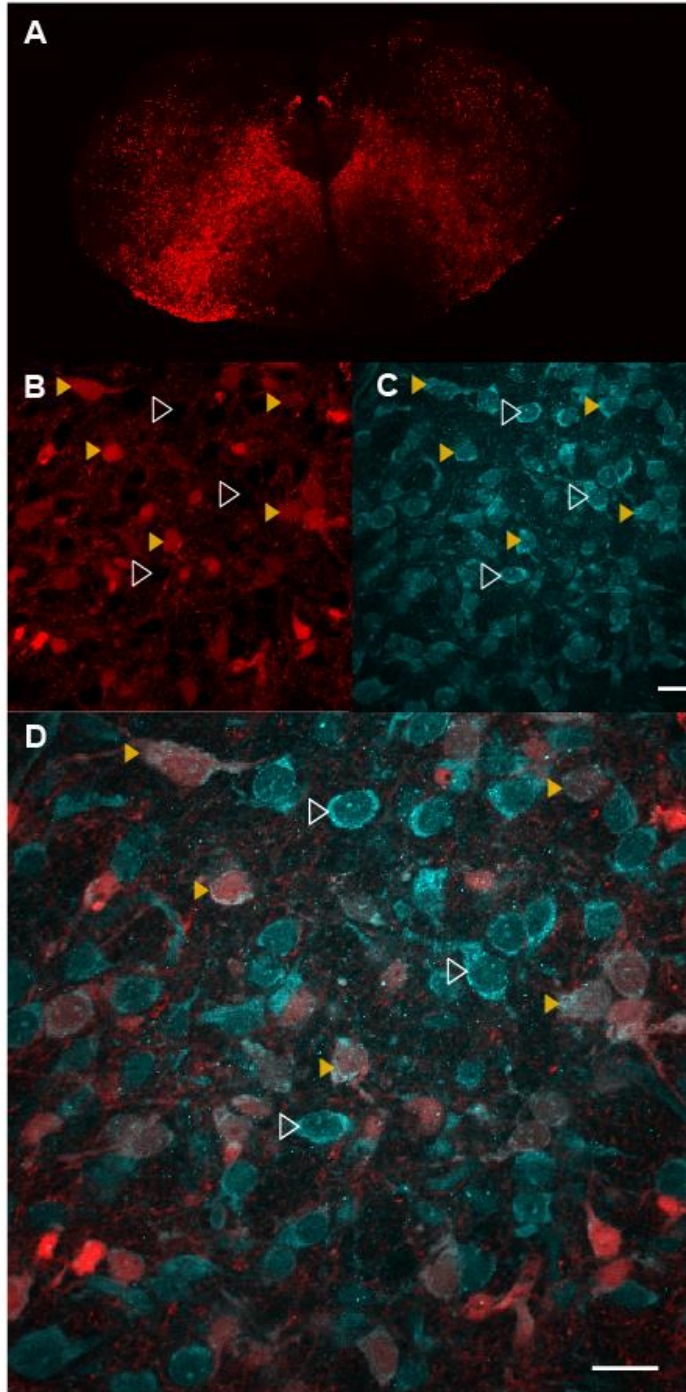


Figure 36. $\text{Na}_v1.6$ polyclonal immunohistochemistry in neonatal mice. A, image of the slice showing the immunohistochemistry was performed at the level of the preBötC. B, immunohistochemistry against $\text{Na}_v1.6$. C, tdTomato labeling of Dbx1 neurons. D, composite of B and C. Filled yellow arrowheads indicate examples of co-localization of Dbx1 tdTomato preBötC neurons and $\text{Na}_v1.6$. White triangles indicate examples of non-Dbx1 neurons that express $\text{Na}_v1.6$. Scale bars in both C and D are 20 μm .

DISCUSSION

Trpc3 ion channels may be involved in the generation of I_{CAN}

Members of the Trp superfamily of ion channels likely contribute to I_{CAN} , as characterized in preBötC neurons (Crowder et al., 2007; Mironov, 2008; Mironov and Skorova, 2011; Pace and Del Negro, 2008; Thoby-Brisson and Ramirez, 2001). Among Trp channel mRNA analyzed in Dbx1 preBötC neurons, *Trpc3* mRNA had the highest expression among Trp mRNA family members in the preBötC, as demonstrated in Figure 5 of the literature review and (Hayes et al., 2017). Through immunohistochemistry, I revealed the presence of Trpc3 ion channels in Dbx1 neurons, exhibited in Figures 33 and 34. These figures also show the presence of Trpc3 ion channels in non-Dbx1 preBötC neurons, which indicates that this channel is expressed by rhythmogenic (Dbx1) neurons as well as non-rhythmogenic (non-Dbx1) neurons that are part of the pattern-generating respiratory circuitry.

Trpc3 has been proposed to contribute to I_{CAN} in preBötC neurons (Ben-Mabrouk and Tryba, 2010), although the evidence in that study is relatively weak considering that the authors showed relatively low resolution western blot analyses and used promiscuous pharmacology. Nevertheless, Trpc3 channels are known to be sensitive to intracellular Ca^{2+} concentration and conduct monovalent cations (Trebak et al., 2003). If this is the case, we would expect Dbx1 neurons to express Trpc3. I found that Trpc3 is expressed ubiquitously in

both Dbx1 and non-Dbx1 preBötC neurons. Given this widespread expression, it is plausible that Trpc3 works in conjunction with other Trp ion channel subunits to mediate I_{CAN} and contribute to the inspiratory bursts and rhythm.

Trpc3 ion channels may play a role in mechanisms other than respiratory rhythm generation

Ubiquitous expression of Trpc3 may indicate that Trpc3 ion channels are involved in other cellular mechanisms in addition to respiratory rhythm generation including simple cellular functions and cellular survival. Trpc channels may be important for signal transduction and axon guidance during brain development (Li et al., 2005). The development of functional neuronal circuits requires the finely tuned growth of nerve fibers toward their targets, a process called nerve pathfinding (Cui and Yuan, 2007; Goodman and Shatz, 1993). It is plausible that Trpc3, being a member of the Trpc family, is involved with the development of neuronal circuits and the growth of nerve fibers as well as having a role in the I_{CAN} current; it is also possible that Trpc3 is mainly important for development and pathfinding and has a minimal role in respiratory rhythm generation.

Trpc3 is also involved in motor control, specifically coordination which is a function of the cerebellum. There, Trpc3 channels operate in conjunction with metabotropic glutamate receptor (mGluR) signaling in mouse Purkinje cells (Hartmann et al., 2008). Group 1 mGluRs regulate slow synaptic excitation; without Trpc3, mice had no slow excitatory post synaptic currents (EPSC) or

mGluR mediated currents. I_{CAN} gated in part by group 1 mGluR signaling are important for respiratory burst generation and respiratory rhythm (Pace et al., 2007b). Group 1 mGluRs are coupled through phospholipase C to inositol triphosphate (IP_3) synthesis, which evokes intracellular Ca^{2+} release, thus serving as a potential source of I_{CAN} activation (Pace et al., 2007b). Trpc3 ion channels present on Dbx1 neurons in both neonatal and adult mice may mediate group 1 mGluR-mediated I_{CAN} activation, thus contributing to inspiratory burst generation.

Na_v1.6 ion channels may be involved in I_{NaP} generation

Between 5 and 25% of preBötC neurons in neonatal mice exhibit voltage-dependent conditional bursting properties *in vitro*, often called *bursting-pacemaker* activity (Del Negro et al., 2005; Koizumi and Smith, 2008; Peña et al., 2004). At the time the preBötC was discovered in 1991 (Smith et al. Science 1991) the voltage-dependent bursting-pacemaker neurons were hypothesized to be rhythmogenic. Most studies to test that idea (i.e., the pacemaker hypothesis) have approached it via pharmacology. Our lab, and our collaborators, have concluded that voltage-dependent pacemaker activity is not required for respiratory rhythm generation because rhythmogenesis still occurs when voltage-dependent bursting behavior is precluded in preBötC neurons (Del Negro et al., 2002b). Rhythm continued and indeed respiratory motor output frequency was unaffected by bath application of blockade of I_{NaP} (Del Negro et al., 2005). Those experiments utilized the drug riluzole, which blocks I_{NaP} (Doble, 1996; Urbani and

Belluzzi, 2000). However, not every group obtained the same results. In thin (250-350 μm) neonatal rat slices and preBötC explants, experiments blocking I_{NaP} with riluzole and tetrodotoxin (TTX) do stop the rhythm (Koizumi and Smith, 2008), but not in in situ or in vivo preparations (Paton et al., 2006; Smith et al., 2007). Furthermore, when similar experimental methods were applied to thicker neonatal mouse slices (500-550 μm) containing the preBötC and surrounding network components such the rostral ventral respiratory group (rVRG), the respiratory rhythm was not disrupted (Pace et al., 2007a). I_{NaP} increases spiking frequency, but has not been shown to contribute to respiratory drive potentials (Morgado-Valle et al., 2008; Pace et al., 2007a).

The disparities in respiratory rhythm cessation could be due to the pharmacological properties of riluzole and differences in experimental design. Riluzole depresses neuronal excitability, thus when added to a slice via direct injection in the preBötC, the force of the injection can cause a channel to form in the tissue allowing riluzole to travel to other nearby areas of the slice such as the raphe obscurus. Serotonergic raphe neurons the preBötC help maintain rhythmic preBötC function (Peña and Ramirez, 2002; Tryba et al., 2006), so a loss in excitability in the raphe would disrupt rhythmogenesis. The narrative above recounts more than a decade of disagreement and discord because of the promiscuous pharmacology of riluzole, which blocks I_{NaP} but has attendant side effects that never lead to a 'clean' interpretation of experimental results. The convoluted nature of the experimental results is confusing and had led us to

search for a specific ion channel (and its gene) to perform an unambiguous test of the putative role for I_{NaP} in respiratory rhythm generation and breathing.

We would expect Dbx1 preBötC neurons to express ion channels that give rise to I_{NaP} . Sodium channel Nav1.6, derived from the gene *Scn8a*, is the leading candidate Nav1.6 because blockade of Nav1.6 ion channels abolishes I_{NaP} while transient Na⁺ currents are unaffected (Osorio et al., 2010; Raman and Bean, 1997). Through immunohistochemistry, I revealed the presence of Nav1.6 ion channels in Dbx1 neurons, exhibited in Figures 35-36. These figures also show the presence of Nav1.6 ion channels in non-Dbx1 preBötC neurons.

I performed numerous experiments to perfect immunohistochemistry techniques on neonatal mice and subsequently perform immunohistochemistry for Nav1.6 ion channels on *Dbx1^{Cre/x};Scn8a^{x/x};Rosa26^{TdT/x}* mice.

Immunohistochemistry experiments on neonatal tissue are known to present more of a challenge than immunohistochemistry on adult tissue but necessary to understand breathing behaviors at early postnatal stages. I began working with a polyclonal antibody published in knockout experiments similar to our goals (Osorio et al., 2010). Polyclonal antibodies increase the likelihood of having a successful experiment because they recognize multiple epitopes of an antigen, thus offering more robust detection. However, when genotyping tails corresponding to mice used for immunohistochemistry experiments, I learned that the polyclonal antibody was continuing to label Nav1.6 ion channels in the *Dbx1^{Cre/x};Scn8a^{-/-};Rosa26^{TdT/x}* knockout mice. This unexpected result can be attributed to the properties of polyclonal antibodies; polyclonal antibody serum

will contain a mixture of antibody subtypes with different affinities and the ability to detect multiple epitopes and fragments of epitopes (Pohanka, 2009). While polyclonal antibodies have their advantages, it was clear I needed to use a more specific monoclonal antibody to appropriately label *Dbx1^{Cre/x};Scn8a^{-/-};Rosa26^{TdTx}*. Monoclonal antibodies recognize only one epitope of an antigen, thus making them more specific than polyclonal antibodies. I have since chosen an appropriate monoclonal antibody against Nav1.6, but at the time of this writing I am still working to perform immunohistochemistry on a *Dbx1^{Cre/x};Scn8a^{-/-};Rosa26^{TdTx}* mouse. The images in the results were from mice that did not have a complete *Scn8a* knockout. I expect I will be able to obtain these results as soon as possible. Nevertheless, the present lack of knockout data does not affect the goal of determining whether Nav1.6 ion channels are expressed in Dbx1 preBötC neurons and provide a viable target for future physiology experiments.

In this chapter, I show Dbx1 and non-Dbx1 preBötC neurons express both Nav1.6 and Trpc3 ion channels that mediate I_{NaP} and I_{CAN} respectively. This advance in knowledge can be used to help design targeted experiments to knock down these channels and further explore their role in respiratory rhythm generation and real breathing.

CHAPTER 4: Cellular mechanisms underlying sighs and the potential roles of preBötC neurons and glia

INTRODUCTION

Sighs were once thought to be a reflex caused by hypo-inflation of the lungs, but a study in 1993 suggested that sighs are produced by a centrally mediated mechanism because respiratory rhythmogenic neurons change discharge patterns during sighs (Orem and Trotter, 1993). A few years later, experimental data obtain *in vitro*, using mouse slice preparations, demonstrated that the preBötC can generate inspiratory breathing rhythms as well as other fictive breathing-related behaviors including sighs and gasps (Lieske, 2000; Ruangkittisakul et al., 2008). Note, that those data *in vitro* do not preclude the importance of other brainstem or higher brain centers in regulating breathing-related sighs and gasps. Rather, those *in vitro* data showed that an isolated preBötC can generate the rudiments of those behaviors *in vitro*. Furthermore, the rate of fictive sighs can be modulated by changes in blood gases, especially during hypoxia (Lieske et. al., 2000). Sighs also act as a psychophysiological mechanism that resets eupneic breathing after behaviors characterized by periods of high variability such as speech and laughter (Li and Yackle, 2017; Li et al., 2016; Ramirez, 2014, 2017; Vlemincx et al., 2010).

Sighs are longer, deeper inspiratory breaths that are necessary for proper lung function (Cherniack et al., 1981; Ferris and Pollard, 1960; Koch et al., 2013). Sighs expand the lung beyond tidal volume (i.e., the normal volume traversed

during ordinary inspiratory breaths), which occurs periodically to diminish the surface tension within alveoli that can otherwise lead to alveolar collapse.

Alveolar collapse must be avoided because it would preclude gas exchange, the essential function of lung ventilation. Therefore, periodic sighs are important to maintain normal lung function.

Sighs are coupled to emotional responses such as relief and sadness and are often generated when a mammal is transitioning between wakefulness to non-REM sleep and when transitioning between from sleep to arousal (Li and Yackle, 2017; Ramirez, 2014). Malfunctions associated with sighs may be drivers for some diseases including sudden infant death syndrome (SIDS) (Franco et al., 2003; Kahn et al., 1988) and panic disorders (Abelson et al., 2001). With SIDS, victims experience a decrease in spontaneous and induced arousals during sleep (Groswasser et al., 2001; Kahn et al., 1992) and as previously stated the sigh mechanism has a role in successfully transitioning between sleep and arousal. With panic disorders, the affected experience an increase in hyperventilation and breathing variability that persists even when panic itself is pharmacologically controlled (Abelson et al., 2001, 2008). Having a clearer picture of the sigh signaling pathways in the brain may lead to a better targeted approach for disease therapies as well as contribute to our overall understanding of how the brain and CNS generate and control the full range of breathing behaviors, which includes eupnea and sighs all the time in physiologically normal conditions, and sometimes gasps in non-physiological environments with low oxygen availability.

The neuropeptide bombesin, found in frogs, can influence sighs in a range of rodents too (Niewoehner et al., 1983; Ramirez, 2014). Neurons sending signals that evoke sighs are thought to be located in the retrotrapezoid nucleus/parafacial respiratory group (RTN/pFRG) (Li et al., 2016). A subset of neurons in the RTN/pFRG of mice express bombesin-like peptides neuromedin B (NMB) and gastrin releasing peptide (GRP). Microinjection of NMB into the preBötC of anaesthetized rats increased sighs from an average *in vivo* basal sigh rate of 44 sighs/hour up to 858 sighs/hour (Li et al., 2016). Analogously, microinjection of GRP into the preBötC of anaesthetized rats increased sighs from the basal sigh rate up to 643 sighs/hour (Li et al., 2016). Bilateral injection of NMB receptor (NMBR) antagonist BIM23042, or the GRP receptor (GRPR) antagonist RC3095, in anaesthetized wild type rats transiently reduced sighs by 50% in both cases, and in both cases eupnea remained unperturbed (Li et al., 2016).

In transgenic knockout mice lacking NMBRs, the sigh rate is reduced from the *in vivo* wild type average basal sigh rate of 40 sighs/hour to an average of 29 sighs/hour while eupnea is unaffected. Comparably, in transgenic knockout mice lacking GRPRs the sigh rate is reduced to half of the wild type basal sigh rate without any change in eupnea (Li et al., 2016).

In vitro application of NMB onto rhythmically active neonatal mouse brainstem slices containing the preBötC doubled the frequency of fictive sighs (~0.01 Hz); likewise, introducing GRP onto mouse brainstem slices containing the preBötC nearly doubles the rate of fictive sighs (1.7 fold increase) suggesting

GRP and NMB receptors are contained within slices encompassing the preBötC (Li et al., 2016). Neither NMBR null mice nor pharmacological inhibition of NMBRs extinguishes sighs completely, which can be explained by the fact that two different peptidergic systems, NMB- and GRP-mediated, modulate the sigh rhythm (Li et al., 2016).

Additionally, tracing the projections of NMB-expressing and GRP-expressing RTN/pFRG neurons (through transgenic co-expression of NMB or GRP with GFP) in neonatal mice showed that these peptidergic neurons project axons to somatostatin-expressing cells within the preBötC. However, whether those cells in the preBötC were neurons or glia was not addressed directly; the published data and extended data in that study do not resolve their identity (Li et al., 2016). Collectively, these data suggest the presence of NMB and GRP receptors that potently modulate sighs – without affecting eupnea – within the preBötC, but the cellular mechanisms remain unidentified. If *Nmb*-expressing and *Grp*-expressing neurons do project to the preBötC, then neurons or glia in the preBötC should express NMB and GRP receptors; this hypothesis which will be tested in this dissertation chapter.

The reason several have speculated on the role of glia (e.g., (Dashevskiy et al., 2016; Ramirez, 2017)) is that sighs in intact animals, and sigh rhythms *in vitro*, occur at frequencies at least one order of magnitude slower than eupnea in intact animals, as well as inspiratory rhythms measured in breathing models *in vitro*. Recent evidence suggests that glia in the preBötC may play an instrumental role in sigh generation. Bath application of glial toxin eliminated

sighs without terminating eupnea (Dashevskiy et al., 2016). It is hypothesized that the release of astrocytic ATP is important for sigh generation (Dashevskiy et al., 2016). If this is the case, preBötC glial cells may express NMB or GRP receptors, a hypothesis which will also be tested in this dissertation chapter. Analogous to the motivation behind the research presented in the prior chapter, anatomical evidence for peptide receptors on preBötC neurons or glia will lead directly to physiological experiments to test their role(s) in sigh generation in living animals, which will enhance our understanding of respiratory physiology in humans and all terrestrial mammals.

METHODS

All of the animal protocols were approved by the Institutional Animal Care and Use Committee at The College of William and Mary, which follows the guidelines provided by the US National Institutes of Health Office of Laboratory Animal Welfare (NIH Office of Laboratory Animal Welfare, 2015).

NMBR and GRPR immunohistochemistry

Dbx1^{CreERT2}; Rosa26^{tdTomato} mice were used for both neonatal and adult experiments. Methods involving mouse genetics, and dissection of neonatal tissue, and fixation of neonatal tissue covered in chapter 1 (See Figure 10, Steps 1, 2, and 4) will be the same for NMBR and GRPR neonatal

immunohistochemistry. Additionally, fixation of neonatal brainstem-spinal cord preparations, transcardial perfusion of adult mice and subsequent fixation were performed in the same manner as described in chapter 3. Brainstem-spinal cord preparations were rinsed in 1X phosphate buffered solution (PBS) (BP399-1, Fisher Scientific, Hampton, NH) for at least 30 minutes after overnight fixation. The brainstem-spinal cord preparations were then placed in 4% low melting point agar for sectioning with a vibratome (Thermo Scientific Microm HM 650 V, Waltham, MA). Transverse 50-60 μm sections were cut from the preBötC region of the brainstem. Neonatal sections were incubated with 20% normal donkey serum (50-413-367, Fisher Scientific, Hampton, NH) overnight at 4°C on an orbital shaker. The following day, the slices were washed with 1X PBS 2 x 30 min and were incubated in 1:500 rabbit anti-Neuromedin B Receptor antibody (ABR-004, Alomone labs, Jerusalem) or 1:500 rabbit anti-Gastrin Releasing Peptide Receptor antibody (ABR-002, Alomone labs) and 1:250 goat anti-GFAP antibody (ab53554, Abcam) with 0.4% TritonX-100 overnight at 4°C on an orbital shaker. Sections were then washed 4 x 30 minutes with 1X PBS and placed in 1:200 donkey anti-rabbit Alexa 405 (711-475-152 Jackson ImmunoResearch Labs, West Grove, PA) and 1:500 donkey anti-goat Alexa 647 (705-605-147 Jackson ImmunoResearch Labs) for one hour. After washing for a minimum of 6 x 30 min with 1X PBS, sections were mounted on glass slides and cover-slipped with Vectashield hardset mounting medium (H-1500; Vector Laboratories, Burlingame, CA). Images were acquired with a 10x air and 60x oil immersion

objectives on a Nikon A1R confocal laser scanning microscope using NIS Elements AR imaging software (Nikon Instruments Inc., Melville, NY).

RESULTS

preBötC neurons express GRP receptors

Visualization of immunohistochemistry against GRP receptors and glial marker GFAP in both neonatal and adult *Dbx1^{CreERT2}; Rosa26^{tdTomato}* mouse brain slices revealed that GRP receptors are expressed in Dbx1 and non-Dbx1 preBötC neurons in neonatal mice and are not expressed in glia, as demonstrated in Figures 37 and 38.

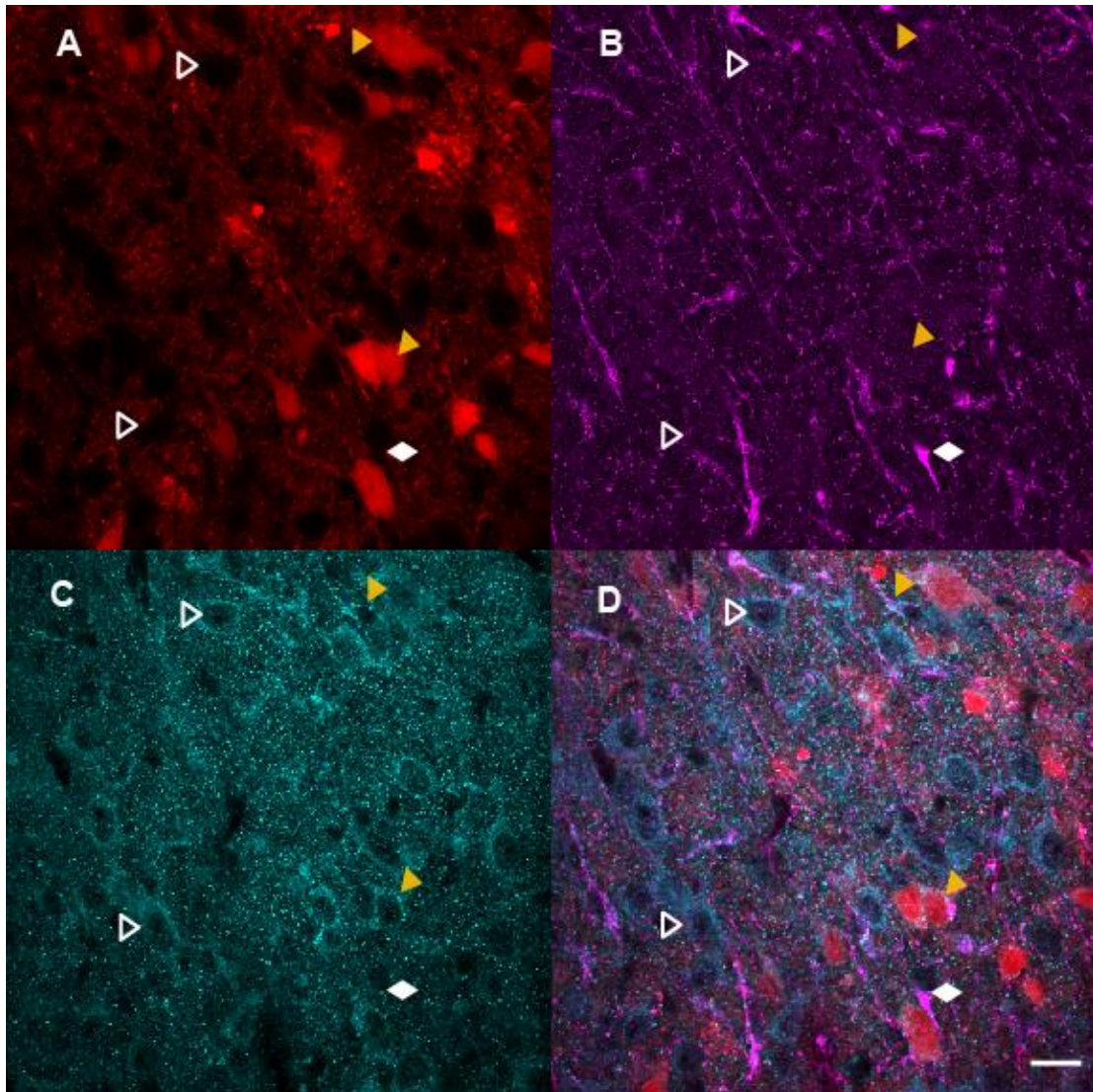


Figure 37. GRP receptors on Dbx1 and non-Dbx1 preBötC neurons in neonatal mice. Dbx1 neurons are labeled with tdTomato (A). Immunohistochemistry for the glial marker GFAP (B) GRP receptors (C) are combined with tdTomato labeling (D). Filled yellow triangles designate examples of GRP receptors on tdTomato neurons. White triangles designate examples of GRP receptors on non-Dbx1 neurons. White diamonds designate examples of glia labeling, none of which overlap with GRP receptor labeling. Scale bar is 20 μ m.

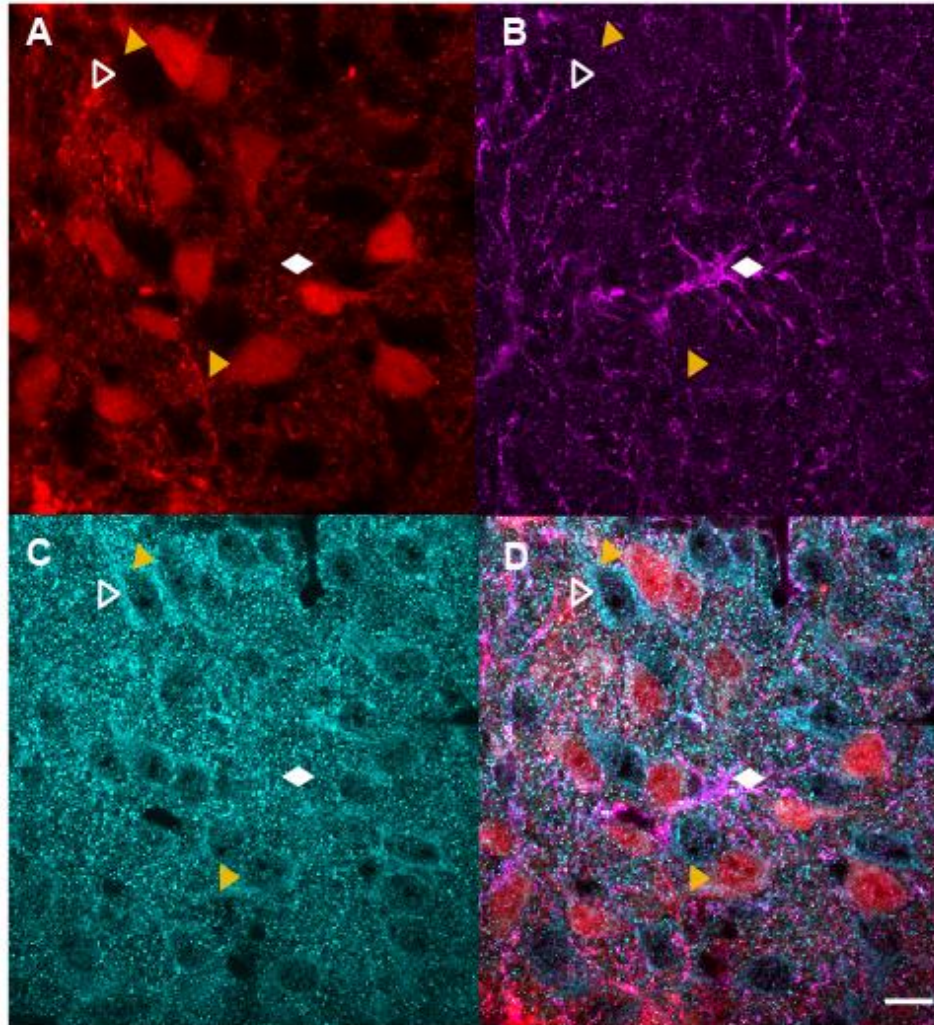


Figure 38. GPR receptors not present on glia in preBötC of neonatal mice. Dbx1 neurons are labeled with tdTomato (A). Immunohistochemistry for the glial marker GFAP (B) GPR receptors (C) are combined with tdTomato labeling (D). Filled yellow triangles designate examples of GPR receptors on tdTomato neurons. White triangles designate examples of GPR receptors on non-Dbx1 neurons. White diamonds designate examples of glia labeling, none of which overlap with GPR receptor labeling. Scale bar is 20 μm .

Figure 39 shows GRP receptor expression in preBötC neurons persists into adulthood while glia still do not express GRP receptors.

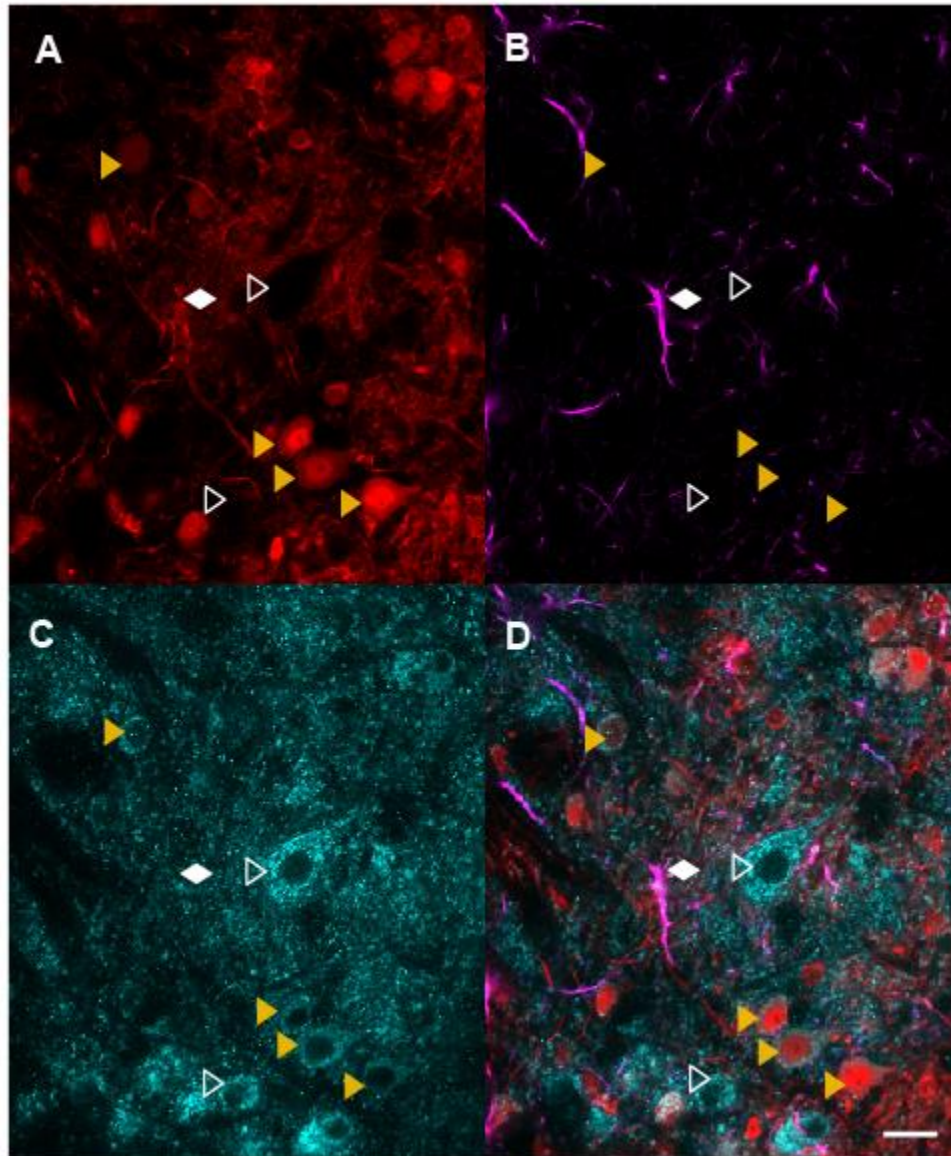


Figure 39. GRP receptors on Dbx1 and non-Dbx1 neurons in adult mice. Dbx1 neurons are labeled with tdTomato (A). Immunohistochemistry for the glial marker GFAP (B) GRP receptors (C) are combined with tdTomato labeling (D). Filled yellow triangles designate examples of GRP receptors on tdTomato neurons. White triangles designate examples of GRP receptors on non-Dbx1 neurons. White diamonds designate examples of glia labeling, none of which overlap with GRP receptor labeling. Scale bar is 20 μm .

preBötC neurons express NMB receptors

Immunohistochemistry against NMB receptors and glial marker GFAP in both neonatal and adult *Dbx1^{CreERT2}; Rosa26^{tdTomato}* mouse brain slices revealed that NMB receptors are expressed in Dbx1 and non-Dbx1 preBötC neurons in neonatal mice and are not expressed in glia, as demonstrated in Figure 40. Figure 41 shows NMB receptor expression in preBötC neurons persists into adulthood while glia still do not express NMB receptors.

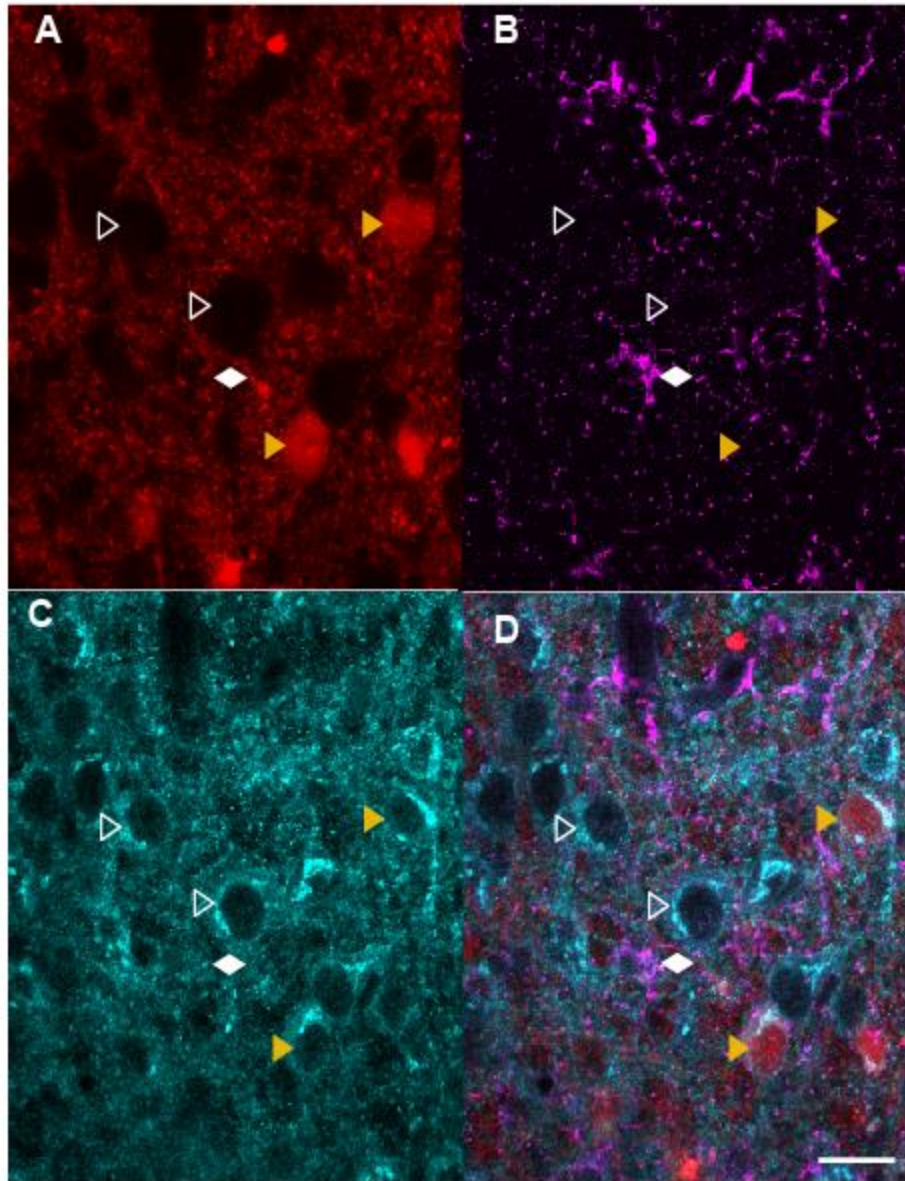


Figure 40. NMB receptors on Dbx1 and non-Dbx1 neurons in neonatal mice. Dbx1 neurons are labeled with tdTomato (A). Immunohistochemistry for the glial marker GFAP (B) NMB receptors (C) are combined with tdTomato labeling (D). Filled yellow triangles designate examples of NMB receptors on tdTomato neurons. White triangles designate examples of NMB receptors on non-Dbx1 neurons. White diamonds designate examples of glia labeling, none of which overlap with NMB receptor labeling. Scale bar is 20 μ m.

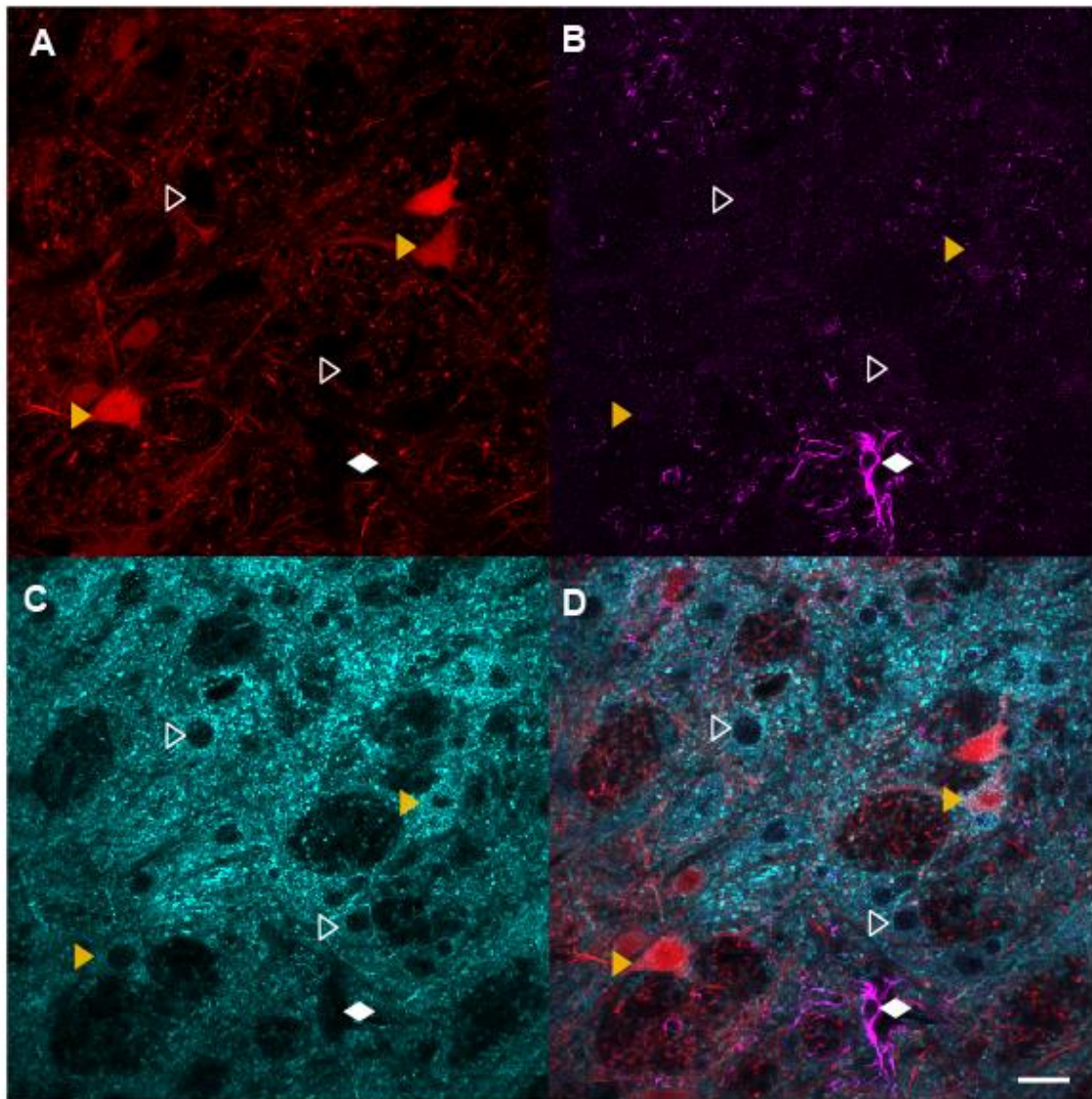


Figure 41. NMB receptors on Dbx1 and non-Dbx1 neurons in adult mice. Dbx1 neurons are labeled with tdTomato (A). Immunohistochemistry for the glial marker GFAP (B) NMB receptors (C) are combined with tdTomato labeling (D). Filled yellow triangles designate examples of NMB receptors on tdTomato neurons. White triangles designate examples of NMB receptors on non-Dbx1 neurons. White diamonds designate examples of glia labeling, none of which overlap with NMB receptor labeling. Scale bar is 20 μm .

DISCUSSION

The preBötC has been established as the site of eupneic respiratory rhythm generation. Investigation of the circuits for other respiratory behaviors such as sighs and gasps suggest the preBötC is an integral part of these behaviors as well. In 2000, recordings from the preBötC generated eupnea, sighs, and gasps – three distinct respiratory activity patterns (Lieske et al., 2000). Sigh bursts *in vitro* are physiologically distinct from eupneic bursts due to their larger amplitude and doublet peak. Both eupneic breaths and sighs must occur on a regular, periodic basis to sustain life (Cherniack et al., 1981; Ferris and Pollard, 1960; Koch et al., 2013); sighs prevent the collapse of alveoli, re-inflate alveoli that have collapsed, and help maintain normal lung function. Sighs are also proposed to reset eupneic breathing variability (Li and Yackle, 2017; Li et al., 2016; Ramirez, 2014, 2017; Vlemincx et al., 2010). Breathing variability is a normal and necessary occurrence, allowing the respiratory network to adapt to environmental changes and behaviors such as speech and laughter. Sighs terminate periods of irregular breathing and facilitate the return of breathing homeostasis. Mice that do not sigh due to genetic engineering develop fatal lung problems (Koch et al., 2013). Bombesin-like receptors NMBR and GRPR are important in the sigh signaling pathway (Li et al., 2016). We show that NMB and GRP receptors are present on Dbx1 and non-Dbx1 preBötC neurons and are not expressed on glia.

Sigh bursts have been recorded *in vitro* from the preBötC along with eupneic bursts (Lieske et. al., 2000), but the underlying mechanisms and possible microcircuits governing sighs are not yet clearly defined. One explanation for the generation of distinct breathing behaviors being generated by the same neural microcircuit is network reconfiguration; the preBötC can adopt different network states as a result of oxygen levels and neuromodulators present (Lieske et. al., 2000). Neural networks can generate several rhythmic neuronal activities with different timescales; this theory makes it possible for the preBötC to generate both eupnea and sighs. In fact, *in vitro* experimental data further suggests that the preBötC is involved in the generation of three distinct fictive breathing behaviors: eupnea, sighs, and gasps (Lieske et. al., 2000). The data provided in this chapter further corroborates this concept.

In vivo, eupnea occurs at a rate of 117 breaths/ne in rats and 218 breaths/hour in mice while sighs occur at an average rate of 44 sighs/hour in rats and 22 sighs/hour in mice (Li et al., 2016); thus, sighs occur at a relatively low frequency when compared to eupnea in both rats and mice. Glial modulation of breathing has been proposed as a theory to explain the different periodicities between eupneic bursts and sigh bursts because glia related behaviors, especially those involving Ca^{2+} signals, operate on a slower timescale than neuronal behaviors (Parpura et al., 2012). Also, Ca^{2+} signals in glial cells were observed to be synchronous with sigh bursts and glial toxins inhibited fictive sighs without altering eupneic bursts (Dashevskiy et al., 2016). Since NMB and GRP are shown to induce sigh bursts and neurons expressing NMB and GRP

project to the preBötC, one logical speculation was that glial cells would express NMB or GRP receptors. However, my anatomical data demonstrate that preBötC neurons, not glia, express NMB or GRP receptors. The presence of sigh NMB and GRP peptide receptors on preBötC neurons provide anatomical evidence that preBötC neurons, not glia, are part of the sigh signaling pathway. Those data definitively rule-out any sigh-generating mechanism that depends on peptidergic signaling to glia in the preBötC. This discovery also provides a basis for further experimentation through physiology to target NMB and GRP receptors in preBötC neurons to elucidate their functional role in sigh behavior.

REFERENCES

Abelson, J.L., Weg, J.G., Nesse, R.M., and Curtis, G.C. (2001). Persistent respiratory irregularity in patients with panic disorder. *Biol. Psychiatry* *49*, 588–595.

Abelson, J.L., Khan, S., Lyubkin, M., and Giardino, N. (2008). Respiratory irregularity and stress hormones in panic disorder: exploring potential linkages. *Depress. Anxiety* *25*, 885–887.

Akins, V.T., Weragalaarachchi, K., Picardo, M.C.D., Reville, A.L., and Negro, C.A.D. (2017). Morphology of Dbx1 respiratory neurons in the preBötzing complex and reticular formation of neonatal mice. *Sci. Data* *4*, sdata201797.

Alaynick, W.A., Jessell, T.M., and Pfaff, S.L. (2011). SnapShot: Spinal Cord Development. *Cell* *146*, 178–178.e1.

Amiel, J., Laudier, B., Attié-Bitach, T., Trang, H., de Pontual, L., Gener, B., Trochet, D., Etchevers, H., Ray, P., Simonneau, M., et al. (2003). Polyalanine expansion and frameshift mutations of the paired-like homeobox gene PHOX2B in congenital central hypoventilation syndrome. *Nat. Genet.* *33*, 459–461.

Amir, R.E., Van den Veyver, I.B., Wan, M., Tran, C.Q., Francke, U., and Zoghbi, H.Y. (1999). Rett syndrome is caused by mutations in X-linked MECP2, encoding methyl-CpG-binding protein 2. *Nat. Genet.* *23*, 185–188.

- Ballanyi, K., Onimaru, H., and Homma, I. (1999). Respiratory network function in the isolated brainstem-spinal cord of newborn rats. *Prog. Neurobiol.* *59*, 583–634.
- Beierlein, M. (2014). Chapter 17 - Cable Properties and Information Processing in Dendrites. In *From Molecules to Networks (Third Edition)*, J.H. Byrne, R. Heidelberger, and M.N. Waxham, eds. (Boston: Academic Press), pp. 509–529.
- Belykh, I., de Lange, E., and Hasler, M. (2005). Synchronization of Bursting Neurons: What Matters in the Network Topology. *Phys. Rev. Lett.* *94*, 188101.
- Benarroch, E.E. (2003). Brainstem in Multiple System Atrophy: Clinicopathological Correlations. *Cell. Mol. Neurobiol.* *23*, 519–526.
- Benarroch, E.E., Schmeichel, A.M., Low, P.A., and Parisi, J.E. (2003). Depletion of ventromedullary NK-1 receptor-immunoreactive neurons in multiple system atrophy. *Brain* *126*, 2183–2190.
- Ben-Mabrouk, F., and Tryba, A.K. (2010). Substance P modulation of TRPC3/7 channels improves respiratory rhythm regularity and ICAN-dependent pacemaker activity. *Eur. J. Neurosci.* *31*, 1219–1232.
- Bieger, D., and Hopkins, D.A. (1987). Viscerotopic representation of the upper alimentary tract in the medulla oblongata in the rat: The nucleus ambiguus. *J. Comp. Neurol.* *262*, 546–562.
- Blackman, A.V., Grabuschnig, S., Legenstein, R., and Sjöström, P.J. (2014). A comparison of manual neuronal reconstruction from biocytin histology or 2-photon imaging: morphometry and computer modeling. *Front. Neuroanat.* *8*.
- Blanchi, B., Kelly, L.M., Viemari, J.-C., Lafon, I., Burnet, H., Bévangut, M., Tillmanns, S., Daniel, L., Graf, T., Hilaire, G., et al. (2003). MafB deficiency causes defective respiratory rhythmogenesis and fatal central apnea at birth. *Nat. Neurosci.* *6*, 1091–1100.
- Bouvier, J., Thoby-Brisson, M., Renier, N., Dubreuil, V., Ericson, J., Champagnat, J., Pierani, A., Chédotal, A., and Fortin, G. (2010). Hindbrain interneurons and axon guidance signaling critical for breathing. *Nat. Neurosci.* *13*, 1066–1074.
- Bower, J.M., Beeman, D., and Hucka, M. (2003). The GENESIS Simulation System. In *The Handbook of Brain Theory and Neural Networks*, M.A. Arbib, ed. (Cambridge, MA: MIT Press), pp. 475–478.
- Briscoe, J., and Ericson, J. (1999). The specification of neuronal identity by graded sonic hedgehog signalling. *Semin. Cell Dev. Biol.* *10*, 353–362.

- Brown, T.G. (1914). On the nature of the fundamental activity of the nervous centres; together with an analysis of the conditioning of rhythmic activity in progression, and a theory of the evolution of function in the nervous system. *J. Physiol.* *48*, 18–46.
- Brunnström, H.R., and Englund, E.M. (2009). Cause of death in patients with dementia disorders. *Eur. J. Neurol.* *16*, 488–492.
- Chamberlin, N.L., Eikermann, M., Fassbender, P., White, D.P., and Malhotra, A. (2007). Genioglossus premotoneurons and the negative pressure reflex in rats. *J. Physiol.* *579*, 515–526.
- Cherniack, N.S., Euler, C., Glogowska, M., and Homma, I. (1981). Characteristics and rate of occurrence of spontaneous and provoked augmented breaths. *Acta Physiol.* *111*, 349–360.
- Chevalier, M., Toporikova, N., Simmers, J., and Thoby-Brisson, M. Development of pacemaker properties and rhythmogenic mechanisms in the mouse embryonic respiratory network. *ELife* *5*.
- Crowder, E.A., Saha, M.S., Pace, R.W., Zhang, H., Prestwich, G.D., and Del Negro, C.A. (2007). Phosphatidylinositol 4,5-bisphosphate regulates inspiratory burst activity in the neonatal mouse preBötzinger complex. *J. Physiol.* *582*, 1047–1058.
- Cui, K., and Yuan, X. (2007). TRP Channels and Axon Pathfinding. In *TRP Ion Channel Function in Sensory Transduction and Cellular Signaling Cascades*, (CRC Press), pp. 55–68.
- Cui, Y., Kam, K., Sherman, D., Janczewski, W.A., Zheng, Y., and Feldman, J.L. (2016). Defining preBötzinger Complex Rhythm- and Pattern-Generating Neural Microcircuits In Vivo. *Neuron* *91*, 602–614.
- Darnall, R.A. (2013). The carotid body and arousal in the fetus and neonate. *Respir. Physiol. Neurobiol.* *185*, 132–143.
- Dashevskiy, T., Bloom, J., and Ramirez, J.-M. (2016). To Sigh Or Not To Sigh: Role Of Glia In Sigh Generation. *FASEB J.* *30*, 987.6-987.6.
- Del Negro, C.A., Koshiya, N., Butera, R.J., and Smith, J.C. (2002a). Persistent sodium current, membrane properties and bursting behavior of pre-bötzinger complex inspiratory neurons in vitro. *J. Neurophysiol.* *88*, 2242–2250.
- Del Negro, C.A., Morgado-Valle, C., and Feldman, J.L. (2002b). Respiratory rhythm: an emergent network property? *Neuron* *34*, 821–830.
- Del Negro, C.A., Morgado-Valle, C., Hayes, J.A., Mackay, D.D., Pace, R.W., Crowder, E.A., and Feldman, J.L. (2005). Sodium and calcium current-mediated

pacemaker neurons and respiratory rhythm generation. *J. Neurosci. Off. J. Soc. Neurosci.* 25, 446–453.

Del Negro, C.A., Hayes, J.A., Pace, R.W., Brush, B.R., Teruyama, R., and Feldman, J.L. (2010). Synaptically activated burst-generating conductances may underlie a group-pacemaker mechanism for respiratory rhythm generation in mammals. *Prog. Brain Res.* 187, 111–136.

Del Negro, C.A., Hayes, J.A., and Rekling, J.C. (2011). Dendritic calcium activity precedes inspiratory bursts in preBotzinger complex neurons. *J. Neurosci. Off. J. Soc. Neurosci.* 31, 1017–1022.

Di Fiore, J.M., Martin, R.J., and Gauda, E.B. (2013). Apnea of prematurity – Perfect storm. *Respir. Physiol. Neurobiol.* 189, 213–222.

Doble, A. (1996). The pharmacology and mechanism of action of riluzole. *Neurology* 47, S233-241.

Dubreuil, V., Ramanantsoa, N., Trochet, D., Vaubourg, V., Amiel, J., Gallego, J., Brunet, J.-F., and Golidis, C. (2008). A human mutation in *Phox2b* causes lack of CO₂ chemosensitivity, fatal central apnea, and specific loss of parafacial neurons. *Proc. Natl. Acad. Sci.* 105, 1067–1072.

Dutschmann, M., Bautista, T.G., Mörschel, M., and Dick, T.E. (2014). Learning to breathe: Habituation of Hering–Breuer inflation reflex emerges with postnatal brainstem maturation. *Respir. Physiol. Neurobiol.* 195, 44–49.

Euler, C. von (1983). On the central pattern generator for the basic breathing rhythmicity. *J. Appl. Physiol.* 55, 1647–1659.

Feldman, J.L. (2011). Neurophysiology of Breathing in Mammals. In *Comprehensive Physiology*, (John Wiley & Sons, Inc.), p.

Feldman, J.L., and Del Negro, C.A. (2006). Looking for inspiration: new perspectives on respiratory rhythm. *Nat. Rev. Neurosci.* 7, 232–241.

Feldman, J.L., and Smith, J.C. (1989). Cellular Mechanisms Underlying Modulation of Breathing Pattern in Mammals. *Ann. N. Y. Acad. Sci.* 563, 114–130.

Feldman, J.L., Del Negro, C.A., and Gray, P.A. (2013). Understanding the rhythm of breathing: so near, yet so far. *Annu. Rev. Physiol.* 75, 423–452.

Ferrante, M., Migliore, M., and Ascoli, G.A. (2013). Functional impact of dendritic branch-point morphology. *J. Neurosci. Off. J. Soc. Neurosci.* 33, 2156–2165.

- Ferris, B.G., and Pollard, D.S. (1960). EFFECT OF DEEP AND QUIET BREATHING ON PULMONARY COMPLIANCE IN MAN*. *J. Clin. Invest.* 39, 143–149.
- Franco, P., Verheulpen, D., Valente, F., Kelmanson, I., de Broca, A., Scaillet, S., Groswasser, J., and Kahn, A. (2003). Autonomic responses to sighs in healthy infants and in victims of sudden infant death. *Sleep Med.* 4, 569–577.
- Fregosi, R.F., and Ludlow, C.L. (2014). Activation of upper airway muscles during breathing and swallowing. *J. Appl. Physiol.* 116, 291–301.
- Frigon, A. (2012). Central Pattern Generators of the Mammalian Spinal Cord. *The Neuroscientist* 18, 56–69.
- Funk, G.D., and Greer, J.J. (2013). The rhythmic, transverse medullary slice preparation in respiratory neurobiology: contributions and caveats. *Respir. Physiol. Neurobiol.* 186, 236–253.
- Funk, G.D., Smith, J.C., and Feldman, J.L. (1993). Generation and transmission of respiratory oscillations in medullary slices: role of excitatory amino acids. *J. Neurophysiol.* 70, 1497–1515.
- Furness, J.B., Alex, G., Clark, M.J., and Lal, V.V. (2003). Morphologies and projections of defined classes of neurons in the submucosa of the guinea-pig small intestine. *Anat. Rec. A. Discov. Mol. Cell. Evol. Biol.* 272A, 475–483.
- Gaig, C., and Iranzo, A. (2012). Sleep-Disordered Breathing in Neurodegenerative Diseases. *Curr. Neurol. Neurosci. Rep.* 12, 205–217.
- Garcia III, A.J., Koschnitzky, J.E., and Ramirez, J.-M. (2013). The physiological determinants of Sudden Infant Death Syndrome. *Respir. Physiol. Neurobiol.* 189, 288–300.
- Garcia-Campmany, L., Stam, F.J., and Goulding, M. (2010). From circuits to behaviour: motor networks in vertebrates. *Curr. Opin. Neurobiol.* 20, 116–125.
- Gestreau, C., Dutschmann, M., Obled, S., and Bianchi, A.L. (2005). Activation of XII motoneurons and premotor neurons during various oropharyngeal behaviors. *Respir. Physiol. Neurobiol.* 147, 159–176.
- Goodman, C.S., and Shatz, C.J. (1993). Developmental mechanisms that generate precise patterns of neuronal connectivity. *Cell* 72, 77–98.
- Gray, P.A. (1999). Modulation of Respiratory Frequency by Peptidergic Input to Rhythmogenic Neurons in the PreBötzing Complex. *Science* 286, 1566–1568.

- Gray, P.A. (2008). Transcription factors and the genetic organization of brain stem respiratory neurons. *J. Appl. Physiol.* *104*, 1513–1521.
- Gray, P.A. (2013). Transcription factors define the neuroanatomical organization of the medullary reticular formation. *Front. Neuroanat.* *7*, 7.
- Gray, P.A., Rekling, J.C., Bocchiaro, C.M., and Feldman, J.L. (1999). Modulation of Respiratory Frequency by Peptidergic Input to Rhythmogenic Neurons in the PreBötzinger Complex. *Science* *286*, 1566–1568.
- Gray, P.A., Janczewski, W.A., Mellen, N., McCrimmon, D.R., and Feldman, J.L. (2001). Normal breathing requires preBötzinger complex neurokinin-1 receptor-expressing neurons. *Nat. Neurosci.* *4*, 927–930.
- Gray, P.A., Hayes, J.A., Ling, G.Y., Llona, I., Tupal, S., Picardo, M.C.D., Ross, S.E., Hirata, T., Corbin, J.G., Eugenin, J., et al. (2010). Developmental origin of preBötzinger complex respiratory neurons. *J. Neurosci.* *30*, 14883–14895.
- Grillner, S. (2006). Biological pattern generation: the cellular and computational logic of networks in motion. *Neuron* *52*, 751–766.
- Grillner, S., and Jessell, T.M. (2009). Measured motion: searching for simplicity in spinal locomotor networks. *Curr. Opin. Neurobiol.* *19*, 572–586.
- Grillner, S., and Manira, A.E. (2015). The intrinsic operation of the networks that make us locomote. *Curr. Opin. Neurobiol.* *31*, 244–249.
- Groswasser, J., Simon, T., Scaillet, S., Franco, P., and Kahn, A. (2001). Reduced Arousals Following Obstructive Apneas in Infants Sleeping Prone. *Pediatr. Res.* *49*, 402.
- Guertin, P.A. (2013). Central pattern generator for locomotion: anatomical, physiological, and pathophysiological considerations. *Mov. Disord.* *3*, 183.
- Guillery, R.W. (2007). Relating the neuron doctrine to the cell theory. Should contemporary knowledge change our view of the neuron doctrine? *Brain Res. Rev.* *55*, 411–421.
- Guinamard, R., Hof, T., and Del Negro, C.A. (2014). The TRPM4 channel inhibitor 9-phenanthrol. *Br. J. Pharmacol.* *171*, 1600–1613.
- Guyenet, P.G., and Bayliss, D.A. (2015). Neural Control of Breathing and CO₂ Homeostasis. *Neuron* *87*, 946–961.
- Guyenet, P.G., Mulkey, D.K., Stornetta, R.L., and Bayliss, D.A. (2005). Regulation of Ventral Surface Chemoreceptors by the Central Respiratory Pattern Generator. *J. Neurosci.* *25*, 8938–8947.

- Guyenet, P.G., Bayliss, D.A., Stornetta, R.L., Fortuna, M.G., Abbott, S.B.G., and DePuy, S.D. (2009). Retrotrapezoid nucleus, respiratory chemosensitivity and breathing automaticity. *Respir. Physiol. Neurobiol.* 168, 59–68.
- Guyenet, P.G., Stornetta, R.L., and Bayliss, D.A. (2010). Central respiratory chemoreception. *J. Comp. Neurol.* 518, 3883–3906.
- Halavi, M., Polavaram, S., Donohue, D.E., Hamilton, G., Hoyt, J., Smith, K.P., and Ascoli, G.A. (2008). NeuroMorpho.Org Implementation of Digital Neuroscience: Dense Coverage and Integration with the NIF. *Neuroinformatics* 6, 241.
- Halavi, M., Hamilton, K.A., Parekh, R., and Ascoli, G.A. (2012). Digital reconstructions of neuronal morphology: three decades of research trends. *Front. Neurosci.* 6, 49.
- Hama, H., Kurokawa, H., Kawano, H., Ando, R., Shimogori, T., Noda, H., Fukami, K., Sakaue-Sawano, A., and Miyawaki, A. (2011). Scale: a chemical approach for fluorescence imaging and reconstruction of transparent mouse brain. *Nat. Neurosci.* 14, 1481–1488.
- Hammer, O., Harper, D.A.T., and Ryan, P.D. (2001). PAST: Paleontological statistics software package for education and data analysis. *Palaeontologica Electronica* 4, 1–9.
- Hartmann, J., Dragicevic, E., Adelsberger, H., Henning, H.A., Sumser, M., Abramowitz, J., Blum, R., Dietrich, A., Freichel, M., Flockerzi, V., et al. (2008). TRPC3 Channels Are Required for Synaptic Transmission and Motor Coordination. *Neuron* 59, 392–398.
- Hayes, J. (2017). Molecular mechanisms of respiratory rhythm and pattern generation: role of sodium and mixed cationic channels. (Merton College, Oxford, UK).
- Hayes, J.A., Kottick, A., Picardo, M.C.D., Halleran, A.D., Smith, R.D., Smith, G.D., Saha, M.S., and Del Negro, C.A. (2017). Transcriptome of neonatal preBötzing complex neurones in Dbx1 reporter mice. *Sci. Rep.* 7.
- Hines, M.L., and Carnevale, N.T. (1997). The NEURON simulation environment. *Neural Comput.* 9, 1179–1209.
- Hirata, T., Li, P., Lanuza, G.M., Cocas, L.A., Huntsman, M.M., and Corbin, J.G. (2009). Identification of distinct telencephalic progenitor pools for neuronal diversity in the amygdala. *Nat. Neurosci.* 12, 141–149.
- Hofmann, T., Chubanov, V., Gudermann, T., and Montell, C. (2003). TRPM5 Is a Voltage-Modulated and Ca²⁺-Activated Monovalent Selective Cation Channel. *Curr. Biol.* 13, 1153–1158.

- Jacobs, G., Claiborne, B., and Harris, K. (2010). Reconstruction of Neuronal Morphology. In *Computational Modeling Methods for Neuroscientists*, E. de Schutter, ed. (MIT Press), pp. 187–210.
- Jacquin, T.D., Borday, V., Schneider-Maunoury, S., Topilko, P., Ghilini, G., Kato, F., Charnay, P., and Champagnat, J. (1996). Reorganization of Pontine Rhythmogenic Neuronal Networks in Krox-20 Knockout Mice. *Neuron* *17*, 747–758.
- Janczewski, W.A., and Feldman, J.L. (2006). Distinct rhythm generators for inspiration and expiration in the juvenile rat. *J. Physiol.* *570*, 407–420.
- Janczewski, W.A., Tashima, A., Hsu, P., Cui, Y., and Feldman, J.L. (2013). Role of Inhibition in Respiratory Pattern Generation. *J. Neurosci.* *33*, 5454–5465.
- Jensen, R.T., Battey, J.F., Spindel, E.R., and Benya, R.V. (2008). International Union of Pharmacology. LXVIII. Mammalian Bombesin Receptors: Nomenclature, Distribution, Pharmacology, Signaling, and Functions in Normal and Disease States. *Pharmacol. Rev.* *60*, 1–42.
- Julu, P.O.O., Kerr, A.M., Apartopoulos, F., Al-Rawas, S., Engerström, I.W., Engerström, L., Jamal, G.A., and Hansen, S. (2001). Characterisation of breathing and associated central autonomic dysfunction in the Rett disorder. *Arch. Dis. Child.* *85*, 29–37.
- Kahn, A., Blum, D., Rebuffat, E., Sottiaux, M., Levitt, J., Bochner, A., Alexander, M., Grosswasser, J., and Muller, M.F. (1988). Polysomnographic Studies of Infants Who Subsequently Died of Sudden Infant Death Syndrome. *Pediatrics* *82*, 721–727.
- Kahn, A., Grosswasser, J., Rebuffat, E., Sottiaux, M., Blum, D., Foerster, M., Franco, P., Bochner, A., Alexander, M., and Bachy, A. (1992). Sleep and cardiorespiratory characteristics of infant victims of sudden death: a prospective case-control study. *Sleep* *15*, 287–292.
- Kiehn, O. (2016). Decoding the organization of spinal circuits that control locomotion. *Nat. Rev. Neurosci.* *17*, 224–238.
- Kleinfeld, D., Deschênes, M., Wang, F., and Moore, J.D. (2014). More than a rhythm of life: breathing as a binder of orofacial sensation. *Nat. Neurosci.* *17*, 647–651.
- Koch, H., Zanella, S., Elsen, G.E., Smith, L., Doi, A., Garcia, A.J., Wei, A.D., Xun, R., Kirsch, S., Gomez, C.M., et al. (2013). Stable Respiratory Activity Requires Both P/Q-Type and N-Type Voltage-Gated Calcium Channels. *J. Neurosci.* *33*, 3633–3645.

- Koizumi, H., and Smith, J.C. (2008). Persistent Na⁺ and K⁺-Dominated Leak Currents Contribute to Respiratory Rhythm Generation in the Pre-Bötzinger Complex In Vitro. *J. Neurosci.* 28, 1773–1785.
- Koizumi, H., Wilson, C.G., Wong, S., Yamanishi, T., Koshiya, N., and Smith, J.C. (2008). Functional imaging, spatial reconstruction, and biophysical analysis of a respiratory motor circuit isolated in vitro. *J. Neurosci.* 28, 2353–2365.
- Koizumi, H., Koshiya, N., Chia, J.X., Cao, F., Nugent, J., Zhang, R., and Smith, J.C. (2013). Structural-functional properties of identified excitatory and inhibitory interneurons within pre-Botzinger complex respiratory microcircuits. *J. Neurosci. Off. J. Soc. Neurosci.* 33, 2994–3009.
- Koizumi, H., Mosher, B., Tariq, M.F., Zhang, R., Koshiya, N., and Smith, J.C. (2016). Voltage-Dependent Rhythmogenic Property of Respiratory Pre-Bötzinger Complex Glutamatergic, Dbx1-Derived, and Somatostatin-Expressing Neuron Populations Revealed by Graded Optogenetic Inhibition. *ENeuro* 3, ENEURO.0081-16.2016.
- Komendantov, A.O., and Ascoli, G.A. (2009). Dendritic Excitability and Neuronal Morphology as Determinants of Synaptic Efficacy. *J. Neurophysiol.* 101, 1847–1866.
- Kottick, A., Martin, C.A., and Negro, C.A.D. (2017). Fate mapping neurons and glia derived from Dbx1- expressing progenitors in mouse preBötzinger complex. *Physiol. Rep.* 5, e13300.
- Langhammer, C.G., Previtara, M.L., Sweet, E.S., Sran, S.S., Chen, M., and Firestein, B.L. (2010). Automated Sholl analysis of digitized neuronal morphology at multiple scales: Whole cell Sholl analysis versus Sholl analysis of arbor subregions. *Cytometry A* 77A, 1160–1168.
- Lanuza, G.M., Gosgnach, S., Pierani, A., Jessell, T.M., and Goulding, M. (2004). Genetic identification of spinal interneurons that coordinate left-right locomotor activity necessary for walking movements. *Neuron* 42, 375–386.
- Launay, P., Fleig, A., Perraud, A.-L., Scharenberg, A.M., Penner, R., and Kinet, J.-P. (2002). TRPM4 Is a Ca²⁺-Activated Nonselective Cation Channel Mediating Cell Membrane Depolarization. *Cell* 109, 397–407.
- Leary, S., Underwood, W., Anthony, R., Cartner, S., Corey, D., Grandin, T., Greenacre, C.B., Gwaltney-Bran, S., McCrackin, M.A., Meyer, R., et al. (2013). AVMA guidelines for the euthanasia of animals: 2013 edition.
- Li, P., and Yackle, K. (2017). Sighing. *Curr. Biol.* 27, R88–R89.

Li, P., Janczewski, W.A., Yackle, K., Kam, K., Pagliardini, S., Krasnow, M.A., and Feldman, J.L. (2016). The peptidergic control circuit for sighing. *Nature* 530, 293–297.

Li, Y., Jia, Y.-C., Cui, K., Li, N., Zheng, Z.-Y., Wang, Y., and Yuan, X. (2005). Essential role of TRPC channels in the guidance of nerve growth cones by brain-derived neurotrophic factor. *Nature* 434, 894–898.

Liang, J., Tang, M.-L., and Chan, P.S. (2009). A generalized Shapiro–Wilk statistic for testing high-dimensional normality. *Comput. Stat. Data Anal.* 53, 3883–3891.

Lieske, S.P.T.-B., M. Telgkamp. P. Ramirez. J.M. (2000). Reconfiguration of the neural network controlling multiple breathing patterns: eupnea, sighs and gasps. *Nat. Neurosci.* 3, 600.

Lischinsky, J.E., Sokolowski, K., Li, P., Esumi, S., Kamal, Y., Goodrich, M., Oboti, L., Hammond, T.R., Krishnamoorthy, M., Feldman, D., et al. Embryonic transcription factor expression in mice predicts medial amygdala neuronal identity and sex-specific responses to innate behavioral cues. *ELife* 6.

Llinás, R.R. (2003). Opinion: The contribution of Santiago Ramon y Cajal to functional neuroscience. *Nat. Rev. Neurosci.* 4, 77.

Madisen, L., Zwingman, T.A., Sunkin, S.M., Oh, S.W., Zariwala, H.A., Gu, H., Ng, L.L., Palmiter, R.D., Hawrylycz, M.J., Jones, A.R., et al. (2010). A robust and high-throughput Cre reporting and characterization system for the whole mouse brain. *Nat. Neurosci.* 13, 133–140.

Madisen, L., Mao, T., Koch, H., Zhuo, J., Berenyi, A., Fujisawa, S., Hsu, Y.-W.A., Li, A.J.G., Gu, X., Zanella, S., et al. (2012). A toolbox of Cre-dependent optogenetic transgenic mice for light-induced activation and silencing. *Nat. Neurosci.* 15, 793–802.

Mainen, Z.F., and Sejnowski, T.J. (1996). Influence of dendritic structure on firing pattern in model neocortical neurons. *Nature* 382, 363–366.

Marchenko, V., Koizumi, H., Mosher, B., Koshiya, N., Tariq, M.F., Bezdudnaya, T.G., Zhang, R., Molkov, Y.I., Rybak, I.A., and Smith, J.C. (2016). Perturbations of Respiratory Rhythm and Pattern by Disrupting Synaptic Inhibition within Pre-Bötzinger and Böttinger Complexes. *ENeuro* 3, ENEURO.0011-16.2016.

Marder, E., Goeritz, M.L., and Otopalik, A.G. (2015). Robust circuit rhythms in small circuits arise from variable circuit components and mechanisms. *Curr. Opin. Neurobiol.* 31, 156–163.

Martin, R.J., and Wilson, C.G. (2012). Apnea of Prematurity. In *Comprehensive Physiology*, (John Wiley & Sons, Inc.), p.

- McKay, L.C., Janczewski, W.A., and Feldman, J.L. (2005). Sleep-disordered breathing after targeted ablation of preBötzinger complex neurons. *Nat. Neurosci.* 8, 1142.
- McLean, D.L., and Dougherty, K.J. (2015). Peeling back the layers of locomotor control in the spinal cord. *Curr. Opin. Neurobiol.* 33, 63–70.
- Mironov, S.L. (2008). Metabotropic glutamate receptors activate dendritic calcium waves and TRPM channels which drive rhythmic respiratory patterns in mice. *J. Physiol.* 586, 2277–2291.
- Mironov, S.L., and Skorova, E.Y. (2011). Stimulation of bursting in pre-Bötzinger neurons by Epac through calcium release and modulation of TRPM4 and K-ATP channels. *J. Neurochem.* 117, 295–308.
- Moore, J.D., Deschênes, M., Furuta, T., Huber, D., Smear, M.C., Demers, M., and Kleinfeld, D. (2013). Hierarchy of orofacial rhythms revealed through whisking and breathing. *Nature* 497, 205–210.
- Moore, J.D., Kleinfeld, D., and Wang, F. (2014). How the brainstem controls orofacial behaviors comprised of rhythmic actions. *Trends Neurosci.* 37, 370–380.
- Moran-Rivard, L., Kagawa, T., Saueressig, H., Gross, M.K., Burrill, J., and Goulding, M. (2001). *Evx1* Is a Postmitotic Determinant of V0 Interneuron Identity in the Spinal Cord. *Neuron* 29, 385–399.
- Morgado-Valle, C., Beltran-Parrazal, L., DiFranco, M., Vergara, J.L., and Feldman, J.L. (2008). Somatic Ca²⁺ transients do not contribute to inspiratory drive in preBötzinger Complex neurons. *J. Physiol.* 586, 4531–4540.
- Myatt, D.R., Hadlington, T., Ascoli, G.A., and Nasuto, S.J. (2012). Neuromantic - from semi-manual to semi-automatic reconstruction of neuron morphology. *Front. Neuroinformatics* 6, 4.
- Niewoehner, D.E., Levine, A.S., and Morley, J.E. (1983). Central effects of neuropeptides on ventilation in the rat. *Peptides* 4, 277–281.
- NIH Office of Laboratory Animal Welfare (2015). Public Health Service policy on humane care and use of laboratory animals (Office of Laboratory Animal Welfare, National Institutes of Health, Department of Health and Human Services).
- Nusbaum, M.P., and Blitz, D.M. (2012). Neuropeptide modulation of microcircuits. *Curr. Opin. Neurobiol.* 22, 592–601.
- Okhotin, V.E., and Kalinichenko, S.G. (2002). The Histophysiology of Neocortical Basket Cells. *Neurosci. Behav. Physiol.* 32, 455–470.

- Ono, T., Ishiwata, Y., Inaba, N., Kuroda, T., and Nakamura, Y. (1998). Modulation of the Inspiratory-Related Activity of Hypoglossal Premotor Neurons During Ingestion and Rejection in the Decerebrate Cat. *J. Neurophysiol.* *80*, 48–58.
- Orem, J., and Trotter, R.H. (1993). Medullary respiratory neuronal activity during augmented breaths in intact unanesthetized cats. *J. Appl. Physiol.* *74*, 761–769.
- Osorio, N., Cathala, L., Meisler, M.H., Crest, M., Magistretti, J., and Delmas, P. (2010). Persistent Nav1.6 current at axon initial segments tunes spike timing of cerebellar granule cells. *J. Physiol.* *588*, 651–670.
- Oyster, C.W., Takahashi, E.S., and Hurst, D.C. (1981). Density, soma size, and regional distribution of rabbit retinal ganglion cells. *J. Neurosci. Off. J. Soc. Neurosci.* *1*, 1331–1346.
- Pace, R.W., and Del Negro, C.A. (2008). AMPA and metabotropic glutamate receptors cooperatively generate inspiratory-like depolarization in mouse respiratory neurons in vitro. *Eur. J. Neurosci.* *28*, 2434–2442.
- Pace, R.W., Mackay, D.D., Feldman, J.L., and Del Negro, C.A. (2007a). Role of persistent sodium current in mouse preBötzinger Complex neurons and respiratory rhythm generation. *J. Physiol.* *580*, 485–496.
- Pace, R.W., Mackay, D.D., Feldman, J.L., and Del Negro, C.A. (2007b). Inspiratory bursts in the preBötzinger complex depend on a calcium-activated non-specific cation current linked to glutamate receptors in neonatal mice. *J. Physiol.* *582*, 113–125.
- Pagliardini, S., Ren, J., Gray, P.A., Vandunk, C., Gross, M., Goulding, M., and Greer, J.J. (2008). Central respiratory rhythmogenesis is abnormal in *lhx1*-deficient mice. *J. Neurosci. Off. J. Soc. Neurosci.* *28*, 11030–11041.
- Parekh, R., and Ascoli, G.A. (2013). Neuronal morphology goes digital: a research hub for cellular and system neuroscience. *Neuron* *77*, 1017–1038.
- Parekh, R., and Ascoli, G.A. (2014). Quantitative Investigations of Axonal and Dendritic Arbors: Development, Structure, Function, and Pathology. *Neurosci. Rev. J. Bringing Neurobiol. Neurol. Psychiatry.*
- Parekh, R., and Ascoli, G.A. (2015). Quantitative investigations of axonal and dendritic arbors: development, structure, function, and pathology. *The Neuroscientist* *21*, 241–254.
- Parpura, V., Heneka, M.T., Montana, V., Oliet, S.H.R., Schousboe, A., Haydon, P.G., Stout, R.F., Spray, D.C., Reichenbach, A., Pannicke, T., et al. (2012). Glial cells in (patho)physiology. *J. Neurochem.* *121*, 4–27.

- Paton, J.F.R., Abdala, A.P.L., Koizumi, H., Smith, J.C., and St-John, W.M. (2006). Respiratory rhythm generation during gasping depends on persistent sodium current. *Nat. Neurosci.* 9, 311–313.
- Peever, J.H., Shen, L., and Duffin, J. (2002). Respiratory pre-motor control of hypoglossal motoneurons in the rat. *Neuroscience* 110, 711–722.
- Peña, F., and Ramirez, J.-M. (2002). Endogenous activation of serotonin-2A receptors is required for respiratory rhythm generation in vitro. *J. Neurosci. Off. J. Soc. Neurosci.* 22, 11055–11064.
- Peña, F., Parkis, M.A., Tryba, A.K., and Ramirez, J.-M. (2004). Differential contribution of pacemaker properties to the generation of respiratory rhythms during normoxia and hypoxia. *Neuron* 43, 105–117.
- Picardo, M.C.D., Weragalaarachchi, K.T.H., Akins, V.T., and Del Negro, C.A. (2013). Physiological and morphological properties of *Dbx1* -derived respiratory neurons in the preBötzinger complex of neonatal mice. *J. Physiol.* 591, 2687–2703.
- Pierani, A., Moran-Rivard, L., Sunshine, M.J., Littman, D.R., Goulding, M., and Jessell, T.M. (2001). Control of interneuron fate in the developing spinal cord by the progenitor homeodomain protein *Dbx1*. *Neuron* 29, 367–384.
- Pohanka, M. (2009). Monoclonal and polyclonal antibodies production - preparation of potent biorecognition element. 7, 115–121.
- Preibisch, S., Saalfeld, S., and Tomancak, P. (2009). Globally optimal stitching of tiled 3D microscopic image acquisitions. *Bioinformatics* 25, 1463–1465.
- Ptak, K., Zummo, G.G., Alheid, G.F., Tkatch, T., Surmeier, D.J., and McCrimmon, D.R. (2005). Sodium Currents in Medullary Neurons Isolated from the Pre-Bötzinger Complex Region. *J. Neurosci.* 25, 5159–5170.
- Rall, W. (1969). Time Constants and Electrotonic Length of Membrane Cylinders and Neurons. *Biophys. J.* 9, 1483–1508.
- Raman, I.M., and Bean, B.P. (1997). Resurgent Sodium Current and Action Potential Formation in Dissociated Cerebellar Purkinje Neurons. *J. Neurosci.* 17, 4517–4526.
- Ramirez, J.-M. (2014). The Integrative Role of the Sigh in Psychology, Physiology, Pathology, and Neurobiology. *Prog. Brain Res.* 209, 91–129.
- Ramirez, J.M. (2017). The sigh: A biological rhythm in the interface between physiology and psychology. IUPS 38th World Congress: Rhythms of Life. (Brazil).

- Ramirez, J.-M., Dashevskiy, T., Marlin, I.A., and Baertsch, N. (2016). Microcircuits in respiratory rhythm generation: commonalities with other rhythm generating networks and evolutionary perspectives. *Curr. Opin. Neurobiol.* *41*, 53–61.
- Rekling, J.C., and Feldman, J.L. (1998). PreBötzinger complex and pacemaker neurons: hypothesized site and kernel for respiratory rhythm generation. *Annu. Rev. Physiol.* *60*, 385–405.
- Rekling, J.C., Champagnat, J., and Denavit-Saubié, M. (1996). Electroresponsive properties and membrane potential trajectories of three types of inspiratory neurons in the newborn mouse brain stem in vitro. *J. Neurophysiol.* *75*, 795–810.
- Revill, A.L., Vann, N.C., Akins, V.T., Kottick, A., Gray, P.A., Negro, C.A.D., and Funk, G.D. (2015). Dbx1 precursor cells are a source of inspiratory XII premotoneurons. *ELife* *4*, e12301.
- Reynolds, L.B. (1962). Characteristics of an inspiration-augmenting reflex in anesthetized cats. *J. Appl. Physiol.* *17*, 683–688.
- Richter, D.W., and Smith, J.C. (2014). Respiratory rhythm generation in vivo. *Physiol. Bethesda Md* *29*, 58–71.
- Rose, M.F., Ren, J., Ahmad, K.A., Chao, H.-T., Klisch, T.J., Flora, A., Greer, J.J., and Zoghbi, H.Y. (2009). Math1 Is Essential for the Development of Hindbrain Neurons Critical for Perinatal Breathing. *Neuron* *64*, 341–354.
- Ruangkittisakul, A., Schwarzacher, S.W., Secchia, L., Poon, B.Y., Ma, Y., Funk, G.D., and Ballanyi, K. (2006). High sensitivity to neuromodulator-activated signaling pathways at physiological [K⁺] of confocally imaged respiratory center neurons in on-line-calibrated newborn rat brainstem slices. *J. Neurosci. Off. J. Soc. Neurosci.* *26*, 11870–11880.
- Ruangkittisakul, A., Schwarzacher, S.W., Secchia, L., Ma, Y., Bobocea, N., Poon, B.Y., Funk, G.D., and Ballanyi, K. (2008). Generation of Eupnea and Sighs by a Spatiochemically Organized Inspiratory Network. *J. Neurosci.* *28*, 2447–2458.
- Ruangkittisakul, A., Kottick, A., Picardo, M.C.D., Ballanyi, K., and Negro, C.A.D. (2014). Identification of the pre-Bötzinger complex inspiratory center in calibrated “sandwich” slices from newborn mice with fluorescent Dbx1 interneurons. *Physiol. Rep.* *2*, e12111.
- Rubin, J.E., Hayes, J.A., Mendenhall, J.L., and Del Negro, C.A. (2009). Calcium-activated nonspecific cation current and synaptic depression promote network-dependent burst oscillations. *Proc. Natl. Acad. Sci. U. S. A.* *106*, 2939–2944.

- Rybak, I.A., Ptak, K., Shevtsova, N.A., and McCrimmon, D.R. (2003). Sodium Currents in Neurons From the Rostroventrolateral Medulla of the Rat. *J. Neurophysiol.* *90*, 1635–1642.
- Schneider, C.A., Rasband, W.S., and Eliceiri, K.W. (2012). NIH Image to ImageJ: 25 years of image analysis. *Nat. Methods* *9*, 671–675.
- Schwarzacher, S.W., Rüb, U., and Deller, T. (2011). Neuroanatomical characteristics of the human pre-Bötzing complex and its involvement in neurodegenerative brainstem diseases. *Brain* *134*, 24–35.
- Scorcioni, R., Polavaram, S., and Ascoli, G.A. (2008). L-Measure: a web-accessible tool for the analysis, comparison and search of digital reconstructions of neuronal morphologies. *Nat. Protoc.* *3*, 866–876.
- Scott, E.K., and Luo, L. (2001). How do dendrites take their shape? *Nat. Neurosci.* *4*, 359–365.
- Segev, I., and Rall, W. (1998). Excitable dendrites and spines: earlier theoretical insights elucidate recent direct observations. *Trends Neurosci.* *21*, 453–460.
- Shapiro, S.S., and Wilk, M.B. (1965). An analysis of variance test for normality (complete samples). *Biometrika* *52*, 591–611.
- Shepherd, G.M. (2004). *The Synaptic Organization of the Brain* (Oxford University Press, USA).
- Sherman, D., Worrell, J.W., Cui, Y., and Feldman, J.L. (2015). Optogenetic perturbation of preBötzing Complex inhibitory neurons modulates respiratory pattern. *Nat. Neurosci.* *18*, 408–414.
- Sholl, D.A. (1953). Dendritic organization in the neurons of the visual and motor cortices of the cat. *J. Anat.* *87*, 387–406.
- Smith, J.C., Greer, J.J., Liu, G.S., and Feldman, J.L. (1990). Neural mechanisms generating respiratory pattern in mammalian brain stem-spinal cord in vitro. I. Spatiotemporal patterns of motor and medullary neuron activity. *J. Neurophysiol.* *64*, 1149–1169.
- Smith, J.C., Ellenberger, H.H., Ballanyi, K., Richter, D.W., and Feldman, J.L. (1991). Pre-Bötzing complex: a brainstem region that may generate respiratory rhythm in mammals. *Science* *254*, 726–729.
- Smith, J.C., Abdala, A.P.L., Koizumi, H., Rybak, I.A., and Paton, J.F.R. (2007). Spatial and Functional Architecture of the Mammalian Brain Stem Respiratory Network: A Hierarchy of Three Oscillatory Mechanisms. *J. Neurophysiol.* *98*, 3370–3387.

Sokolowski, K., Esumi, S., Hirata, T., Kamal, Y., Tran, T., Lam, A., Oboti, L., Brighthaupt, S.-C., Zaghlula, M., Martinez, J., et al. (2015). Specification of Select Hypothalamic Circuits and Innate Behaviors by the Embryonic Patterning Gene *Dbx1*. *Neuron* 86, 403–416.

Sokolowski, K., Tran, T., Esumi, S., Kamal, Y., Oboti, L., Lischinsky, J., Goodrich, M., Lam, A., Carter, M., Nakagawa, Y., et al. (2016). Molecular and behavioral profiling of *Dbx1*-derived neurons in the arcuate, lateral and ventromedial hypothalamic nuclei. *Neural Develop.* 11, 12.

Song, H., Hayes, J.A., Vann, N.C., Drew LaMar, M., and Del Negro, C.A. (2015). Mechanisms Leading to Rhythm Cessation in the Respiratory PreBötzing Complex Due to Piecewise Cumulative Neuronal Deletions. *ENeuro* 2.

Song, H., Hayes, J.A., Vann, N.C., Wang, X., LaMar, M.D., and Negro, C.A.D. (2016). Functional Interactions between Mammalian Respiratory Rhythmogenic and Premotor Circuitry. *J. Neurosci.* 36, 7223–7233.

Stanek, E., Cheng, S., Takatoh, J., Han, B.-X., and Wang, F. (2014). Monosynaptic premotor circuit tracing reveals neural substrates for oro-motor coordination. *ELife* 3, e02511.

Stornetta, R.L., Rosin, D.L., Wang, H., Sevigny, C.P., Weston, M.C., and Guyenet, P.G. (2003). A group of glutamatergic interneurons expressing high levels of both neurokinin-1 receptors and somatostatin identifies the region of the pre-Bötzing complex. *J. Comp. Neurol.* 455, 499–512.

Strübing, C., Krapivinsky, G., Krapivinsky, L., and Clapham, D.E. (2001). TRPC1 and TRPC5 Form a Novel Cation Channel in Mammalian Brain. *Neuron* 29, 645–655.

Stuart, G.J., and Spruston, N. (2015). Dendritic integration: 60 years of progress. *Nat. Neurosci.* 18, 1713–1721.

Suzue, T. (1984). Respiratory rhythm generation in the in vitro brain stem-spinal cord preparation of the neonatal rat. *J. Physiol.* 354, 173–183.

Swietek, B., Gupta, A., Proddutur, A., and Santhakumar, V. (2016). Immunostaining of Biocytin-filled and Processed Sections for Neurochemical Markers. *J. Vis. Exp.*

Tahmasian, M., Rosenzweig, I., Eickhoff, S.B., Sepehry, A.A., Laird, A.R., Fox, P.T., Morrell, M.J., Khazaie, H., and Eickhoff, C.R. (2016). Structural and functional neural adaptations in obstructive sleep apnea: An activation likelihood estimation meta-analysis. *Neurosci. Biobehav. Rev.* 65, 142–156.

- Talpalar, A.E., Bouvier, J., Borgius, L., Fortin, G., Pierani, A., and Kiehn, O. (2013). Dual-mode operation of neuronal networks involved in left–right alternation. *Nature* 500, 85–88.
- Tan, W., Janczewski, W.A., Yang, P., Shao, X.M., Callaway, E.M., and Feldman, J.L. (2008). Silencing preBötzinger Complex somatostatin-expressing neurons induces persistent apnea in awake rat. *Nat. Neurosci.* 11, 538–540.
- Thoby-Brisson, M., and Ramirez, J.-M. (2001). Identification of Two Types of Inspiratory Pacemaker Neurons in the Isolated Respiratory Neural Network of Mice. *J. Neurophysiol.* 86, 104–112.
- Thoby-Brisson, M., Karlén, M., Wu, N., Charnay, P., Champagnat, J., and Fortin, G. (2009). Genetic identification of an embryonic parafacial oscillator coupling to the preBötzinger complex. *Nat. Neurosci.* 12, 1028–1035.
- Toporikova, N., Chevalier, M., and Thoby-Brisson, M. (2015). Sigh and Eupnea Rhythmogenesis Involve Distinct Interconnected Subpopulations: A Combined Computational and Experimental Study. *ENeuro* 2, ENEURO.0074-14.2015.
- Travers, J.B., Yoo, J.-E., Chandran, R., Herman, K., and Travers, S.P. (2005). Neurotransmitter phenotypes of intermediate zone reticular formation projections to the motor trigeminal and hypoglossal nuclei in the rat. *J. Comp. Neurol.* 488, 28–47.
- Trebak, M., Vazquez, G., Bird, G.S.J., and Putney, J.W. (2003). The TRPC3/6/7 subfamily of cation channels. *Cell Calcium* 33, 451–461.
- Tryba, A.K., Peña, F., and Ramirez, J.-M. (2006). Gasping Activity In Vitro: A Rhythm Dependent on 5-HT_{2A} Receptors. *J. Neurosci.* 26, 2623–2634.
- Tupal, S., Rieger, M.A., Ling, G.-Y., Park, T.J., Dougherty, J.D., Goodchild, A.K., and Gray, P.A. (2014). Testing the role of preBötzinger Complex somatostatin neurons in respiratory and vocal behaviors. *Eur. J. Neurosci.* 40, 3067–3077.
- Tuppy, M., Barna, B.F., Alves-Dos-Santos, L., Britto, L.R.G., Chiavegatto, S., Moreira, T.S., and Takakura, A.C. (2015). Respiratory deficits in a rat model of Parkinson's disease. *Neuroscience* 297, 194–204.
- Ullrich, N.D., Voets, T., Prenen, J., Vennekens, R., Talavera, K., Droogmans, G., and Nilius, B. (2005). Comparison of functional properties of the Ca²⁺-activated cation channels TRPM4 and TRPM5 from mice. *Cell Calcium* 37, 267–278.
- Urbani, A., and Belluzzi, O. (2000). Riluzole inhibits the persistent sodium current in mammalian CNS neurons. *Eur. J. Neurosci.* 12, 3567–3574.

Vann, N.C., Pham, F.D., Hayes, J.A., Kottick, A., and Negro, C.A.D. (2016). Transient Suppression of Dbx1 PreBötzinger Interneurons Disrupts Breathing in Adult Mice. *PLOS ONE* 11, e0162418.

Vlemincx, E., Van Diest, I., Lehrer, P.M., Aubert, A.E., and Van den Bergh, O. (2010). Respiratory variability preceding and following sighs: A resetter hypothesis. *Biol. Psychol.* 84, 82–87.

Volgin, D.V., Rukhadze, I., and Kubin, L. (2008). Hypoglossal premotor neurons of the intermediate medullary reticular region express cholinergic markers. *J. Appl. Physiol. Bethesda Md* 1985 105, 1576–1584.

Wallen-Mackenzie, A., Gezelius, H., Thoby-Brisson, M., Nygard, A., Enjin, A., Fujiyama, F., Fortin, G., and Kullander, K. (2006). Vesicular Glutamate Transporter 2 Is Required for Central Respiratory Rhythm Generation But Not for Locomotor Central Pattern Generation. *J. Neurosci.* 26, 12294–12307.

Wang, X., Hayes, J.A., Reville, A.L., Song, H., Kottick, A., Vann, N.C., LaMar, M.D., Picardo, M.C.D., Akins, V.T., Funk, G.D., et al. (2014). Laser ablation of Dbx1 neurons in the pre-Bötzing complex stops inspiratory rhythm and impairs output in neonatal mice. *ELife* 3, e03427.

Wearne, S.L., Rodriguez, A., Ehlenberger, D.B., Rocher, A.B., Henderson, S.C., and Hof, P.R. (2005). New techniques for imaging, digitization and analysis of three-dimensional neural morphology on multiple scales. *Neuroscience* 136, 661–680.

Weese-Mayer, D.E., Lieske, S.P., Boothby, C.M., Kenny, A.S., Bennett, H.L., and Ramirez, J.-M. (2008). Autonomic dysregulation in young girls with Rett Syndrome during nighttime in-home recordings. *Pediatr. Pulmonol.* 43, 1045–1060.

Welzl, H., and Bureš, J. (1977). Lick-synchronized breathing in rats. *Physiol. Behav.* 18, 751–753.

Weragalaarachchi, K. (2012). Morphological Study of Dbx1+ Respiratory Rhythm-Generating Neurons in PreBötzing Complex in Neonatal Mice. The College of William and Mary.

Westberg, K.-G., and Kolta, A. (2011). The Trigeminal Circuits Responsible for Chewing. In *International Review of Neurobiology*, N.K. Masayuki Kobayashi Koichi Iwata and John L. Waddington, ed. (Academic Press), pp. 77–98.